

Relativistic Hydrodynamics and other topics in Numerical Relativity

by

Ignacio (Iñaki) Olabarrieta

Licenciado en Ciencias, Universidad del País Vasco, 1998
M.Sc., The University of British Columbia, 2000

A THESIS SUBMITTED IN PARTIAL FULFILMENT OF
THE REQUIREMENTS FOR THE DEGREE OF

DOCTOR OF PHILOSOPHY

in

THE FACULTY OF GRADUATE STUDIES

(Department of Physics and Astronomy)

We accept this thesis as conforming
to the required standard

.....
.....
.....
.....

THE UNIVERSITY OF BRITISH COLUMBIA

August 5, 2004

© Ignacio (Iñaki) Olabarrieta, 2004

In presenting this thesis in partial fulfilment of the requirements for an advanced degree at the University of British Columbia, I agree that the Library shall make it freely available for reference and study. I further agree that permission for extensive copying of this thesis for scholarly purposes may be granted by the head of my department or by his or her representatives. It is understood that copying or publication of this thesis for financial gain shall not be allowed without my written permission.

(Signature) _____

Department of Physics and Astronomy

The University Of British Columbia
Vancouver, Canada

Date _____

Abstract

In this thesis I consider three different projects in numerical relativity. The first one is a study of the spherically-symmetric collapse of a scalar field with a potential that mimics the inclusion of angular momentum. This work has been carried out in collaboration with M. W. Choptuik, W. Unruh and J. Ventrella. In this study we found a new family of type II critical solutions which are discretely self similar.

The second project involves work I did in another collaboration with M. W. Choptuik, L. Lehner, R. Petryk, F. Pretorius and H. Villegas. Here we study the dynamical evolution of 5-dimensional generalizations of black holes, called black strings, which are known to be unstable to sufficiently long-wavelength perturbations along the string direction. Not only have we been able to dynamically trigger the instability, explicitly verifying the results from perturbation theory, we have been able to evolve for sufficiently long times to observe that the system goes through a phase (not necessarily the final end-state) that resembles a series of black holes connected by a thin black string.

The third and most extensive part of this thesis is a study of ideal fluids fully coupled to gravity, both in spherical symmetry and in axisymmetry. In this project we have cast both the dynamic and equilibrium equations for general relativistic hydrodynamics in the 2+1+1 formalism and in a way that is tailor-made for the use of high resolution shock capturing methods. In addition, our implementation, for the case of no rotation, is able to evolve discontinuous data and has proven to be convergent. Unfortunately our implementation currently has too much numerical dissipation, and suggests that the use of adaptive methods may be very helpful in achieving long term evolution of star-like configurations.

Contents

Abstract	ii
Contents	iii
List of Figures	vi
List of Tables	viii
Acknowledgements	ix
1 Introduction	1
1.1 3+1 Decomposition	3
1.2 Critical Phenomena	7
1.3 Black Holes and Black Strings	10
1.4 Relativistic Hydrodynamics	13
1.5 Summary of Results	16
2 Scalar Field Collapse with Angular Momentum	18
2.1 Introduction	18
2.2 Equations of Motion	19
2.2.1 Equations	19
2.2.2 Regularity and Boundary Conditions	22
2.3 Results	24
2.3.1 Numerics	24
2.3.2 Families of Initial Data	25
2.3.3 Analysis	26
2.3.4 Results	27
2.4 Conclusions	32

3	Instability of a Black String	38
3.1	Introduction	38
3.2	Equations	39
3.3	Numerical Implementation	41
3.3.1	Evolution	41
3.3.2	Determination of initial data: solving the constraints	43
3.3.3	Finding Event Horizons	45
3.4	Results	47
4	General Relativistic Hydrodynamics in Spherical Symmetry	52
4.1	Introduction	52
4.2	Model/Equations	53
4.3	Numerics	58
4.3.1	Geometric Equations	59
4.3.2	Hydrodynamic Equations	61
4.4	Results	69
4.4.1	New Variables	69
4.4.2	Evolution of TOV solution	72
5	Axisymmetric Hydrodynamics	78
5.1	Introduction	78
5.2	2+1+1 Formalism	78
5.2.1	Geometry	81
5.2.2	Fluids	85
5.2.3	Boundary and Regularity conditions	87
5.3	Initial Data for Rotating Stars	88
5.3.1	Integrability Condition	90
5.4	Numerics	92
5.5	Results	97
6	Conclusions and Directions for Future Research	108
6.1	Scalar Field Collapse with Angular Momentum	109
6.2	Instability of a Black String	109
6.3	Relativistic Hydrodynamics	110
	Bibliography	112

A Hydrodynamic equations in conservation form 121

B Scalar fields considered in the $l=1$ case 123

C Hydrodynamic equations in the 2+1+1 formalism 127

D Characteristic Structure 136

List of Figures

1.1	3 + 1 decomposition of spacetime.	6
1.2	Penrose diagram of a spherical symmetric black hole.	11
2.1	Values of $\log_{10}(\Delta_l)$ versus l	28
2.2	Values of $\log_{10}(\gamma_l)$ versus l	29
2.3	Value of $\max_t \{\max_r \{2M(t, r)/r\}\}$ in the critical regime as a function of l	30
2.4	Values of T_l^* versus l	31
2.5	$T_l^* \Delta_l$ as a function of l	33
2.6	Fit to periodicity of the times at which $\max_r \{2M/r(t, r)\}$ attains its maximum.	34
2.7	Fit to DSS of the times at which $\max_r \{2M(t, r)/r\}$ attains its maximum.	35
3.1	Values of R_{\max} , R_{\min} and λ for the apparent horizon as a function of time.	48
3.2	Embedding diagram of the evolution of the apparent horizon.	49
3.3	Plots of the apparent horizon and estimates of the event horizon location.	51
4.1	Outgoing boundary conditions for the fluid variables.	58
4.2	Control Volume for the spherical symmetric code.	62
4.3	Calculation of the Roe flux.	66
4.4	$\psi(\infty)$ calculated using the original variables and a shooting method to integrate the HC 70	
4.5	Solution curves for TOV initial conditions.	74
4.6	Convergence of the evolution of a TOV solution.	76
4.7	Evolution of a TOV solution with varying amounts of numerical flux.	77
5.1	Numerical grid for axisymmetric hydrodynamics.	96
5.2	Convergence test for a weak gravitating axisymmetric pulse of perfect fluid.	98
5.3	Geometry of the setup to study the KH instability.	100
5.4	KH instability.	101
5.5	Pressure evolution of a weakly self-gravitating pulse of fluid.	103
5.6	Evolution of the conformal factor for a weakly self-gravitating pulse of fluid.	104

5.7	Evolution of a strongly self-gravitating pulse of fluid.	105
-----	------------------------------------------------------------------	-----

List of Tables

2.1	Families of initial Data.	25
2.2	Type of initial data.	25
2.3	Properties of critical solutions for different values of l	37

Acknowledgements

I want to thank the Government of the Basque Country for providing me with a grant to work on this thesis. I also want to thank my collaborators in the projects discussed and all the current and past members of the numerical relativity group in UBC. Special thanks go to Scott Noble for teaching me so much about relativistic hydrodynamics. Tom Davis, Phil Eles, and Bojan Losic for listening to some of my paranoias. My family and friends in Spain who always have encouraged me to finish this thesis. And finally my supervisor, Matt Choptuik, for all his help, encouragement and patience.

Chapter 1

Introduction

Strong, dynamical gravity plays a crucial role in many interesting astrophysical systems. Especially when the strength of gravity becomes such that the typical length scale, R , of the system is comparable to the gravitational length scale, $L_G = GM/c^2$, defined by the mass, M , of the system, (G and c are, respectively, Newton's constant, and the speed of light in vacuum) or typical velocities are comparable to c , Newtonian gravity fails to completely describe the dynamics of the system. In such cases Einstein's theory of gravitation—general relativity—gives a more accurate description. Some examples of these astrophysical systems are supernovae explosions, neutron stars (including pulsars), and black holes.

In Einstein's theory of gravitation the effects of gravity are encapsulated in a Lorentzian metric tensor, $g_{\alpha\beta}$, defined on a differentiable manifold. This manifold is identified with the region of the universe (i.e. space and time) in which we are interested. This metric tensor tells us how distances and times change from point to point in the manifold and this translates directly to how one measures distances and times in the physical spacetime. The theory provides equations that the metric tensor satisfies, known as the Einstein field equations:

$$G_{\alpha\beta} = \frac{8\pi G}{c^4} T_{\alpha\beta}. \quad (1.1)$$

$G_{\alpha\beta}$ is known as the Einstein tensor and, in general, is a very complicated function of the metric $g_{\alpha\beta}$ as well as its first and second spatial and temporal derivatives. Specifically

$$G_{\alpha\beta} = R_{\alpha\beta} - \frac{1}{2} g_{\alpha\beta} R, \quad (1.2)$$

where $R_{\alpha\beta}$ is the Ricci tensor and $R = \text{Tr}[R_{\alpha\beta}]$ is the Ricci scalar (Tr denotes the trace). On the right hand side of equation (1.1) we have the stress-energy tensor, $T_{\alpha\beta}$, which describes the matter content in our spacetime.

The tensor form of the Einstein equations hide their great complexity when written out explicitly in a specific coordinate system. In general they are 10 coupled, non-linear, time-dependent partial differential equations, which for most cases, particularly those of astrophysical interest, are amenable only to numerical solution. Additionally, these equations are invariant under general diffeomorphisms. This invariance is associated with the coordinate invariance or *covariance* of the

physical theory. In general we need to fix the coordinate system in some way. This frequently involves solving some extra partial differential equations.

The purpose of this thesis is to numerically evolve these equations for three different situations, focusing on the case in which $T_{\alpha\beta}$ is the stress-energy tensor associated with a perfect fluid so that we must solve the equations of general relativistic hydrodynamics along with Einstein's equations. Spacetimes containing scalar fields as well as vacuum solutions are also considered.

In particular in Chap. 2, we discuss a new family of critical solutions that has been discovered in collaboration with M. Choptuik, W. Unruh and J. Ventrella. These results were found for a massless scalar field in spherical symmetry with a potential that tries to mimic the effects of angular momentum. I played a leading role in almost all phases of this project.

In Chap. 3, we discuss the main results of a collaboration with M. Choptuik, L. Lehner, R. Petryk, F. Pretorius and H. Villegas in which the instability of a black string, a five dimensional extension to a black hole, was studied dynamically [18]. I focus on the parts of the computations for which I was responsible; this involved solving the initial data constraints and developing some tools for analysis of the physics of the solutions.

In the last part of the thesis, Chaps. 4 and 5, we discuss our efforts to study the evolution of a perfect fluid in axisymmetric spacetimes. The equations for the fluid and the geometry in the so-called 2+1+1 formalism are presented and our numerical implementation of a computer code to solve the system is explained in detail.

The remainder of this introductory chapter is organized as follows. First, in Sec. 1.1, we discuss one way to cast equations (1.1) in a way that is appropriate for their solution as an initial-value (dynamical) problem. This formalism is the one used in Chaps. 2, 3, and 4, and it is a crucial part of the formalism used in Chap. 5. Then, in Sec. 1.2, we briefly introduce the topic of critical phenomena in gravitational collapse. A short introduction to black holes and black strings in 5 dimensions follows. In Sec. 1.4, an introduction to, and a summary of, previous work in relativistic hydrodynamics is given. We conclude with a brief summary of the results of the thesis in Sec. 1.5.

In the remainder of the thesis we choose units such that $G = c = 1$, we adopt the Einstein summation convention for tensor-component indices, and we use the signature $\{-, +, +, +\}$ for the metric tensor $g_{\alpha\beta}$. Greek/lower-case latin/upper-case latin indices are 4-dimensional (spacetime), 3-dimensional (spatial) and 2-dimensional (spatial) tensor-component indices, respectively. Indices involving letters from the beginning of each alphabet, i.e. $\alpha, \beta, \gamma, \dots, a, b, c, \dots$ and A, B, C are generally abstract tensor indices, while those involving letters near the middle of each alphabet, i.e. $\mu, \nu, \xi, \dots, i, j, k, \dots$ and I, J, K, \dots generally refer to tensor components taken with respect to some specific coordinate system.

1.1 3+1 Decomposition

In this section we discuss a way of rewriting equations (1.1) in a form tailor-made for the study of their evolution. There are many people who have worked on the problem of decomposing these equations: [3], [10], [71] and [115] describe some of the main efforts. Here we follow York's development [115], which gives a "3+1" decomposition of the field equations (1.1), and a set of first-order-in-time equations for dynamical variables describing the geometry. Our goals are to choose the values of the free fields defined at an instant of time (constant- t spacelike hypersurface), and to find the solution of the geometry and the matter for the whole subsequent spacetime (future or past development of the initial data). In this decomposition of equations (1.1), it is also possible to identify which geometric fields are to be freely chosen at the initial time—this is a non-trivial issue due to the existence of the constraints (described below).

Since we want to set initial data at a constant- t hypersurface, it is natural to foliate the spacetime with spacelike hypersurfaces of constant time. This foliation will produce a decomposition of equations (1.1) into equations constraining dynamical quantities intrinsic to each hypersurface, and equations that tell us how to propagate these dynamical variables from hypersurface to hypersurface.

One way of defining the foliation is by introducing a scalar field t with the following property: the level sets defined by this scalar field, i.e. surfaces of constant t , must be spacelike hypersurfaces, meaning that any vector field defined on the hypersurfaces is spacelike. For now, we will assume that these hypersurfaces cover all of the spacetime (or at least the region of interest) and that they are free of (physical) singularities. Associated with t is the (locally) closed one form, Ω_α , given by

$$\Omega_\alpha = \nabla_\alpha t. \quad (1.3)$$

Since the slices are spacelike, Ω_α is timelike, and we can therefore write the square of its norm as

$$g^{\alpha\beta}\Omega_\alpha\Omega_\beta = -\frac{1}{\alpha^2}, \quad (1.4)$$

where α is a positive function¹. Notice that the *distance* (actually the proper time) between hypersurfaces labelled by t and $t + dt$, as measured by observers moving orthogonally to the slices, is αdt . For this reason, α , is usually called the *lapse* function. It is useful to define the normalized one-form, ω_α

$$\omega_\alpha = \alpha\Omega_\alpha, \quad (1.5)$$

and the unit normal vector, n^α

$$n^\alpha = -g^{\alpha\beta}\omega_\beta, \quad (1.6)$$

¹Those not familiar with tensor analysis should not confuse the α function with the α index.

where the sign has been chosen so that n^α is future-directed. Using this definition the metric, $\gamma_{\alpha\beta}$, induced in the spacelike hypersurface can be written as

$$\gamma_{\alpha\beta} = g_{\alpha\beta} + n_\alpha n_\beta. \quad (1.7)$$

$\gamma_{\alpha\beta}$ is a purely spatial tensor, i.e. it has no component along n^α :

$$\gamma_{\alpha\beta} n^\beta = g_{\alpha\beta} n^\beta + n_\alpha n_\beta n^\beta = n_\alpha - n_\alpha = 0, \quad (1.8)$$

where we have used the fact that $n_\alpha n^\alpha = -1$. It is also important to note that the mixed form

$$\gamma^\alpha{}_\beta = \delta^\alpha{}_\beta + n^\alpha n_\beta, \quad (1.9)$$

is the projection operator onto the spatial hypersurfaces. Associated with the Riemannian metric (1.7) there is a 3-metric-compatible covariant derivative, D_a , satisfying

$$D_a \gamma_{bc} = 0 \quad (1.10)$$

that can also be defined via projection of the spacetime covariant derivative, ∇_α . For example for a spatial vector, V^α , we have

$$D_\delta V^\gamma = \gamma^\alpha{}_\delta \gamma^\gamma{}_\beta \nabla_\alpha V^\beta. \quad (1.11)$$

Using D_a , we can calculate the 3-dimensional curvature ${}^{(3)}R_{abcd}$, 3-dimensional Ricci tensor ${}^{(3)}R_{ab}$, and 3-dimensional Ricci scalar ${}^{(3)}R$. These quantities describe the internal geometry of each hypersurface; in addition, we need a description of how the metric γ_{ab} changes from slice to slice. This information is encoded in the (symmetric) extrinsic curvature tensor, K_{ab} , which can be defined by:

$$K_{ab} = -\frac{1}{2} \mathcal{L}_{n^\alpha} \gamma_{ab}. \quad (1.12)$$

Here \mathcal{L}_{n^α} is the Lie derivative along the unit vector field normal to the hypersurface and the factor of $-1/2$ is a matter of convention. It is worth noticing that K_{ab} is a purely spatial tensor, since \mathcal{L}_{n^α} commutes with the projection operator (1.9).

Now we have all the elements needed to proceed with the 3+1 decomposition of (1.1). Specifically, we consider the following projections of the field equations:

$$n^\alpha n^\beta G_{\alpha\beta} = 8\pi n^\alpha n^\beta T_{\alpha\beta}, \quad (1.13)$$

$$\gamma^a{}_\alpha n_\beta G^{\alpha\beta} = 8\pi \gamma^a{}_\alpha n_\beta T^{\alpha\beta}, \quad (1.14)$$

$$\gamma^\alpha{}_a \gamma^\beta{}_b G_{\alpha\beta} = 8\pi \gamma^\alpha{}_a \gamma^\beta{}_b T_{\alpha\beta}. \quad (1.15)$$

It is relatively straightforward to show that

$$n^\alpha n^\beta G_{\alpha\beta} = \frac{1}{2} \left[{}^{(3)}R + (K^a{}_a)^2 - K_{ab} K^{ab} \right], \quad (1.16)$$

and

$$\gamma^a{}_\alpha n_\beta G^{\alpha\beta} = D_b (K^{ab} - \gamma^{ab} K^c{}_c). \quad (1.17)$$

We can now write equations (1.13) and (1.14) as

$$\frac{1}{2} \left[{}^{(3)}R + (K^c{}_c)^2 - K_{ab} K^{ab} \right] = 8\pi\rho, \quad (1.18)$$

$$D_a (K^{ab} - \gamma^{ab} K^c{}_c) = 8\pi j^b, \quad (1.19)$$

where we have made use of the following definitions for the projections of the stress energy tensor:

$$\rho \equiv n^\alpha n^\beta T_{\alpha\beta}, \quad (1.20)$$

$$j^a \equiv \gamma^a{}_\alpha n_\beta T^{\alpha\beta}. \quad (1.21)$$

Physically, these quantities are the energy and momentum densities, respectively, that time-like observers moving normally to the hypersurfaces would observe.

Note that equations (1.18) and (1.19) only involve spatial tensors and spatial derivatives of such tensors. These equations need to be satisfied by the 3-metric, γ_{ab} , the extrinsic curvature, K_{ab} , and the matter densities, ρ and j^a , on every hypersurface. In particular, they need to be satisfied at the initial time and thus they constrain the initial data. This implies that not every metric function γ_{ab} and every component of K_{ab} (12 values in total) are freely specifiable, but that they need to be chosen in such a way that the constraint equations are obeyed. Equation (1.18) is called the Hamiltonian constraint, while (1.19) are usually called the momentum constraints.

To develop the other 6 field equations, equations (1.15), it is useful to use a time derivative operator, \mathcal{L}_{N^α} , where N^α is a vector field dual to the one form Ω_α , meaning that $\Omega_\alpha N^\alpha = 1$. It is important to note that this vector field is unique only up to reparametrization of the (spatial) coordinates in each hypersurface. In particular, any vector field $t^\alpha = (\partial/\partial t)^\alpha = N^\alpha + \beta^\alpha = \alpha n^\alpha + \beta^\alpha$, such that $\beta^\alpha n_\alpha = 0$, satisfies $\Omega_\alpha t^\alpha = 1$ (see Fig. 1.1). We will hereafter assume that we have adopted a so-called “3+1” coordinate system adapted to some such vector field, t^α , as illustrated in Fig. 1.1. Since β^α is a spatial vector, we have $\beta^0 = 0$ in such a coordinate system. The vector field β^α encodes the diffeomorphism invariance within the hypersurfaces and, more geometrically, describes the shifting in the spatial coordinates from hypersurface to hypersurface relative to normal propagation (see Fig. 1.1). Hence β^α is known as the shift vector. In terms of \mathcal{L}_{N^α} , the extrinsic curvature tensor can be written as:

$$K_{ab} = -\frac{1}{2\alpha} \mathcal{L}_{N^\alpha} \gamma_{ab} = -\frac{1}{2\alpha} (\mathcal{L}_{t^\alpha} \gamma_{ab} - \mathcal{L}_{\beta^\alpha} \gamma_{ab}), \quad (1.22)$$

which implies

$$K_{ab} = -\frac{1}{2\alpha} \left(\frac{\partial \gamma_{ab}}{\partial t} - D_b \beta_a - D_a \beta_b \right). \quad (1.23)$$

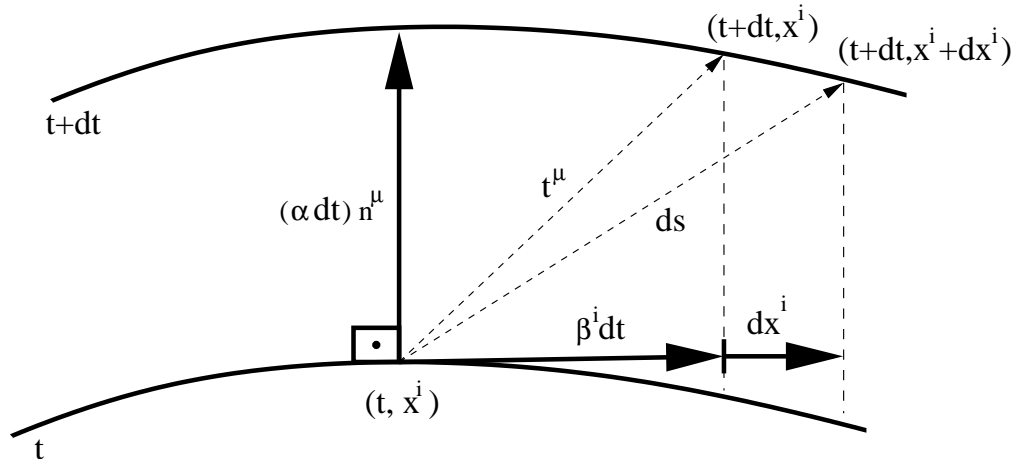


Figure 1.1: 3 + 1 decomposition of the spacetime. The distance (proper time) along the direction of the unit normal vector, n^μ , between hypersurfaces labelled by t and $t + dt$ is given by αdt . Note that β^i and dx^i are purely spatial vectors defined on the tangent space of the hypersurface at event (t, x^i) . In general, in order to move to an event with the same spatial coordinates, x^i , on hypersurface $t + dt$, i.e. in order to move along the vector field $(\partial/\partial t)^\mu$, we have to shift by an amount $\beta^i dt$ on the future spatial hypersurface relative to normal propagation. The distance between events with coordinates (t, x^i) and $(t + dt, x^i + dx^i)$ is ds and can be calculated by the “Pythagorean theorem” for Lorentzian geometry.

After some algebra, we can write equations (1.15) as

$$\mathcal{L}_{t^\mu} K_{ab} = \mathcal{L}_{\beta^a} K_{ab} - D_a D_b \alpha + \alpha \left\{ {}^{(3)}R_{ab} - 2K_{ac} K^c_b + K_{ab} K^c_c - 8\pi \left[S_{ab} - \frac{1}{2} \gamma_{ab} (S^c_c + \rho) \right] \right\}, \quad (1.24)$$

where $S_{ab} \equiv \gamma^\alpha_a \gamma^\beta_b T_{\alpha\beta}$, known as the spatial stress tensor, is the total spatial projection of the stress energy tensor onto the hypersurface. Equations (1.18), (1.19) and (1.24) complete the decomposition of equations (1.1).

Let us stress that we have: (a) kinematical variables, the lapse and the shift, that encode the coordinate freedom of the theory and that must be specified in some fashion; (b) dynamical variables, γ_{ab} , K^a_b , which, loosely speaking, encode the physical information describing the geometry of spacetime.

The 3+1 decomposition of the 4-dimensional line-element can be expressed using the 4-dimensional Lorentzian version of the Pythagorean theorem (as described in [71]). Specifically, the square of the spacetime displacement, ds^2 , between events with coordinates (t, x^i) and $(t + dt, x^i + dx^i)$ can be written as (see Fig. 1.1)

$$\begin{aligned} ds^2 &= -(\alpha dt)^2 + \gamma_{ij} (dx^i + \beta^i dt)(dx^j + \beta^j dt) \\ &= -(\alpha^2 + \beta_i \beta^i) dt^2 + 2\gamma_{ij} \beta^i dt dx^j + \gamma_{ij} dx^i dx^j. \end{aligned} \quad (1.25)$$

An important note is that since only a maximum of 6 of the 10 (second-order) Einstein equations are independent of each other, we have considerable freedom in choosing which specific equations to solve during a dynamical evolution. The initial data for the geometry and matter must *always* be chosen to satisfy the constraint equations (1.18–1.19), but the evolution equations (1.24), together with the contracted Bianchi identities, $G_{\alpha\beta}{}^{;\alpha} = 0$, then guarantee that the constraints are satisfied at any future or past time. This property of the continuum system of equations is in general lost once the system is discretized; at best the numerical solution only satisfies the unused equations at the truncation order of the approximation. Checking the convergence properties of the residuals of these unused equations thus gives us a very strong check of the validity of our solutions.

1.2 Critical Phenomena

The discovery of critical phenomena in gravitational collapse was reported by Choptuik in [17]. He studied the spherically-symmetric collapse to black holes² of a massless scalar field, ϕ , minimally

²Black holes are described in more detail in section 1.3, at this point they can be viewed as regions of spacetime in which even light is trapped and cannot escape to infinity.

coupled to gravity. The Lagrangian for this problem is given by

$$L = \frac{R}{16\pi} - \frac{1}{2}\phi_{;\alpha}\phi^{;\alpha}, \quad (1.26)$$

where R is the Ricci scalar (the usual Lagrangian for gravity). At that time, it was already known that, under the same symmetry assumptions, the dynamical evolution of weak configurations of scalar field leads to dispersal of the scalar field to infinity, resulting in Minkowski-like spacetimes [24], and that configurations of sufficiently strongly self-gravitating scalar field give rise to black hole formation [25]. Choptuik's work was the first systematic study of the intermediate regime. In order to study the transition to black hole formation, the initial data were parametrized by a single parameter, p , such that for high parameter values black holes were formed, while for low values, dispersal was the end state. An example of such a parameter is the initial amplitude of the scalar field. At the threshold of black hole formation, $p = p^*$, interesting and unexpected results were found.

First of all, as we approach p^* from above, the mass of the black hole that is obtained tends to zero following a power law:

$$M_{\text{BH}} = C(p - p^*)^\gamma, \quad (1.27)$$

where M_{BH} is the mass of the black hole, C is a constant of proportionality and $\gamma \approx 0.37$ is a universal exponent independent of the specific family of initial data used in the calculation. We note that scaling of dimensionful quantities is also seen if the critical solution is approached from below (subcritical) rather than from above.

Moreover, for values of p close to p^* , the solutions in the strong field regime approach—at least for some finite time and in some finite region of space—a solution called the critical solution, which is universal in the following sense. There exist coordinates (τ, ρ) in which the critical solutions obtained using different families of initial data all take the same form. In [17] so-called polar-areal coordinates, leading to a line-element

$$ds^2 = -\alpha(t, r)^2 dt^2 + a(t, r)^2 dr^2 + r^2 d\Omega^2, \quad (1.28)$$

were used to perform the evolutions, with t measuring central proper time. The relationship between these coordinates and (τ, ρ) is given by:

$$\tau \equiv \ln(t^* - t) + \kappa, \quad (1.29)$$

$$\rho \equiv \ln r + \kappa, \quad (1.30)$$

with t^* and κ depending on the family of initial data used to construct the solution. Not only was the critical solution found to be universal, it also showed an echoing behaviour. This means that in

the critical regime, any dimensionless function, Z , constructed from the solution has the following symmetry:

$$Z(\tau - \Delta, \rho - \Delta) = Z(\tau, \rho), \quad (1.31)$$

where, for the scalar field, the *period* $\Delta \approx 3.4$ is obviously also a universal parameter since all the features of the solution are universal when written in (τ, ρ) coordinates. The transformation given by (1.31) amounts to a discrete rescaling of the original coordinates (t, r) , and solutions with this rescaling invariance are thus said to be discretely self similar (DSS).

The critical solution is unstable, essentially by construction: small deviations from the precise value $p = p^*$ lead to complete dispersal of the field, or to the formation of a black hole. Soon after the publication of [17], similar behaviour was observed in the collapse of axisymmetric gravitational waves [1] and, crucially, in spherically symmetric collapse of perfect fluid with a so-called radiation equation of state [29]. In this last work Evans conjectured that perturbation theory about the *continuously* self-similar solution that appeared at the black hole threshold for fluid collapse might provide insight into some of the phenomenology that had been observed.

Work along precisely these lines was carried out with great success by Koike *et al* [53] who made the key observation that the “sharpness” of the empirically measured mass scaling law (1.27) for fluid collapse (as well as for the original scalar collapse), strongly suggested that the critical solution, had only a *single* unstable mode. From this assumption, and using a mathematical development precisely analogous to that used in the standard treatment of statistical mechanical critical phenomena, it follows that the mass-scaling exponent is simply the reciprocal of the Lyapunov exponent associated with the unstable mode. In follow up work, Gundlach [40] was able to show that this picture also held for the more difficult to treat case of the massless scalar field.

Similar behaviour has been found in the collapse to black hole formation for many other types of matter. In general, different matter models behave in two qualitatively different ways at the threshold of black hole formation. In contrast to the massless scalar case, it has been found that the smallest black hole formed for some matter models is non-zero. In analogy with statistical mechanical critical phenomena (first and second order phase transitions) this sort of transition is dubbed “type I”, whereas a transition characterized by (1.27) is called “type II”.

Type I critical solutions exhibit a fundamental length scale; it is this scale that determines the minimum value for the mass of the black hole above threshold. On the other hand, type II critical solutions are generically scale invariant. More specifically, type I critical solutions are usually static or periodic, while type II are self similar, or discretely self similar.

Although many matter models have been investigated in spherical symmetry (see [43] for a recent review) very little is known about critical phenomena in less symmetric systems. So far,

only two systems have been investigated: axisymmetric vacuum, studying the collapse to black hole formation of gravitational waves [1]; and the collapse of a scalar field in axisymmetry [20], [21]. The calculations described in Chap. 2 represent an attempt to investigate the possible effects of angular momentum on critical collapse via an effective potential for a scalar field in spherical symmetry.

1.3 Black Holes and Black Strings

The Einstein field equations (1.1) allow for black hole solutions. For example in spherical symmetry the well-known Schwarzschild metric

$$ds^2 = g_{\mu\nu} dx^\mu dx^\nu = - \left(1 - \frac{2M}{r}\right) dt^2 + \left(1 - \frac{2M}{r}\right)^{-1} dr^2 + r^2 d\Omega^2, \quad (1.32)$$

is the *unique* vacuum solution (apart from flat spacetime, which is *not* a regular limit of Schwarzschild as $M \rightarrow 0$) of the field equations. The region of the spacetime with $r < 2M$ cannot communicate with infinity, i.e. no physical trajectory (timelike or null curve) originating from $r < 2M$ can propagate to $r \rightarrow \infty$ (nor to $r > 2M$ for that matter), and the region $r < 2M$ is thus known as a black hole.

In order to describe black holes, it helps to draw diagrams of the corresponding spacetimes that preserve causal structure and which compactify the spacetimes, so that various types of infinity lie at finite coordinate distance. These sorts of pictures are called Penrose diagrams. Figure 1.2 shows one such diagram for the Schwarzschild solution (1.32). Note that each point in the bulk of the diagram represents a 2-sphere manifold of specific radius and that light rays (null geodesics) travel along straight lines inclined at 45° . This diagram has many features worthy of discussion. Starting with the boundary, at the right-most edge of the plot there is a point called i^0 which represents spacelike infinity and which is the locus where all outgoing spacelike geodesics end. In addition, the point on top, labelled by i^+ , corresponds to future timelike infinity and is where future-directed timelike geodesics in region I terminate (i^- corresponds to past timelike infinity and is where past-directed timelike geodesics end). The line joining i^+ with i^0 is future null infinity, denoted by \mathcal{I}^+ , and is the place where null, future-directed, geodesics originating in region I terminate (likewise, past null infinity, \mathcal{I}^- , is the line connecting i^0 with i^-). If a timelike geodesic is within bulk region II it does not end at i^+ but instead ends at the dotted line labelled $r = 0$ (the same happens for null geodesics within region II, they also cannot reach \mathcal{I}^+). The dotted line corresponds to $r = 0$ in (1.32) and is, in fact, a physical (crushing) singularity of the spacetime, where the spacetime curvature goes to infinity. The observation that, starting in region II, no timelike or null geodesic can propagate into region I suggests that region II is a black hole. Its boundary is called an event horizon.

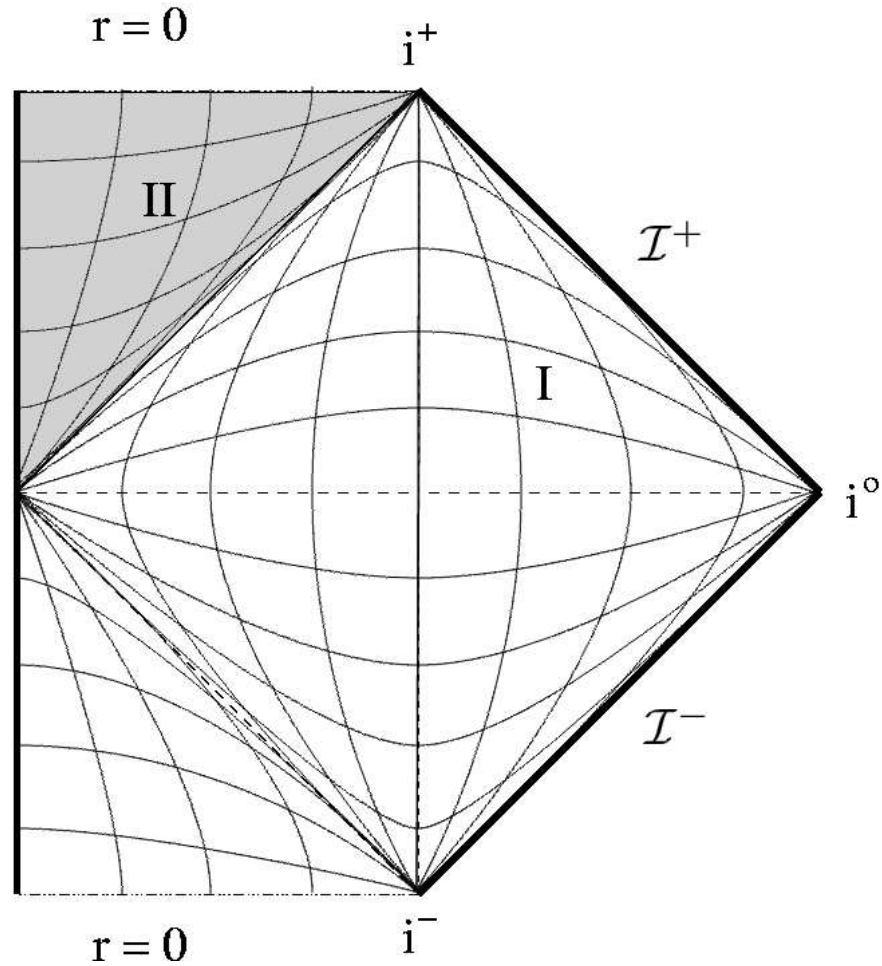


Figure 1.2: Penrose diagram of a spherically symmetric black hole. Note that light rays travel at 45 degree angles in this diagram. Region II (shaded) is causally disconnected from \mathcal{I}^+ and thus lies within a black hole. The boundary of the black hole is called the event horizon. Plotted lines running approximately vertically (horizontally) correspond, in region I, to lines with constant coordinate r (t). We also note that the diagram shown is only half of the full Penrose diagram for the maximally extended Schwarzschild solution, see [71].

There are a whole family of spacetimes (Kerr-Newman solutions) with similar characteristics to Schwarzschild, and that can be characterized by just a few parameters (specifically three —mass, angular momentum and charge). These spacetimes are believed to be the end-states of the evolution of sufficiently massive stars. At the end of the evolution of a massive star (larger than about $10 M_{\odot}$) its structure resembles an onion, with layers of different materials with increasing atomic number towards its centre. The inner most core is composed of iron which is maximally bound with respect to the nuclear force, and hence cannot undergo thermonuclear burning. This core grows from the burning of the outer layers of silicon and sulphur, and when its mass becomes of the order of $1.5 M_{\odot}$, its pressure cannot counteract the gravitational pull and it collapses. This process releases titanic amounts of energy that are carried out to the outer regions of the star mainly by neutrinos. A highly energetic shock is produced that moves outwards through the envelope. This shock energizes the outer region which undergoes a violent explosion—a supernova—which expels all of the outer layers of the original star. The remnant of this process is a very compact object of a few kilometres radius and, at most, several solar masses. In particular, if the mass of the remnant exceeds about $3M_{\odot}$ ³, even degeneracy pressure cannot hold the star up against gravitational collapse [89] and a black hole, whose mass will again be a few M_{\odot} , will form. Although there is not yet unequivocal observational evidence for this type of black hole, many candidates have been found in binary systems—for an inventory see [82].

There is also evidence for more massive black holes. Studies of microlensing events and “ultra-luminous” X-ray sources, among others, have provided some hints about the possible existence of black holes with intermediate masses [105], i.e. those with masses between a few solar masses and a few million. Moreover, there are strong indications that super massive black holes, with masses in the range $10^6 - 10^9 M_{\odot}$ or greater, can be found in most galactic centres. See [26] and [35] for discussion of the evidence for such a black hole at the centre of the Milky Way galaxy.

It is a very well known result that black holes in 4 dimensions (3 spacelike, 1 timelike) are *stable* solutions in general relativity [14]. This means that small perturbations around the solutions tend to die off, and to be radiated away in the form of gravitational radiation. Although this is a very well established result in 4 dimensions, very little is known about the behaviour of solutions with event horizons in a 5-dimensional spacetime (we consider here 4 spatial and 1 temporal dimension). Gregory and Laflamme [37], [38] showed, using linear stability analysis, that at least some classes of black hole solutions in 5 dimensions—those known as black strings, and which have the structure “4-D black hole” \times “a line”—are unstable under long wavelength perturbations in the “line” (string) dimension.

Given that small perturbations of these solutions tend to grow, a natural question arises: what is

³For some models with differential rotation the upper limit can exceed $4M_{\odot}$ [5].

the end state of the evolution of the perturbed black string? There are some arguments supporting the idea that the state will involve some kind of bifurcation of the original solution [37], [38]. Were this true, it would represent a violation of Penrose's cosmic censorship conjecture, generalized to 5 dimensions, which posits that singularities of the type discussed above should generically be hidden from external view by event horizons. On the other hand an argument has been published by Horowitz and Maeda [48] suggesting that bifurcation cannot occur in finite time.

In order to study the end stage of the perturbed black string, numerical calculations have been performed [18]. In Chap. 3 we summarize the main results found in that collaborative effort, focusing on the numerical solution of the 5-dimensional analogue of the constraint equations (1.18-1.19).

1.4 Relativistic Hydrodynamics

Following [110], we can define a perfect fluid such that in local comoving coordinates the fluid is isotropic. In particular, assuming that the spacetime is Minkowskian (flat), we can write

$$T^{tt} = \rho_H, \quad T^{xx} = T^{yy} = T^{zz} = P, \quad (1.33)$$

where ρ_H is the proper energy density and P is the hydrostatic pressure. The first generalization of these stress tensor components will be for the case where each fluid element has an arbitrary spatial velocity, v^i , with respect to some fixed (lab) frame. This can be achieved via a general boost (spacetime rotation), resulting in

$$T^{\mu\nu} = (\rho_H + P) u^\mu u^\nu + P \eta^{\mu\nu}. \quad (1.34)$$

Here u^μ is the fluid 4-velocity, satisfying $u^\mu u_\mu = -1$, and $\eta^{\mu\nu} = \text{diag}[-1, 1, 1, 1]$. Note that the equations for the conservation of energy and momentum can be written as $T^{\mu\nu}{}_{;\mu} = 0$, and that this divergence involves an ordinary derivative since we are in flat spacetime. In order to extend this expression to a generally curved manifold we need only replace the Minkowskian metric by the general Lorentzian metric of the spacetime and partial derivatives with covariant derivatives. Thus, in a general curved spacetime, the stress energy tensor for a perfect fluid is

$$T^{\mu\nu} = (\rho_H + P) u^\mu u^\nu + P g^{\mu\nu} \quad (1.35)$$

with (local) conservation of energy and momentum expressed by

$$(T^{\mu\nu})_{;\mu} = 0. \quad (1.36)$$

Note that this expression is in accordance with the Einstein equations (1.1) since $(G^{\mu\nu})_{;\mu} = 0$ by the Bianchi identities. In addition to this conservation law, a fluid can satisfy additional conservation

laws depending on its composition. In the current case we will assume conservation of particle number (baryon number), which is expressed as

$$(J^\mu)_{;\mu} = 0, \quad (1.37)$$

where J^μ is the current associated with the particles; i.e.

$$J^\mu = \rho_0 u^\mu, \quad (1.38)$$

with ρ_0 the rest mass density. As usual, in addition to these equations, we need to specify an equation of state for the fluid that relates the pressure to the energy densities.

We also note that the above form for the perfect fluid stress-energy excludes the possibility of thermal or viscous effects—in other words we neglect all the non-adiabatic effects in the fluid (apart from shocks). The proper general relativistic incorporation of such terms is still a matter of open research [72].

In the strong gravity regime, the pressure and stresses are typically so large that we cannot assume the fluid is incompressible. In addition, for highly relativistic configurations, the pressure contributions to the stress tensor can be of the same order as those from the energy density. This makes general relativistic fluids behave very differently from the type of fluids that we encounter in everyday life, where stress energy tensors are dominated by the rest mass density of the fluid, where the assumption of incompressibility is often a very good one, and where characteristic three velocities satisfy $v \ll 1$. General relativistic hydrodynamics (hereafter simply relativistic hydrodynamics, or relativistic hydro) involves the solution of equations (1.36)–(1.37) coupled to equations (1.1). There has been quite a lot of work in relativistic hydrodynamics because it is a *good* model for a lot of astrophysical systems, and is reasonably tractable computationally. A good review of the work and the methods that have been and are being used to study relativistic hydro can be found in [30]. Here we only briefly touch on some of the main efforts.

May & White:

The field started with the pioneering work of May and White [68], [69] who studied the collapse of a perfect fluid in spherical symmetry. In order to study the collapse they adopted Lagrangian coordinates (i.e. coordinates comoving with the fluid). This approach was very successful but, due to its Lagrangian nature, it is difficult to generalize to less symmetric spacetimes (for example, axisymmetric solutions) because the matter may follow complicated paths which can “tangle” the coordinates. May and White used a numerical approach based on finite difference approximations, which involves replacement of the derivatives in the equations with finite difference quotients. In order to deal with the shocks that generically arise during the collapse of perfect fluids, the

continuum equations were modified to include terms that mimic viscosity [108]. The addition of this artificial viscosity tends to smooth out discontinuities over many finite-difference grid zones. This method of solution has also been used by other authors in order to investigate supernovae explosions [98], and neutron star collapse [70], all in spherical symmetry.

Wilson formulation:

Wilson developed one of the first Eulerian formulations for relativistic hydrodynamics that saw use in numerical work [111]. His approach involved writing the fluid equations (1.36–1.37) as a set of advection equations, i.e. equations of the type:

$$\frac{\partial Q_i}{\partial t} + \frac{\partial Q_i v^j}{\partial x^j} = S_i, \quad (1.39)$$

where v^j is again the fluid 3-velocity with respect to the lab (Eulerian) frame. The formulation included the definition of appropriate variables, $\{Q_i(t, x^j)\}$, that allowed the fluid equations to be cast in this specific form. Note that in general S_i has terms involving the pressure gradients which are treated as sources. The original implementation of this formalism [111] was used to study the accretion of perfect fluid on to a rotating black hole. This was a “background calculation” in which the fluid’s self-gravity was assumed to be negligible, so that the curved geometry acted on the fluid, but not vice versa. Wilson’s numerical implementation was again based on finite differences, using so-called upwind derivatives for stability as well as artificial viscosity in regions with shocks. This formulation has been used extensively. Some of the systems that have been simulated using it include stellar core collapse [112], axisymmetric stellar core collapse [85], [28], [95], and coalescence of binary neutron stars using the conformally-flat approximation for the geometry [113].

Nakamura formulation:

For the research described in Chap. 4 and especially Chap. 5, it is of crucial importance to review the work due to Nakamura and collaborators [63], [74], [75], [76], [92]. Nakamura and his co-workers used the so-called 2+1+1 formalism for the geometry and the fluid equations. This formalism is a variant of the 3+1 decomposition described in Sec. 1.1 and is designed for use with spacetimes having an axial Killing vector field (i.e. axisymmetric spacetimes). The formalism was originally developed for the Einstein equations by Geroch [34] and was extended for hydrodynamics by Maeda et al. [63]. In this approach the field equations (and the spacetime) are first decomposed with respect to the axial Killing vector field. The decomposition is very similar in spirit to a Kaluza-Klein reduction, in which effective matter fields and equations of motion are produced in the quotient 3-dimensional spacetime. After this initial decomposition is complete, the resultant 3-dimensional spacetime is decomposed using an analogue of the 3+1 approach (now, however, it is a 2+1 decomposition, which accounts for the name “2+1+1”).

Nakamura's numerical implementation of the 2+1+1 equations also used finite difference methods—largely paralleling Wilson's approach—and artificial viscosity to treat shocks. The main application studied was the collapse of axisymmetric stars, including stars with large values of angular momentum. Their investigation showed that the collapsing star tends to form a ring structure which, in the case of moderate values of angular momentum, is enclosed by an apparent horizon. On the other hand, for initial stars that were sufficiently rapidly rotating, some evidence for the formation of naked singularities was found [74].

Valencia Formulation:

An important property of the fluid equations that none of the above studies took full advantage of is the fact that the hydrodynamical equations can be written in conservation law form (see App. A):

$$\frac{\partial Q_i}{\partial t} + \frac{\partial F_i^j}{\partial x^j} = S_i. \quad (1.40)$$

Here, F_i^j is the flux associated with Q_i along the x^j direction and, crucially, S_i does not contain any derivatives of the dynamical fluid variables. This was first exploited in the context of relativistic hydrodynamics by the *Valencia group* in [66]. Casting the equations in the above form allows the use of the Godunov approach (see [57], [58] for a summary of this and other so-called conservative methods) which ensures the correct jumps in values of dynamical variables across discontinuities, as well as the correct shock propagation speeds. (for these reasons such techniques are sometimes called High Resolution Shock Capturing, or HRSC, methods). One advantage with respect to formulations such as Wilson's, is that HRSC methods do not require the use of artificial viscosity for code stability, or to simulate extremely relativistic ($v \rightarrow c$) flows. Some examples of calculations are [91], [78], [31] and more recently [4]. In this thesis we will apply conservative methods to the hydrodynamic equations, and finite difference methods to the geometric equations, both within the 2+1+1 formalism.

1.5 Summary of Results

In Chap. 2, we describe a new family of critical solutions resulting from the collapse of a massless scalar field with a particular potential that mimics angular momentum in spherical symmetry. These solutions are parametrized by an angular momentum coefficient, l . We have found that for each value of l we obtain a different discretely self similar critical solution. We also find that Δ_l decreases approximately exponentially with increasing values of l and, in fact, approaches zero in such a way that the critical solution appears to be periodic in the limit $l \rightarrow \infty$. Moreover we have

found scaling laws similar to (1.27) with l -dependent mass-scaling exponents, γ_l , that also decrease with l .

In the collaborative work explained in Chap. 3 we have been able to check, by dynamical evolution of black strings, the results found using perturbative methods by Gregory and Laflamme [37]. Not only have we directly verified that long thin black strings are unstable to perturbations along the string dimension, we have seen some indications that the spacetime evolves to a state (not necessarily the end-state) which can be described as a series of black holes connected by thin black strings. Unfortunately the code crashes at late times due to a coordinate pathology. We are thus unable to make any statements concerning the ultimate end-state of the evolution, since, at the time of the crash, the spacetime is still highly dynamical.

Chap. 4 describes a spherically symmetric code for relativistic hydro whose purpose is to test the formalisms and algorithms, both at the continuum and discrete levels, subsequently used in the axisymmetric case. We have seen that, in our coordinate system (which is the natural restriction to spherical symmetry of the one used in the axisymmetric code), the standard conservation variables used in the Valencia formalism [91] must be modified in order to get a well-posed set of geometric constraint equations. In addition, we have found that the Roe approximation used in the computation of numerical fluxes results in a scheme that is too dissipative, at least for grids with constant resolution, to maintain long term evolution of stationary solutions in our chosen coordinate system.

In the concluding chapter, we present the equations for relativistic hydrodynamics written in the 2+1+1 formalism and in a way which is amenable for treatment using HRSC methods. The equations for rotational, hydrostatic equilibrium, along with an integrability condition, are also expressed in the same formalism. Finally, we describe our numerical implementation for the case of no rotation. At the current time this code is both too dissipative and too unstable to be able to use it for the study of the long term evolution of stationary solutions. However, we can evolve certain configurations of discontinuous data, and can also demonstrate that the code exhibits second order convergence for situations where the hydrodynamical flow remains smooth.

Chapter 2

Scalar Field Collapse with Angular Momentum

2.1 Introduction

In this chapter we explain the main results of a new study of critical phenomena in gravitational collapse. The work that we present here is the result of a collaboration with M. Choptuik, W. Unruh and J. Ventrella. As described in Sec. 1.2, most studies of black hole critical phenomena (or related phenomena in other sets of nonlinear evolution equations) to date have been performed assuming spherical symmetry as a simplifying assumption (exceptions are [1], [62] and more recently [20], [21]). This simplification has been adopted in most cases because accurate simulation of Type II critical solutions—which exhibit structure at all scales due to their self-similar nature—requires great computational resources. Since spherically symmetric spacetimes do not allow for angular momentum, very little is currently known about the role of angular momentum in critical collapse. For a few cases, most notably the Type II solutions found in spherically symmetric collapse of a massless scalar field [33], or certain types of perfect fluid [41], [42], perturbative calculations about the spherical critical solutions suggest that all non-spherical modes, including those contributing to net angular momentum, are damped as one approaches criticality. In particular in [33], [41] and [42] using second order perturbation theory it was found that the angular momentum of the black holes produced has the following dependence as a function of the critical parameter p :

$$\vec{L}_{\text{BH}} = \vec{L}_0 [\ln(p - p^*)] (p - p^*)^\mu, \quad (2.1)$$

where $\vec{L}_0 [\ln(p - p^*)]$ is some quasi-periodic function that is family-dependent and $\mu \approx 0.76$ is a universal scaling exponent which is larger than the corresponding γ (scaling exponent for the black hole mass in (1.27)). These calculations thus suggest that, at least for small deviations from spherical symmetry, the resulting solutions at the verge of black hole formation should remain spherically symmetric in non-symmetric collapse. We also note that an axisymmetric numerical relativity code is currently being developed [21] to study non-perturbatively some effects of angular

momentum in the critical collapse of a scalar field.

Here a different approach is taken. Maintaining spherical symmetry, the equations of motion for a massless scalar field are modified by effective terms which mock up some of the effects of angular momentum. As described below, the procedure amounts to performing an angular average over the matter field variables—similar to what is done in [88], [81] and [107]—and results in an entire family of models, parameterized by a principal angular “quantum number”, l (we will generally restrict l to take on non-negative integer values, although real-valued l 's are also formally possible). We note that since the models remain spherically symmetric, we cannot use them to address the validity of the perturbative calculations mentioned above (e.g. equation (2.1)). Nonetheless, we find interesting results that may shed some light on the effects of angular momentum near the black hole threshold.

Some of the main results that have been found are as follows. First, each value of the angular momentum parameter l , apparently defines a distinct critical solution. For $l < 10$, these solutions are found to be discretely self similar, with values of the echoing exponent Δ_l (see (1.31) and the accompanying discussion) that rapidly decrease (approximately exponentially) as l increases. As a result, for large values of l , and for the time scales for which we are able to dynamically evolve near criticality, the threshold solutions become approximately *periodic*. In addition, and as expected for Type II solutions, we find that for $l < 7$ the masses of the black holes formed follow power laws of the type (1.27). As with the echoing exponents, for increasing values of l it is found that the mass-scaling exponent, γ_l , rapidly decreases, again approximately exponentially in l .

The remainder of this chapter is structured as follows. In the following section we describe the recipe used to calculate the effective equations of motion, along with the regularity and boundary conditions imposed in the solution of these equations. In Sec. 2.3 we briefly describe the numerical code, the way the solutions have been analyzed, and then provide a summary of the results obtained for varying values of l .

2.2 Equations of Motion

2.2.1 Equations

In order to derive equations of motion, scalar fields of the following form are considered:

$$\Psi_l^m(t, r, \theta, \phi) = \psi(t, r)\Theta_l^m(\theta, \phi), \quad m = -l, -l + 1, \dots, l - 1, l \quad (2.2)$$

where $\Theta_l^m(\theta, \phi)$ are normalized *real* eigenfunctions of the angular part of the flatspace Laplacian with eigenvalue $l(l + 1)$, and the index m labels the $2l + 1$ distinct orthonormal eigenfunctions for a

given value of l^1 . By construction, the scalar fields Ψ_l^m , are not, in general, spherically symmetric and we therefore do not study their collapse directly. Instead, our strategy is find effective equations for the *single* (t, r) -dependent quantity $\psi(t, r)$. To do so, for a specific value of l , we consider the stress-energy tensors, $T^{(lm)}_{ab}$, for the $2l + 1$ fields Ψ_l^m :

$$T^{(lm)}_{ab} = \frac{1}{8\pi} \left[\nabla_a \Psi_l^m \nabla_b \Psi_l^m - \frac{1}{2} g_{ab} (\nabla^c \Psi_l^m \nabla_c \Psi_l^m) \right], \quad (2.3)$$

where g_{ab} is the metric of the spacetime, ∇_a is the metric-compatible covariant derivative and the non-standard factor of $1/(8\pi)$ has been introduced to cancel the one in (1.1). Again by construction, the sum of these stress tensors

$$\mathcal{T}^{(l)}_{ab} = \sum_m T^{(lm)}_{ab}, \quad (2.4)$$

is spherically symmetric and thus depends only on $\psi(t, r)$, l , and the metric g_{ab} . The net result of this procedure is equivalent to performing an angle average over the individual stress energy tensors $T^{(l)}_{ab}$ and then summing them, i.e. to computing

$$\mathcal{T}^{(l)}_{ab} = \sum_m \langle T^{(lm)}_{ab} \rangle \quad (2.5)$$

where

$$\langle f(\theta, \phi) \rangle = \frac{1}{4\pi} \int f(\theta, \phi) \sin(\theta) d\theta d\phi. \quad (2.6)$$

We can now compute the effective equation of motion for the field, $\psi(t, r)$, by demanding that the divergence of the total stress energy tensor is zero:

$$g^{ac} \nabla_c \mathcal{T}^{(l)}_{ab} = 0. \quad (2.7)$$

The equations for the geometric variables are determined from the $3 + 1$ decomposition of the Einstein field equations explained in Sec. 1.1. For the current study we adopt Schwarzschild-like (polar-areal) coordinates, in which the metric (1.25) takes the form:

$$ds^2 = -\alpha^2(t, r) dt^2 + a^2(t, r) dr^2 + r^2 d\theta^2 + r^2 \sin^2 \theta d\phi^2. \quad (2.8)$$

Here $\alpha(t, r)$ is the lapse function and $a(t, r)$ is the only non-trivial component of the 3-metric γ_{ij} (both α and a are positive functions). Using this metric, the non zero components of the

¹Note that, in general, $\Theta_l^m(\theta, \phi)$ will *not* be eigenfunctions of the azimuthal rotation operator $(\partial/\partial\phi)$, since they are real.

stress-energy tensor for a general value of l are

$$\mathcal{T}^{(l)t}_t = -\frac{(2l+1)}{8\pi} \left[\frac{1}{a^2} (\Pi^2 + \Phi^2) + l(l+1) \frac{\psi^2}{r^2} \right], \quad (2.9)$$

$$\mathcal{T}^{(l)t}_r = -\frac{(2l+1)}{8\pi} \frac{2}{a\alpha} \Pi \Phi, \quad (2.10)$$

$$\mathcal{T}^{(l)r}_r = \frac{(2l+1)}{8\pi} \left[\frac{1}{a^2} (\Pi^2 + \Phi^2) - l(l+1) \frac{\psi^2}{r^2} \right], \quad (2.11)$$

$$\mathcal{T}^{(l)\theta}_\theta = \mathcal{T}^{(l)\phi}_\phi = \frac{(2l+1)}{8\pi a^2} (\Pi^2 - \Phi^2), \quad (2.12)$$

and the stress-energy trace is

$$\mathcal{T}^{(l)} \equiv \mathcal{T}^{(l)i}_i = \frac{(2l+1)}{8\pi} \left[\frac{2}{a^2} (\Pi^2 - \Phi^2) - 2l(l+1) \frac{\psi^2}{r^2} \right]. \quad (2.13)$$

In the above expressions, we have made use of the auxiliary variables, Φ and Π , defined as follows:

$$\Phi(t, r) = \frac{\partial \psi}{\partial r}, \quad (2.14)$$

$$\Pi(t, r) = \frac{a}{\alpha} \frac{\partial \psi}{\partial t}. \quad (2.15)$$

The dynamical equations of motion for these fields, which follow from the definition of Φ as well as the wave equation for ψ (which in turn can be derived from the vanishing of the divergence of the total stress tensor (2.7)) are then:

$$\frac{\partial \Phi}{\partial t} = \frac{\partial}{\partial r} \left(\frac{\alpha}{a} \Pi \right), \quad (2.16)$$

$$\frac{\partial \Pi}{\partial t} = \frac{1}{r^2} \frac{\partial}{\partial r} \left(r^2 \frac{\alpha}{a} \Phi \right) - l(l+1) a \alpha \frac{\psi}{r^2}. \quad (2.17)$$

Note that the dependence of these equations on l is only through the last term in equation (2.17) which is proportional to $l(l+1)/r^2$. This term can be thought of as the field-theoretic extension of an analogous term due to the angular momentum potential, l^2/r^2 , in the 1-dimensional reduced problem of a particle moving in a central potential.

As mentioned above, equations for the geometric variables result from the 3 + 1 decomposition of the field equations presented in Sec. 1.1, as well as from our choice of coordinates. Specifically, we have the following:

$$\frac{1}{a} \frac{\partial a}{\partial r} = \frac{(2l+1)}{2} r \left(\Pi^2 + \Phi^2 + l(l+1) \frac{a^2}{r^2} \psi^2 \right) - \frac{a^2 - 1}{2r}, \quad (2.18)$$

$$\frac{1}{\alpha} \frac{\partial \alpha}{\partial r} = \frac{(2l+1)}{2} r \left(\Pi^2 + \Phi^2 - l(l+1) \frac{a^2}{r^2} \psi^2 \right) + \frac{a^2 - 1}{2r}, \quad (2.19)$$

$$\frac{\partial a}{\partial t} = (2l+1) r \alpha \Pi \Phi. \quad (2.20)$$

Equation (2.18) is the Hamiltonian constraint (1.18), which is used to determine the 3-metric component, a . Similarly, the slicing condition (2.19) fixes the lapse function α at each instant of time, and is often known as the *polar slicing condition*. It can be derived from the demand that $\text{Tr}(K_{ab}) = K^r_r + K^\theta_\theta + K^\phi_\phi = K^r_r$ for all times. The Hamiltonian constraint and slicing condition, with appropriate regularity and boundary conditions, completely fix the geometric variables in this coordinate system. Equation (2.20) is an extra equation derived from the definition of K^r_r and the momentum constraint (1.19). In our numerical solutions, it is used as a gauge of the accuracy of our simulations, as well as to provide a replacement for the Hamiltonian constraint in certain strong field instances where the numerical constraint solver fails. In addition, we compute the mass aspect function, $M(t, r)$,

$$M(t, r) = \frac{r}{2} \left(1 - \frac{1}{a^2} \right), \quad (2.21)$$

which serves as a valuable diagnostic quantity in our simulations. The value of this function as $r \rightarrow \infty$ agrees with the ADM mass (Arnowitt-Deser-Misner mass [3]), and more generally, in a vacuum region of spacetime, measures the amount of (gravitating) mass contained within the 2-sphere of radius r at time t . Moreover, $2M(t, r)/r$ is useful since its value approaches 1 when a trapped surface is produced and hence (modulo cosmic censorship), a black hole would form in the spacetime being constructed. We note that, as is the case with the usual Schwarzschild coordinates for a spherically symmetric black hole, polar-areal coordinates cannot penetrate apparent horizons, and in fact become singular as they come “close to” black-hole regions of spacetime, where $2M(t, r)/r \rightarrow 1$. This fact does not present a problem in the study of critical behaviour in our models, since the critical solutions *per se* have $\max_r [2M(t, r)/r]$ bounded away from 1.

2.2.2 Regularity and Boundary Conditions

In addition to the above equations of motion, appropriate regularity and boundary conditions are needed. At the origin, $r = 0$, regularity and elementary flatness implies the following expansions:

$$\lim_{r \rightarrow 0} a(t, r) = 1 + r^2 a_2(t) + O(r^4), \quad (2.22)$$

$$\lim_{r \rightarrow 0} \alpha(t, r) = \alpha_0(t) + r^2 \alpha_2(t) + O(r^4), \quad (2.23)$$

$$\lim_{r \rightarrow 0} \psi(t, r) = r^l \psi_l(t) + r^{l+2} \psi_{l+2}(t) + O(r^{l+4}). \quad (2.24)$$

This leads to the following boundary conditions:

$$a(t, 0) = 1, \quad (2.25)$$

$$\frac{\partial a}{\partial r}(t, 0) = 0, \quad (2.26)$$

$$\frac{\partial \alpha}{\partial r}(t, 0) = 0, \quad (2.27)$$

$$\psi(t, 0) = O(r^l), \quad (2.28)$$

$$\Pi(t, 0) = O(r^l), \quad (2.29)$$

$$\Phi(t, 0) = \begin{cases} O(r^{l-1}) & \text{for } l \geq 1, \\ O(r) & \text{for } l = 0. \end{cases} \quad (2.30)$$

In the continuum, our equations of motion are to be solved as a pure Cauchy problem, on the domain $t \geq 0$, $r \geq 0$, with boundary conditions at spatial infinity given by asymptotic flatness (i.e. that the matter fields vanish, and that the metric becomes that of Minkowski spacetime, as $r \rightarrow \infty$). Computationally, we solve an approximation to this problem on a finite spatial domain $0 \leq r \leq r_{\max}$, where r_{\max} is some arbitrary outer radius chosen sufficiently large that we are confident that the numerical results do not depend significantly on its precise value. At the outer boundary, then, the following condition for α is imposed:

$$\alpha(t, r_{\max}) a(t, r_{\max}) = 1. \quad (2.31)$$

This can be viewed as simply providing a convenient normalization for α , since given a solution, α , of the slicing equation (2.19), $k\alpha$ is also a solution, where k is an arbitrary positive constant. We note that although we have used (2.31) in order to perform the calculations, a different normalization convention—i.e. a different, and time dependent, choice of k —has been used in order to perform the analysis of the solutions. Specifically, in the analysis we have used central proper time $T(t)$ defined by:

$$T(t) = \int_0^t \alpha(\tilde{t}, 0) d\tilde{t}. \quad (2.32)$$

This definition of time has a natural geometrical interpretation since $r = 0$ is invariantly defined by the symmetry of the spacetime. For the scalar field variables, Π and Φ , approximate outgoing-radiation boundary conditions (Sommerfeld conditions) are used:

$$\frac{\partial \Phi}{\partial t}(t, r_{\max}) + \frac{\partial \Phi}{\partial r}(t, r_{\max}) + \frac{\Phi(t, r_{\max})}{r_{\max}} = 0, \quad (2.33)$$

$$\frac{\partial \Pi}{\partial t}(t, r_{\max}) + \frac{\partial \Pi}{\partial r}(t, r_{\max}) + \frac{\Pi(t, r_{\max})}{r_{\max}} = 0. \quad (2.34)$$

An important point in the derivation of the equations of motion is the fact that the eigenfunctions in (2.2) are discrete and the allowable values of l are only non-negative integers. Once the equations

are obtained we have relaxed that constraint and have allowed l to take non-negative *real* values (the physical interpretation of such solutions, if any, is open for discussion). The solutions corresponding to non-integer values of l would have some degree of irregularity at the origin depending on the particular value of l chosen. This implies that only some finite number of derivatives with respect to r will be defined at $r = 0$. In our particular numerical implementation, which assumes that second derivatives of the variables are defined, we have been able to study the evolution of these systems as long as $l > 3$.

2.3 Results

2.3.1 Numerics

We solve equations (2.16), (2.17) for the scalar field gradients, equations (2.18), (2.19) for the geometry, and use (2.14) to reconstruct the field ψ . The system is approximated using second order centred finite difference techniques, and coded using RNPL [65]. Numerical dissipation of the Kreiss-Oliger [52] variety was included to damp high frequency modes, and it should be noted that this particular type of dissipation is added at sub-truncation error order, so does not effect the overall accuracy of the scheme as the mesh spacing tends to 0. For the current computations, the damping terms were most useful in regularizing the truncation error estimation procedure that occurs when adaptive mesh refinement (AMR) techniques are used. It was also crucial to impose the correct leading-order regularity conditions close to the origin, $r = 0$ (equations (2.29)–(2.30)) to keep the solution regular during the evolutions.

Most of the simulations were done on a fixed uniform spatial grid $r_j = (j-1)\Delta r$, $j = 1, 2, \dots, J$, $J = 1 + r_{\max}/\Delta r$ with a typical number of grid points $J = 1025$, and typical $r_{\max} = 100$. In this grid we define discrete values $\{\psi_j\}$, $\{\Phi_j\}$, $\{\Pi_j\}$ and discrete values of the geometric fields. The regularity conditions are imposed on the dynamical variables by:

$$\Pi_1 = \begin{cases} 4/3\Pi_2 - 1/3\Pi_3 & \text{for } l = 0, \\ 0 & \text{for } l \geq 1, \end{cases} \quad (2.35)$$

$$\Pi_2 = \Pi_3/2^{2(l-1)} \quad \text{for } l \geq 2, \quad (2.36)$$

$$\Phi_1 = \begin{cases} 4/3\Phi_2 - 1/3\Phi_3 & \text{for } l = 1, \\ 0 & \text{for } l \neq 1, \end{cases} \quad (2.37)$$

$$\Phi_2 = \begin{cases} \Phi_3/2 & \text{for } l = 2, \\ \Phi_3/2^{2(l-2)} & \text{for } l > 2. \end{cases} \quad (2.38)$$

These have been calculated using the regularity conditions (2.29–2.30) and the finite difference

approximation for the first derivative with respect to r^q (q taking values 1, $l-1$ and $l-2$) at $r=0$:

$$\frac{df}{dr^q} \approx \frac{(2^{-q} - 2^q) f_1 + 2^q f_2 - 2^{-q} f_3}{(2^q - 1) \Delta r^q}. \quad (2.39)$$

For small values of the angular momentum parameter—specifically for $l \leq 2$ —an AMR algorithm based on that described in [17] was used.

2.3.2 Families of Initial Data

Our study involved the evolution of 6 different one parameter families of initial data, each defined by an initial profile $\psi(0, r)$ as listed in Table 2.1, with specific values of the parameters appearing in the profile definitions as given in Table 2.2. In addition to $\psi(0, r)$ we need to provide $\Pi(0, r)$

Family	Form of initial data, $\psi(0, r)$	p
(a)	$A \exp(-(r - r_0)^2/\sigma^2)$	A
(b)	$-2A(r - r_0)/\sigma^2 \exp(-(r - r_0)^2/\sigma^2)$	A
(c)	$A r^2 (\text{atan}(r - r_0) - \text{atan}(r - r_0 - \sigma))$	A

Table 2.1: Families of initial data and the parameter p that is tuned to generate a critical solution.

to complete the specification of the initial data. In all cases we chose $\Pi(0, r)$ to produce an approximately in-going pulse at the initial time:

$$\Pi(0, r) = \Phi(0, r) = \frac{\partial \psi}{\partial r}(0, r). \quad (2.40)$$

Initial Data	Family	Parameters
1	(a)	$r_0 = 70.0, \sigma = 5.00$
2	(b)	$r_0 = 70.0, \sigma = 5.00$
3	(c)	$r_0 = 70.0, \sigma = 5.00$
4	(a)	$r_0 = 40.0, \sigma = 10.0$
5	(a)	$r_0 = 40.0, \sigma = 5.00$
6	(a)	$r_0 = 70.0, \sigma = 10.0$

Table 2.2: Initial data used in our investigations. The family label is explained in Table 2.1.

As previously mentioned, all of the initial data families listed in Table 2.1 have a single free parameter, p , and, as is the usual case in studies of black hole critical phenomena, for any given family we observe two different final states in the evolution, depending on the value of p . For values

of $p > p^*$ the maximum value of $2M(t, r)/r$ approaches 1 implying that an apparent horizon is about to form. On the other hand if $p < p^*$ the scalar field completely disperses, and leaves (essentially) flat spacetime in its wake. The solution that arises as $p \rightarrow p^*$ then represents the threshold of black hole formation and, by definition, is the critical solution. We note that these critical solutions are *not* $t \rightarrow \infty$ end-states of evolution; rather they persist for only a finite amount of time, and, in fact, are unstable, heuristically representing an infinitely fine-tuned balance between dispersal and gravitational collapse.

2.3.3 Analysis

We have calculated p^* for the different families of initial data described above, and for different values of l , via bisection (binary search), tuning p in each case to a typical precision of $(p - p^*)/p \approx 10^{-15}$ (which is close to machine precision using 8-byte real floating point arithmetic).

As in the case for $l = 0$ (where the equations of motion reduce to those for a single, non-interacting massless scalar field, as studied in [17]), the critical solutions for values of $l \leq 9.5$ are apparently discretely self similar (DSS). As discussed in the introductory chapter, DSS spacetimes are scale-periodic, meaning that any non-dimensional quantity, Z , obeys the following equation for some specific values of the parameters Δ and T^* :

$$Z((T - T^*), r) = Z(e^{n\Delta}(T - T^*), e^{n\Delta}r), \quad (2.41)$$

where T is central proper time as defined by (2.32), and T^* is the “accumulation time” of the self-similar solution. Note that this is the same scaling invariance as (1.31) but written in the original coordinates given by (2.8). In (2.41) the integer n denotes the *echo* number. We also note that due to the discrete $\psi \rightarrow -\psi$ invariance that is exhibited both by the equations of motion as well as the critical solutions themselves, if Δ is the echoing exponent for which formula (2.41) is satisfied with $Z(T, r) \equiv \psi(T, r)$, then the geometric quantities $a(T, r)$, $\alpha(T, r)$, $2M(T, r)/r$ obey (2.41) with an echoing exponent $\Delta/2$.

In order to extract Δ from our simulations, we use the observation that certain geometric quantities will achieve (locally) extremal values on the spatial domain at discrete central proper times T_n given by

$$T_n - T^* = (T_0 - T^*) e^{n\Delta/2}. \quad (2.42)$$

where T_0 is the time at which one starts counting the echoes. Specifically, Δ and T^* have been computed by a least squares fit for the times T_n at which $\max_r [2M(t, r)/r]$ achieves a local maximum in time, i.e. by minimizing:

$$\chi^2 = \sum_{n=1}^N \left[T_n - T_0 e^{n\Delta/2} + T^* (e^{n\Delta/2} - 1) \right]^2. \quad (2.43)$$

2.3.4 Results

Table 2.3 summarizes the values of Δ_l we have estimated using this procedure; the data are also graphed in Fig. 2.1. Again, note that the reported values for Δ_l have been calculated using central proper time T instead of proper time at infinity (the parameterization used in the numerical evolutions *per se*). Also the reported uncertainties have been estimated from the deviations in the Δ_l values computed across the the six different families of initial data. The first entry in Table 2.3 ($l = 0$) corresponds to the original case studied in [17]. The second one ($l = 1$) is apparently the same solution found for the self-gravitating collapse of an $SO(3)$ non-linear σ model, assuming a hedgehog ansatz [50], [61]. The remainder of the solutions (for the other values of l) are, to the best of our knowledge, new.

As was also discussed in the introduction, systems exhibiting type II critical behaviour, where the critical solution is self-similar, generally also exhibit power-law scaling of dimensionful quantities in near-critical evolutions. For example, we can expect the black hole mass, M_{BH} , to scale as

$$M_{\text{BH}} = C (p - p^*)^{\gamma_l} \quad (2.44)$$

for super-critical evolutions as $p \rightarrow p^*$. Here C is a constant that depends on the family of initial data while γ_l is a universal exponent for each value of l , i.e. independent of the specific initial data family used to generate the critical solution. We have observed such scaling in at least some of our computations, but, following Garfinkle and Duncan [32] have found it more convenient to extract γ_l by monitoring the maximum value of the trace of the stress tensor, \mathcal{T} , which, from the Einstein equations, is proportional to the maximum value of the Ricci curvature. On dimensional grounds \mathcal{T} (defined by (2.13)) and R should both scale with an exponent -2γ . This technique has the advantage of being more precise than a strategy based directly on (2.44) since we can calculate the trace of the stress-energy more accurately than the mass of the black hole formed, and can perform the computation using sub-critical evolutions, where the gradients of field variables generally do not become as large as those in the super-critical cases. The values of γ_l as a function of l are listed in Table 2.3 and are plotted in Fig. 2.2.

As is characteristic of type-II critical solutions exhibiting discrete self-similarity, $2M(t, r)/r$ oscillates at higher frequencies and on smaller spatial scales during the course of an evolution in the critical regime. As has already been noted, as l increases, the echoing exponent Δ_l decreases rapidly. In addition, we observe that the maximum and minimum values between which the spatial maximum of $2M(t, r)/r$ oscillates increase with l (see Fig. 2.3) indicating that the critical solutions are becoming increasingly relativistic as the angular momentum barrier becomes more pronounced. The amplitude of the oscillations between these extremal values decreases since $\min_r [2M(t, r)/r]$ increases more rapidly than $\max_r [2M(t, r)/r]$ (see Fig. 2.3).

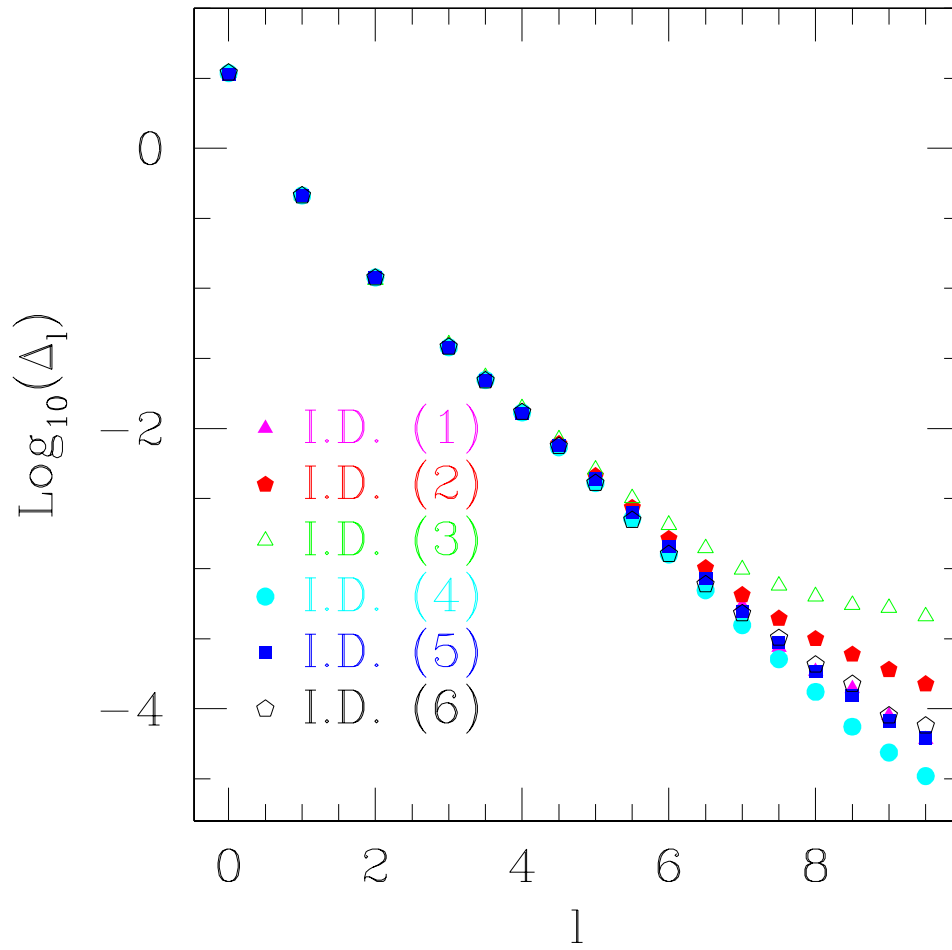


Figure 2.1: Values of $\log_{10}(\Delta_l)$ versus l . In this figure we can see that Δ_l decreases almost exponentially with l . The different lines represent different families of initial data. Assuming universality, the differences between the values calculated for the different families provides one measure of error in our determination of Δ_l .

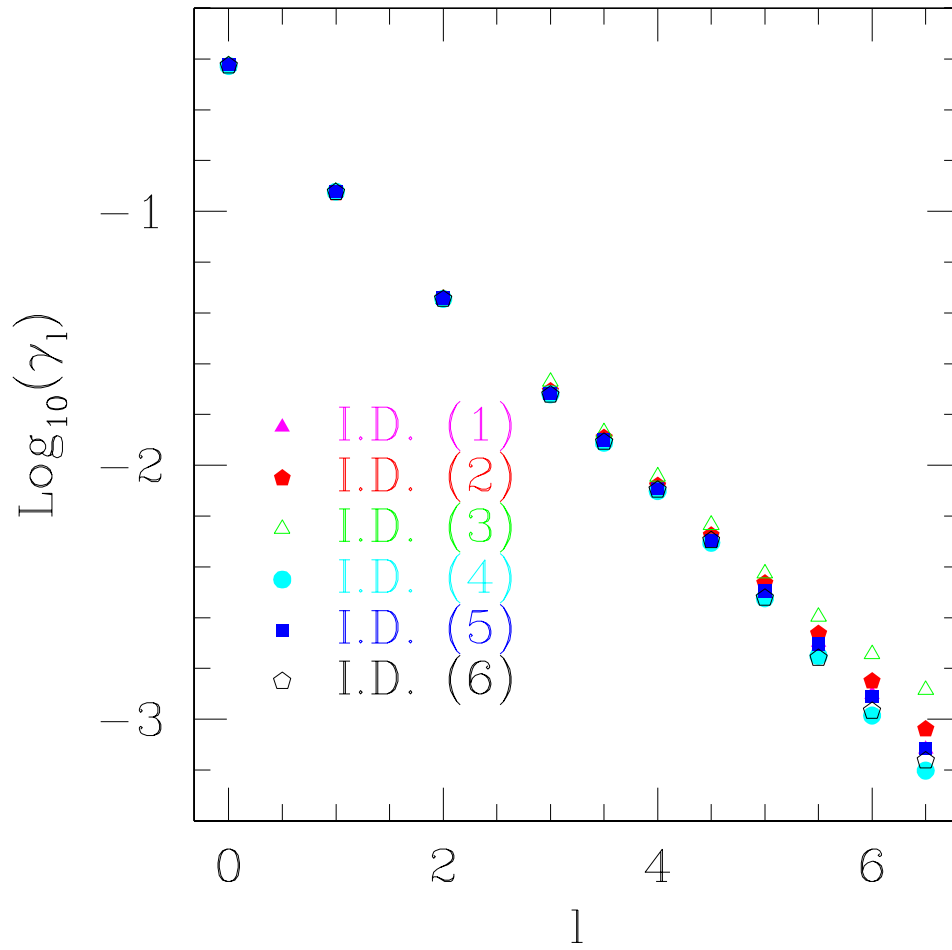


Figure 2.2: Values of $\log_{10}(\gamma_l)$ versus l , where γ_l is the scaling exponent defined by (2.44). As for the case of the echoing exponent, Δ_l , γ_l also decreases approximately exponentially with l . We note that due to lack of numerical accuracy we only can reliably compute γ_l for $l \leq 6.5$

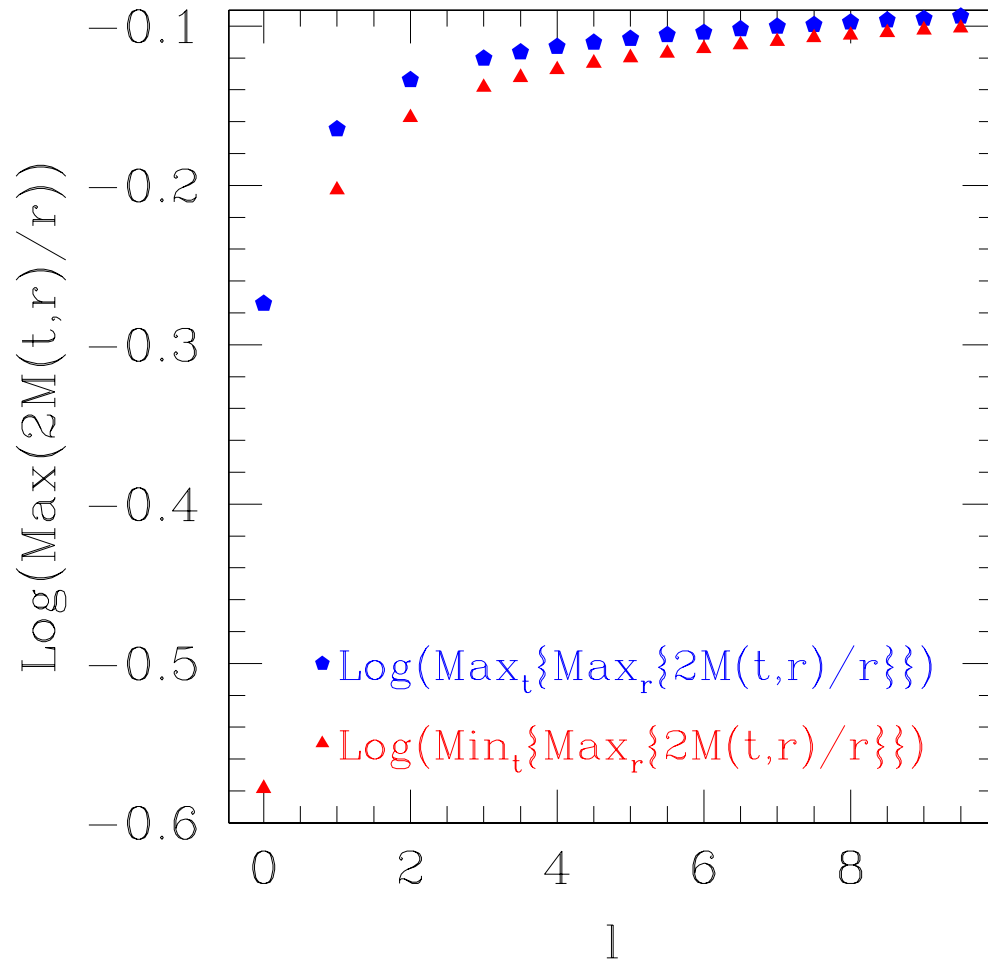


Figure 2.3: $\max_t \{\max_r [2M(t,r)/r]\}$ in the critical regime as a function of l (solid line) and the same for $\min_t \{\max_r [2M(t,r)/r]\}$ (dashed line). We see how the maximum and minimum increase with l . On the other hand the amplitude of oscillation, given by their difference, apparently tends to zero with increasing l .

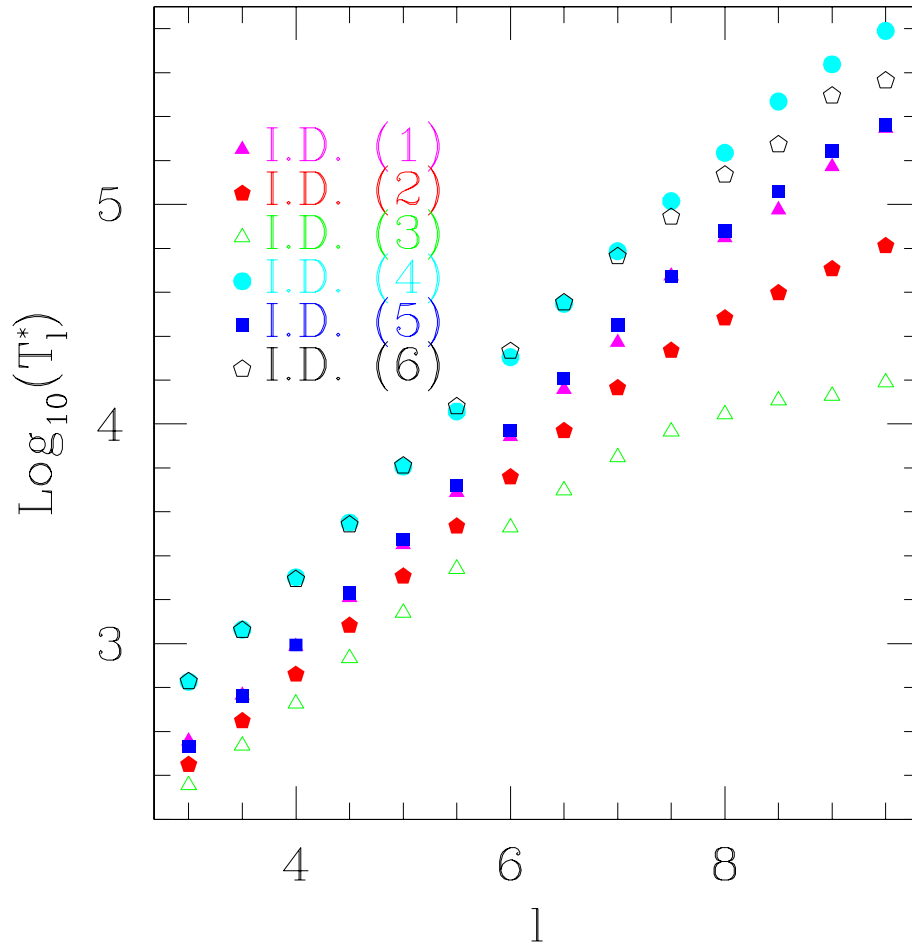


Figure 2.4: Values of $\log_{10}(T_l^*)$ versus l . T_l^* is the “accumulation time” defined by equation (2.41) for a parameter l measured using central proper time. The accumulation time increases almost exponentially showing an increase in the stability of the critical solution as l increases.

Empirically, we have also found that, as we increase l within a family of initial data, although $\Delta_l \rightarrow 0$ and $T_l^* \rightarrow \infty$ (see Fig. 2.4), the product $T_l^* \Delta_l$ appears to asymptote to a finite value. Note that ostensibly this product is family dependent (see Fig. 2.5), but that all DSS type-II critical solutions are universal only up to a global scale transformation $(r, t) \rightarrow (kr, kt)$, with k an arbitrary positive constant.

Choosing $k = k(l)$ for each of the families so that $\max_r [2M(t, r)/r]$ is attained at some fiducial radius r_0 , and considering the case $l = 10$, we find that the normalized asymptotic oscillation frequency, f_0 , defined by

$$f_0 = r_0 / (T^* \Delta) = 4.35 \pm 0.01 \quad (2.45)$$

agrees for all families to better than 1%. Again, the quoted uncertainty is estimated from the variation of f_0 across the different families of initial data. We note that for $l = 10$ the near-critical solution stays at a near-constant radial position; our spatial resolution is not enough to resolve the small changes associated with the extremely small value of Δ_l . The radial location of $\max_r [2M(t, r)/r]$ in this regime is the value of r_0 that we have used in (2.45).

We also note that the observation that f_0 is apparently well-defined and unique (up to the usual rescalings associated with type-II critical solutions), is consistent with the empirical observation that as l increases, the critical solution becomes ever closer to a *periodic* solution. In particular, for a periodic solution we have $\Delta \rightarrow 0$, and then

$$T_n - T^* = (T_0 - T^*) e^{n\Delta} \approx (T_0 - T^*) (1 + n\Delta) \approx - (T^* \Delta) n - T^*, \quad (2.46)$$

where T_0 represents the loosely defined time demarking the onset of the critical regime (and whose precise value is clearly irrelevant in the limit $T^* \rightarrow \infty$) which implies that the maximal value is attained at times T_n :

$$T_n = - (T^* \Delta) n. \quad (2.47)$$

As shown in Figs. 2.6 and 2.7, from our simulations for $l = 10$, we cannot ascertain whether the solution is discretely self similar with Δ_l very small (< 0.0002), or periodic with period $\tau = T^* \Delta$.

Naively at least, we expect that for $l > 10$, distinguishing between discrete self similarity and periodicity would become even more difficult. However, it is worth noticing that for $l = 20$ we have *not* yet seen evidence for (almost)-periodicity, with period $T^* \Delta$, but have instead seen a more complicated structure near criticality that is not yet understood.

2.4 Conclusions

In this chapter we have discussed the results for a model that tries to incorporate some of the effects of angular momentum in the context of critical gravitational collapse. A new family of spherically-

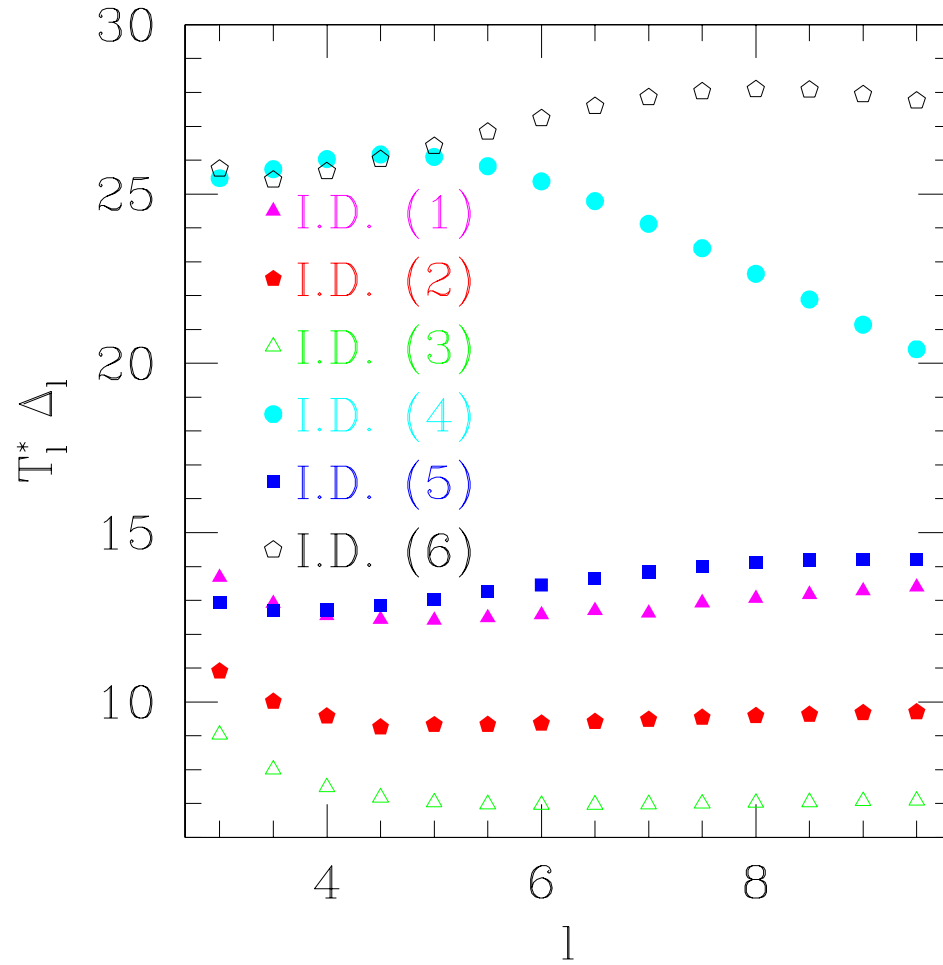


Figure 2.5: $T_l^* \Delta_l$ as a function of l . The fact that these products remain finite as $T_l^* \rightarrow \infty$ and $\Delta_l \rightarrow 0$ is evidence that the critical solutions tend to a *periodic* solution in the limit $l \rightarrow \infty$.

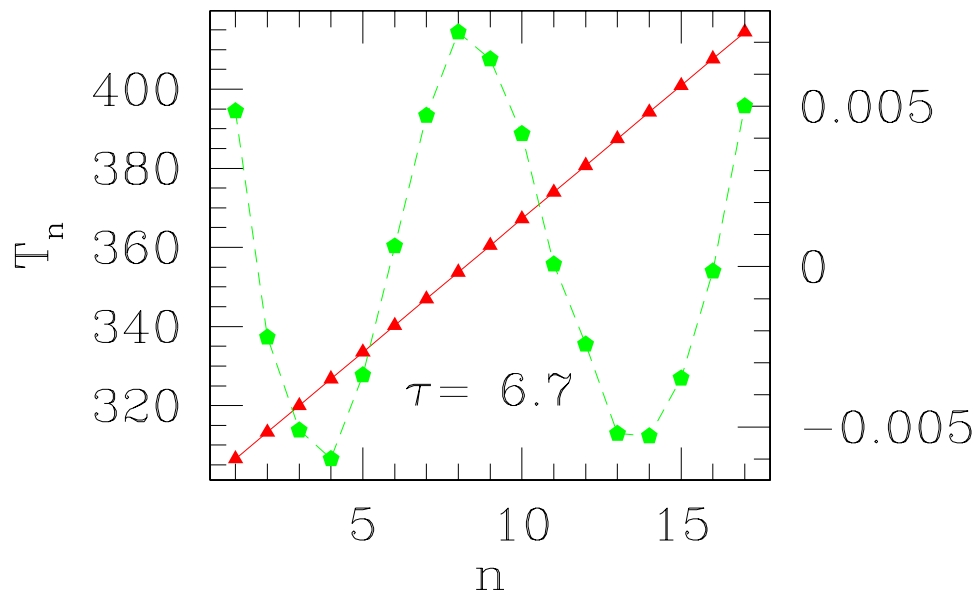


Figure 2.6: Fit of the times T_n at which $\max_r [2M(t, r)/r]$ reaches its maximum in time (denoted by triangles and scale on the left) assuming a periodic ansatz. Initial data family (1) was used with angular momentum parameter $l = 10$. We also plot the residuals of each data point with respect to the best fit (denoted by pentagons and a scale on the right)

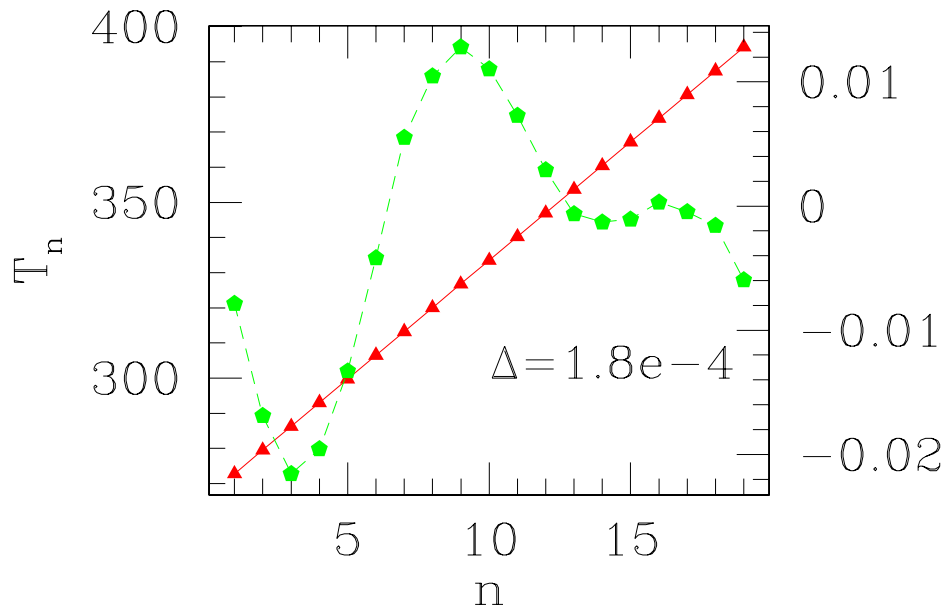


Figure 2.7: Fit of the times T_n at which $\max_r [2M(t, r)/r]$ reaches its maximum in time (triangles and scale on the left) assuming a self-similar ansatz. Initial data family (1) was used with angular momentum parameter $l = 10$. Again, we also plot the residuals of each data point with respect to the best fit (pentagons and scale on the right). Notice that the errors in the fit are of the same order as the errors to a fit assuming periodicity (Fig. 2.6), indicating that from our numerical results we are unable to distinguish between the two types of solutions for $l \geq 10$.

symmetric critical solutions, (black hole threshold solutions) labelled by an angular momentum parameter, l , have been found. These solutions have similar properties to those for the $l = 0$ case originally studied in [17]: specifically, the solutions exhibit discrete self similarity, and have scaling laws for the values of dimensionful quantities in evolutions close to criticality. We have calculated the l -dependence of the echoing exponents Δ_l , and the mass-scaling exponents γ_l , finding that both decrease rapidly with increasing l , (at least up to $l \approx 10$). Moreover, we have argued that as l increases, the critical solution approaches a periodic solution.

As we explained in the introduction, we expect that $\gamma_l = 1/\lambda_l$ where λ_l is the Lyapunov exponent associated with the single unstable mode of the critical solution for angular momentum parameter l . Therefore since $\gamma_l \rightarrow 0$ with increasing l , we apparently have $\lambda_l \rightarrow \infty$. This has the interpretation of increased stability of the critical solution for increasing l , i.e. the period of time that a solution can remain close to criticality (for a fixed amount of fine tuning) increases with l , this can be observed by the increase in T_l^* (see Fig. 2.4). We believe that this can be interpreted as an effect of the angular momentum barrier which (partially) stabilizes the collapse against black hole formation.

l	Δ_l	γ_l
0	3.43 ± 0.05	0.376 ± 0.003
1	0.460 ± 0.002	0.119 ± 0.001
2	0.119 ± 0.003	0.0453 ± 0.0002
3	0.039 ± 0.001	0.020 ± 0.001
3.5	0.0224 ± 0.0009	0.0127 ± 0.0008
4	0.0132 ± 0.0008	0.0082 ± 0.0008
4.5	0.0077 ± 0.0007	0.0052 ± 0.0006
5	0.0044 ± 0.0007	0.0033 ± 0.0005
5.5	0.0026 ± 0.0006	0.0020 ± 0.0005
6	0.0015 ± 0.0005	0.0013 ± 0.0005
6.5	0.0009 ± 0.0005	0.0008 ± 0.0005
7	0.0006 ± 0.0004	-
7.5	0.0004 ± 0.0004	-
8	0.0003 ± 0.0004	-
8.5	0.0002 ± 0.0003	-
9	0.0002 ± 0.0002	-
9.5	0.0002 ± 0.0003	-

Table 2.3: Summary of the properties of the critical solutions computed for different values of l .

Note that both the echoing exponents, Δ_l , and the mass scaling exponents, γ_l , rapidly decrease as l increases. Quoted errors have been estimated from the variation in values computed across the different families of initial data. Values of Δ_l have been calculated using central proper time T normalization of the lapse function, which is the natural normalization for type-II critical behaviour. For $l > 6.5$ we have not been able to calculate γ_l due to lack of numerical precision. Note that the $l = 0$ data agree with the original values calculated in [17], and that the $l = 1$ data agree with values calculated in [61] and [50] using models of completely different origin.

Chapter 3

Instability of a Black String

3.1 Introduction

This chapter describes a 5-dimensional problem (4 space plus 1 time dimensions) which involves the dynamical evolution of a perturbed black string. This work was a joint effort with M. Choptuik, L. Lehner, R. Petryk, F. Pretorius and H. Villegas [18]. As mentioned in the introduction, the unperturbed solution (originally proposed by Myers and Perry [73]) has the structure “4-D black hole” \times “a line”, hence the nomenclature “black string”. Gregory and Laflamme [37] proved that black strings are unstable against long wavelength perturbations in the string dimension. Our work tries to answer the natural question that arises: What is the end state of the evolution of such an instability?

In [37] it was conjectured, using entropy considerations, that unstable black strings fragment producing spatially periodic black hole solutions of the type described in [7]. This process will produce a naked singularity and hence violate (4+1 dimensional) cosmic censorship [47]. However this analysis, which is based on the linearization of the equations around the black string solution, stops being valid once the perturbation grows sufficiently. More recently, Horowitz and Maeda have argued that this proposed bifurcation of the event horizon cannot be achieved in finite time [48]. Moreover they conjectured that the system is likely to evolve to a new stationary solution which is not invariant under translations along the string direction. Following this reasoning, Wiseman solved the equations for equilibrium [114] and found new non-translationally symmetric solutions. The ADM masses, (see [3] for definition of ADM mass) of these solutions are larger than the maximum mass for an unstable black string at the same compactification length, which would appear to rule them out as candidate end-states. In [18] we adopt a different approach, in order to investigate the end state, we dynamically trigger the instability and analyze the subsequent evolution of the spacetime.

The organization of this chapter is as follows. In Sec. 3.2 we describe the form of the black string solution, define the coordinates that we use for the evolution, and define the form of the perturbation. In Sec. 3.3, we then explain the specifics of the numerical integration of the equations

of motion for the model, paying special attention to the solution of the constraint equations, and the construction of an approximate event horizon finder, which represent my chief contributions to the collaborative effort. Finally, in Sec. 3.4, we summarize the results that were obtained from the study.

3.2 Equations

The solution studied by Gregory and Laflamme [37] was first constructed by Myers and Perry [73] and describes a 5-dimensional vacuum configuration with an event horizon. With a specific choice of coordinates—called ingoing Eddington-Finkelstein coordinates—the 5-dimensional line element for the solution takes the form

$$ds^2 = -(1 - 2M/r) dt^2 + 4M/r dr dt + (1 + 2M/r) dr^2 + dz^2 + r^2 d\Omega^2, \quad (3.1)$$

where M is the *mass* of the black string, z is the so-called string dimension, and $d\Omega^2 = d\theta^2 + \sin^2\theta d\phi^2$ is the metric of a unit 2-sphere.

Note that the solution is z -invariant, so that the metric coefficients do not depend on the string dimension and that, paralleling the 4-dimensional Schwarzschild case, we can identify $r = 2M$ with the radius of the black string. In what follows we assume that the string dimension is periodic, or in more mathematical terms, that it has S^1 topology, i.e. that $z = 0$ and $z = L$ are identified, for some constant L . Physically, this choice of topology is not crucial (so long as L is chosen sufficiently large to admit the Gregory-Laflamme instability) but computationally, the choice allows us to sidestep any issues associated with imposing approximate boundary conditions in the string direction. We also note that the solution is spherically symmetric in the sense that $(\partial/\partial\theta)^\alpha$ and $(\partial/\partial\phi)^\alpha$ are Killing vector fields. Gregory and Laflamme found that the above solution is unstable to certain z -dependent perturbations. Specifically, they found that perturbations with wavelengths, λ_z , sufficiently large compared to the string radius grow exponentially. We also note that there is some evidence that black strings could have one or more additional unstable modes that preserve the z translational symmetry [104], but if this is the case, then the numerical results discussed below would suggest that such modes grow more slowly than those that break the symmetry.

In order to determine equations of motion for the dynamical evolution of a perturbed black string, we use the decomposition technique summarized in Sec. 1.1, but adapted for a 5-dimensional spacetime (so that we have a 4+1 decomposition). In addition, to minimize computational complexity and cost, we retain the spherical symmetry of (3.1), but allow the metric to have both t - and z -dependence in addition to the original r -dependence. Thus, we write the spacetime metric

as

$$ds^2 = (-\alpha^2 + h_{AB}\beta^A\beta^B) dt^2 + 2h_{AB}\beta^A dx^B dt + h_{AB}dx^A dx^B + h_\Omega d\Omega^2, \quad (3.2)$$

where the indices A and B range over the coordinates $\{r, z\}$, and the metric functions α , β^A , h_{AB} and h_Ω now generally depend on t , r and z . Our choice of the usual angular coordinates $\{\phi, \theta\}$, adapted to the spherical symmetry amounts to fixing 2 of the 5 degrees of coordinate freedom that we have in this problem. The three remaining degrees of freedom are fixed by choosing the lapse function, α , and the two non-trivial components of the shift vector, β^A . For all times, we choose α and β^z to be those associated with the static black string (3.1):

$$\alpha = (1 + 2M/r)^{-1/2}, \quad \beta^z = 0. \quad (3.3)$$

The last coordinate choice is used to maintain the condition $[h_\Omega/r^2](t, r) = [h_\Omega/r^2](0, r)$ for all times. This produces the following algebraic constraint on the shift vector component β^r :

$$\beta^r = \frac{2\alpha K_{\theta\theta}}{h_{\Omega,r}}. \quad (3.4)$$

The main motivation for choosing this particular gauge is to have well behaved coordinates that allow us to penetrate the horizon (as in [93] and [55]). This is crucial for our use of techniques that excise the region of the spacetime containing the singularity. We want to point out that a preliminary approach that fixed β^r to its black-string value for all times gave rise to coordinate singularities. In particular the radial position of the apparent horizon showed significant variation, approaching zero at late times. In order to decrease this variation, and in the spirit of the so called ‘‘horizon-locking’’ [93] coordinates we chose condition (3.4).

The field equations for our model are natural extensions of the 3+1 equations, summarized in Sec. 1.1, for the case of vacuum (vanishing stress-energy tensor). Specifically, the equations we need to solve are

$$H \equiv {}^{(4)}R + K^2 - K_{ij}K^{ij} = 0, \quad (3.5)$$

$$M_i \equiv D_j K_i^j - D_i K = 0, \quad (3.6)$$

$$\frac{\partial h_{ij}}{\partial t} = -2\alpha K_{ij} + D_j \beta_i + D_i \beta_j, \quad (3.7)$$

$$\begin{aligned} \frac{\partial K_{ij}}{\partial t} = & \alpha \left({}^{(4)}R_{ij} + K K_{ij} \right) - 2\alpha K_{ik} K_j^k - D_i D_j \alpha \\ & + D_i \beta^k K_{kj} + D_j \beta^k K_{ki} + \beta^k D_k K_{ij} + \alpha F^k{}_i F^m{}_j h_{km} H, \end{aligned} \quad (3.8)$$

where $F^k{}_i = -2\delta^k{}_r \delta^r{}_i$. Note that in the last equation, equation (3.8), the Hamiltonian constraint (1.18) has been added, and that this addition changes the structure of the principal parts of the differential operators involved in the equations. This has been done on the grounds that the

equations thus modified have better stability properties than the “bare” equations (see [51], [96], and [56] for reviews).

In order to efficiently study the non-linear dynamics resulting from the Gregory-Laflamme instability, we find it convenient to be able to macroscopically “perturb” the black string solution (3.1). We do so by altering h_Ω from its black string form. More specifically, at the initial time we set

$$\frac{h_\Omega}{r^2}(0, r, z) = 1 + A \sin\left(z \frac{2\pi q}{L}\right) e^{-(r-r_0)^2/\delta^2}. \quad (3.9)$$

Here, A is a measure of the strength of the perturbation—in particular, for $A = 0$ the perturbation vanishes and we recover the black string solution—and q is an integer that controls the spatial frequency in the z -direction. To complete the specification of the initial data for our evolutions, we set all remaining metric components, h_{ab} and K_{ab} —except for h_{rr} , K_{rr} and $K_{\theta\theta}$ —to their black-string values. The values of h_{rr} , K_{rr} and $K_{\theta\theta}$ are then determined from the constraint equations as described in more detail below.

3.3 Numerical Implementation

In this project we chose to perform *free* evolution, meaning that the constraint equations are only solved at the initial time. One motivation for this choice is that the solution of the Hamiltonian and momentum constraints, which are generally elliptic in nature, is computationally more costly than solving equations of evolution type. This is particularly the case when one wants to implement the numerical solution on massively parallel, distributed memory machines; parallelization of single-grid, finite-differenced evolution equations is straightforward, while parallel treatment of elliptic equations (or other equations with “long-range interactions”), may need to be quite intricate. Having solved the constraints at the initial time, we then follow the standard practice in numerical relativity of computing the residuals associated with the discrete constraints as time progresses as one measure of the error in the solution. Here we are exploiting the property that the evolution equations preserve the constraints at the continuum level, and that this property should be preserved by our discrete scheme—to the order of truncation error—provided that the scheme is stable [16].

3.3.1 Evolution

In our numerical implementation we fix the mass of the unperturbed black string to one, i.e. $M = 1$. A second order finite-difference, Crank-Nicholson treatment for the evolution equations is used, with the resulting algebraic equations for the update values solved using an iterative

process. This process consists of a constant number of iterations (3) and can be viewed as a specific predictor-corrector scheme for the evolved variables [100].

We discretize on a uniform grid, using coordinates (x, z) where $x = r/(1+r)$. Note that since $x = 1$ corresponds to $r = \infty$, we can actually set boundary conditions at i^0 (see Figure 1.2). This compactification of the radial coordinate proved crucial to the efficacy of our scheme; our computations done on a grid with finite range of the radial coordinate, $r \leq 0 \leq r_{\max}$, with the sort of approximate outgoing conditions often used in numerical relativity, lead to spurious results (including indications of time-independent, z -dependent solutions) which exhibited significant dependence on the specific value of r_{\max} chosen. The use of numerical dissipation of the Kreiss-Oliger form [52] was also essential to the stability of our numerical scheme, and was particularly important in two regions of the computational domain: close to the horizon of the black hole, as well as for $x \rightarrow 1$ (i.e. close to i^0), where the lack of spatial resolution caused outgoing disturbances to ultimately be represented near the Nyquist limit. In this latter case, the Kreiss-Oliger dissipation provides a natural and effective mechanism for “annihilating” the outgoing radiation while minimizing the amount of artificial reflection back into the interior of the computational domain.

Another important aspect of our implementation is the use of black hole excision [101]. As is the case for the 4-dimensional black hole discussed in Sec. 1.3, at $r = 0$ the black-string spacetime is singular: not only do some curvature terms go to infinity there, some of the metric coefficients blow-up as well. Dealing with such infinities numerically would seem to be fairly hopeless with current techniques, so to circumvent this problem, some region interior to the black string is excised from the computational domain. At the excision surface we do not need to set boundary conditions (this assumes that the time-locus of the interior boundary is either null or spacelike), and in practice we simply use a finite difference approximation of the evolution equations that employs appropriate one-sided difference formulae. The reason that this can work in principle is due to the fact that the interior of a black hole (or black string) *by definition* cannot influence the exterior, as discussed in Sec. 1.3. Now, for excision to work in practice, the excision surface needs to be chosen to be inside the event horizon. However, the event horizon is a *globally* defined structure—it cannot be located without knowledge of the entire spacetime. On the other hand the *apparent horizon* (the outer most marginally trapped surface) can be computed from quantities that are defined at a given instant of time and, assuming cosmic censorship, lies inside the event horizon [47]. In practice then, we locate the apparent horizon periodically and ensure that we are excising within this surface, and thus within the event horizon. The algorithm for locating the apparent horizon is described in detail in [18] and consists of a flow method that corrects the radius of an initial guess for the apparent horizon until the surface has an expansion below some specific tolerance. Specifically, if the radius of the apparent horizon is given by $r = R(z)$, the function $R(z)$ is corrected at every

iteration by

$$R^{n+1} = R^n - \theta_+ \Delta\tau \quad (3.10)$$

where R^{n+1} [R^n] is the value of $R(z)$ at iteration $n + 1$ [n], θ_+ is the outward null expansion at iteration n and $\Delta\tau$ is the time-step for the evolution of the flow.

As a final note, following the development of a stable, convergent serial (single processor) code, we constructed a parallel version using the CACTUS Computational Toolkit [11].

3.3.2 Determination of initial data: solving the constraints

As described previously, once the components of h_{AB} and K_{ab} that we have deemed to be freely specifiable are given at $t = 0$, we solve (3.5)–(3.6) for the initial values of the remaining geometric variables, h_{rr} , K_{rr} and $K_{\theta\theta}$. This solution proceeds by iteration—each pass is comprised of three distinct stages, each of which involves the solution of one of the constraints for the appropriate geometric quantity (i.e. one of h_{rr} , K_{rr} , $K_{\theta\theta}$) treating all other quantities, including the other two constrained functions, as fixed. This process is iterated until the ℓ_2 -norm (RMS value) of the residuals of all the equations falls below a certain tolerance. To initialize the iteration, we assign (unperturbed) black-string values to h_{rr} , K_{rr} and $K_{\theta\theta}$. At least for the weak perturbations (small A 's in equation (3.9)) considered in our study, this initialization is good enough to yield convergence for the iterative process.

We now describe this iterative solution process—in particular, the solution of each individual constraint equation—in more detail. The constraint equations are discretized on a uniform grid of points $\{x_i, z_j\}$ with $x_i = (i - 1)\Delta x$, $i = 1, \dots, N_x$, and $z_j = (j - 1)\Delta z$, $j = 1, \dots, N_z$. The mesh spacings in the x and z directions are $\Delta x \equiv x_{i+1} - x_i = 1/(2(N_x - 1))$ and $\Delta z \equiv z_{j+1} - z_j = L/(N_z - 1)$ respectively. We typically excise the region $x \leq 1/2$, corresponding to $r \leq M$, from the computational domain, i.e. the range of our coordinates is such that $x_1 = 1/2$, $x_{N_x} = 1$, $z_1 = 0$ and $z_{N_z} = L$. We first consider the Hamiltonian constraint (3.5), which in our coordinate system can be viewed as an equation for h_{rr} , and which has the form:

$$F_1 \frac{\partial h_{rr}}{\partial x} + F_2 h_{rr} \frac{\partial^2 h_{rr}}{\partial z^2} + F_3 h_{rr} \frac{\partial h_{rr}}{\partial z} + F_4 \left(\frac{\partial h_{rr}}{\partial z} \right)^2 + F_5 (h_{rr})^2 + F_6 h_{rr} = 0. \quad (3.11)$$

Here, the F_m , $m = 1, \dots, 6$, are functions that generally depend on all of the metric and extrinsic curvature components and their derivatives *except* h_{rr} (and its derivatives). We discretize this equation to second order in the mesh spacings using a difference approximation centered at the

points $(x_{i+1/2}, z_j)$. The resulting algebraic equations can be written as follows:

$$\begin{aligned}
(F_1)_{i+1/2,j} & \frac{[h_{rr}]_{i+1,j} - [h_{rr}]_{i,j}}{\Delta x} + \\
(F_2)_{i+1/2,j} & \frac{1}{2} ([h_{rr}]_{i+1,j} + [h_{rr}]_{i,j}) \\
& \frac{1}{2} \left[\frac{[h_{rr}]_{i,j+1} - 2[h_{rr}]_{i,j} + [h_{rr}]_{i,j-1}}{\Delta z^2} + \frac{[h_{rr}]_{i+1,j+1} - 2[h_{rr}]_{i+1,j} + [h_{rr}]_{i+1,j-1}}{\Delta z^2} \right] + \\
(F_3)_{i+1/2,j} & \frac{1}{2} ([h_{rr}]_{i+1,j} + [h_{rr}]_{i,j}) \frac{1}{2} \left[\frac{[h_{rr}]_{i+1,j+1} - [h_{rr}]_{i+1,j-1}}{2\Delta z} + \frac{[h_{rr}]_{i,j+1} - [h_{rr}]_{i,j-1}}{2\Delta z} \right] + \\
(F_4)_{i+1/2,j} & \left[\frac{1}{2} \left(\frac{[h_{rr}]_{i+1,j+1} - [h_{rr}]_{i+1,j-1}}{2\Delta z} + \frac{[h_{rr}]_{i,j+1} - [h_{rr}]_{i,j-1}}{2\Delta z} \right) \right]^2 + \\
(F_5)_{i+1/2,j} & \left[\frac{1}{2} ([h_{rr}]_{i+1,j} + [h_{rr}]_{i,j}) \right]^2 + (F_6)_{i+1/2,j} \left[\frac{1}{2} ([h_{rr}]_{i+1,j} + [h_{rr}]_{i,j}) \right] = 0. \quad (3.12)
\end{aligned}$$

Here $(F_m)_{i+1/2,j}$ are second order approximations of the functions F_m at points $(x_{i+1/2}, y_j)$. Assuming the values $[h_{rr}]_{i,j}, j = 1, 2, \dots, N_z$ are known, the above system can be viewed as a set of N_z non-linear algebraic equations for N_z unknowns $[h_{rr}]_{i+1,j}, j = 1, 2, \dots, N_z$. We can solve this non-linear set of equations using an N_z -dimensional Newton-Raphson method. Note that we thus solve the equations “line-by-line” in x_i , starting at the inner boundary, $i = 1$, which is chosen well within the horizon of the string (as mentioned above, typically at $r = M$ which amounts to $x_1 = 1/2$), and where the boundary values, $[h_{rr}]_{1,j}, j = 1, \dots, N_z$, are chosen to be those corresponding to an unperturbed black string. Also note that the algebraic systems obtained in the linearization of (4.38) are: (a) tridiagonal, due to the nearest-neighbor character of our second order finite difference approximations; and (b) cyclic, because of the imposed periodicity in the z -direction. These linear systems can be solved efficiently (in $O(N_z)$ time) using a cyclic tridiagonal linear solver [86].

We now turn attention to the r component of the momentum constraint (3.6), $M_r = 0$, which is viewed as an equation for $k_{\theta\theta} = K_{\theta\theta}/\alpha$ (the factor of α is introduced to more readily maintain regularity at spatial infinity). In terms of this function, $M_r = 0$ can be written as

$$G_1 \frac{\partial k_{\theta\theta}}{\partial x} + G_2 k_{\theta\theta} + G_3 = 0, \quad (3.13)$$

where, again, the functions $G_m, m = 1, 2, 3$, do not depend on $k_{\theta\theta}$ or its derivatives. Note that this equation does not contain any z -derivatives of $k_{\theta\theta}$ and thus, for any value of z , is an ordinary differential equation in x , which is moreover first order in x . We discretize (3.13) using

$$(G_1)_{i+1/2,j} \frac{[k_{\theta\theta}]_{i+1,j} - [k_{\theta\theta}]_{i,j}}{\Delta x} + (G_2)_{i+1/2,j} \frac{1}{2} ([k_{\theta\theta}]_{i+1,j} + [k_{\theta\theta}]_{i,j}) + (G_3)_{i+1/2,j} = 0, \quad (3.14)$$

which is a second order approximation centred at the point $(x_{i+1/2}, z_j)$. For any value of z_j , and assuming that the values $[k_{\theta\theta}]_{i+1,j}$ are known, the above algebraic equations can be solved for

$[k_{\theta\theta}]_{i,j}$. The boundary conditions $[k_{\theta\theta}]_{N_x,j}$, $j = 1, \dots, N_z$, at $x = 1$ (i_0) are again fixed to their (unperturbed) black string values.

The last constraint equation, $M_z = 0$, is considered to be an equation for $k_{rr} = r^2 K_{rr}/\alpha$ (again, the scaling of the extrinsic curvature component by r^2/α is motivated by regularity considerations at $x = 1$):

$$H_1 \frac{\partial k_{rr}}{\partial z} + H_2 k_{rr} + H_3 = 0. \quad (3.15)$$

Once more, the functions H_m , $m = 1, 2, 3$, do not involve k_{rr} or its derivatives. This equation has the same structure as (3.13), but with the roles of x and z reversed, so that we now have, for any value of x , an ODE in z that we must solve. The second-order discretization used in this case is centred at points $(x_i, z_{j+1/2})$:

$$(H_1)_{i,j+1/2} \frac{[k_{rr}]_{i,j+1} - [k_{rr}]_{i,j}}{\Delta z} + (H_2)_{i,j+1/2} \frac{1}{2} ([k_{rr}]_{i,j+1} + [k_{rr}]_{i,j}) + (H_3)_{i,j+1/2} = 0. \quad (3.16)$$

In order to solve these equations, we again set the boundary conditions $[k_{rr}]_{i,1}$, $i = 1, \dots, N_x$ to their black string values computed at $z = z_{\min}$, then solve for increasing values of j .

3.3.3 Finding Event Horizons

As explained before, it is not possible to calculate the intersection of an event horizon with a given spacelike slice of a spacetime without knowledge of the entire spacetime. Specifically, in order to locate an event horizon one must determine the causal past of future null infinity, which in effect means determining the origin of all null geodesics that reach \mathcal{I}^+ . Any region of spacetime not contained in the causal past of \mathcal{I}^+ (i.e. the “exterior universe”) lies within a black hole, by definition, and the surfaces separating black hole interiors from the exterior universe are the event horizons.

For the purposes of the black string calculations, it is interesting to attempt to study the actual dynamics of the event horizon—i.e. the time history of the intersection of the event horizon with our spacelike hypersurfaces, so a method that provides a good approximation to the location of the event horizon is needed. Here we describe one technique that we have used, following [49], to do just that. The method involves approximating the location of the boundary of the causal past of some $r = \text{constant}$ surface by following radial null rays.

We first derive equations for certain null rays in our spacetime. In particular, an appropriate Lagrangian for radial rays (i.e. no motion in the z direction) in our coordinate system is

$$\mathcal{L} = (-\alpha^2 + h_{rr}\beta^{r^2}) (t')^2 + 2h_{rr}\beta^r t' r' + h_{rr} (r')^2, \quad (3.17)$$

where the prime denotes differentiation with respect to some affine parameter λ . Since we are interested in null trajectories, we set $\mathcal{L} = 0$. The equation for the radial position of the null rays

is then

$$\dot{r} = \pm \frac{\alpha}{\sqrt{h_{rr}}} - \beta^r \equiv R(t, r, z), \quad (3.18)$$

where the plus [minus] sign corresponds to outgoing [ingoing] null rays respectively. Note that this equation is expressed in terms of derivatives with respect to the coordinate time t , which are denoted by an overdot. Once the evolution of the spacetime has been calculated, equation (3.18) for the outgoing case is integrated *backwards in time*, for all values of z_j , with initial conditions $r = r_0$ at the maximum time t_{\max} achieved in the evolution. We chose r_0 to be outside the horizon and close to $x = 1$, as an approximation to \mathcal{I}^+ , or inside the horizon and close to the excision surface. In both cases, at least for our spacetimes, the evolution backwards in time accumulates at the event horizon. The integration is done using a second order Runge-Kutta scheme. Specifically, for a ray with constant coordinate z_j , in order to calculate r^n (the radial position at time t^n) from the value r^{n+1} (the radial position at time t^{n+1}) with $t^n = t^{n+1} - \Delta t$ we use the following approximation:

$$k_1 = -\Delta t R(t^{n+1}, r^{n+1}, z), \quad (3.19)$$

$$k_2 = -\Delta t R(t^{n+1} - 1/2\Delta t, r^{n+1} + 1/2k_1, z), \quad (3.20)$$

$$r^n = r^{n+1} + k_2. \quad (3.21)$$

Here, R is defined by the right hand side of equation (3.18). In order to calculate $R(t^{n+1}, r^{n+1}, z)$ and $R(t^{n+1} - 1/2\Delta t, r^{n+1} + 1/2k_1, z)$ we need to determine values of α , β^r and h_{rr} at those coordinate positions. Since the functional form of α is specified *a priori*, we can use that closed-form specification for the needed lapse values. In order to calculate the required values of β^r and h_{rr} , we use second-order (bi-linear) interpolation in the (x_i, z_j) mesh.

Notice that integration of the equations of motion for the rays backwards in time does not give us all of the causal past of $r = r_0$, but only the part of the past that can be reached by purely radial rays. However, we believe that for the spacetimes that we have computed, and particularly since the event horizon is an attractor with respect to backwards integration, tracking these rays allows us to rather accurately locate the horizon. For related discussions of approximate event horizon location in the axisymmetric, four-dimensional case, see [12], [49],[60]. Finally, we should point out that the technique of *backwards* integration is absolutely crucial to the accuracy and efficiency of this strategy—*forward* integration of outgoing null rays becomes an increasingly ill-posed problem (especially at the numerical level) for rays emanating from regions closer and closer to the event horizon.

3.4 Results

Our code was thoroughly tested and showed second order convergence in the mesh spacings as expected. In particular, second order convergence of independent discretizations of the equations of motion was demonstrated, as was second order convergence of the discrete constraint equation residuals. This provides a stringent test of the correctness of our implementation.

All of the calculations performed in this study have initial data as defined by (3.9) with specific parameter values $A = 0.1$, $q = 1$, $r_0 = 2.5$ and $\delta_r = 0.5$. Using these parameters, we have been able to recover the main perturbative results found by Gregory and Laflamme [37]. Specifically, we found a critical value L_c for the string length which is within 2% of the value reported by Gubser [39], $L_c \approx 14.3M$. Fig. 3.1 shows the maximum, R_{\max} , and minimum, R_{\min} , values of the areal radius of the the apparent horizon, as well as the following parameter defined in [39]:

$$\lambda \equiv \frac{1}{2} \left(\frac{R_{\max}}{R_{\min}} - 1 \right). \quad (3.22)$$

In the figure one can see that for a string length marginally larger than the critical value, L_c , the apparent horizon gets increasingly distorted as the evolution proceeds, i.e. the maximum value of the areal radius grows while the minimum decreases. On the other hand, for a value of L slightly smaller than L_c , the evolution is evidently (physically) stable.

In order to most efficiently study the non-linear regime in an attempt to determine the ultimate fate of an unstable black string, we want to have the instability growing as fast as possible. We thus decided to study configurations with a string length $L = 1.4L_c$ since perturbation theory predicts that the fastest growing mode has a wavelength close to that value [37].

In Fig. 3.2 we show sequences of embedding diagrams illustrating the evolution of the apparent horizon for a calculation with $L = 1.4L_c$. In this diagram angular dimensions have been suppressed, and new coordinates (\bar{r}, \bar{z}) are used so that the coordinate distance along the curve corresponds to proper distance along the apparent horizon. From these plots, we can get some sense of how the perturbation grows, and how there are indications that the late-time solution may be approaching a series of black holes connected by thin black strings.

Unfortunately our code crashes soon after the last frame shown in Fig. 3.2 (and such crashes are generic in our late time evolutions of unstable black strings). Thus we *cannot* conclude that this chain of black holes connected with a thin black strings is truly indicative of the final state, not least since the spacetime is still highly time-dependent at the time of the crash. Investigation of the behavior of the dynamical variables as $t \rightarrow t_{\text{crash}}$ indicates that the break-down is due to a coordinate pathology. First, we find that t_{crash} is not significantly dependent on the mesh spacings Δx and Δz . This suggests that a numerical instability is not responsible for the

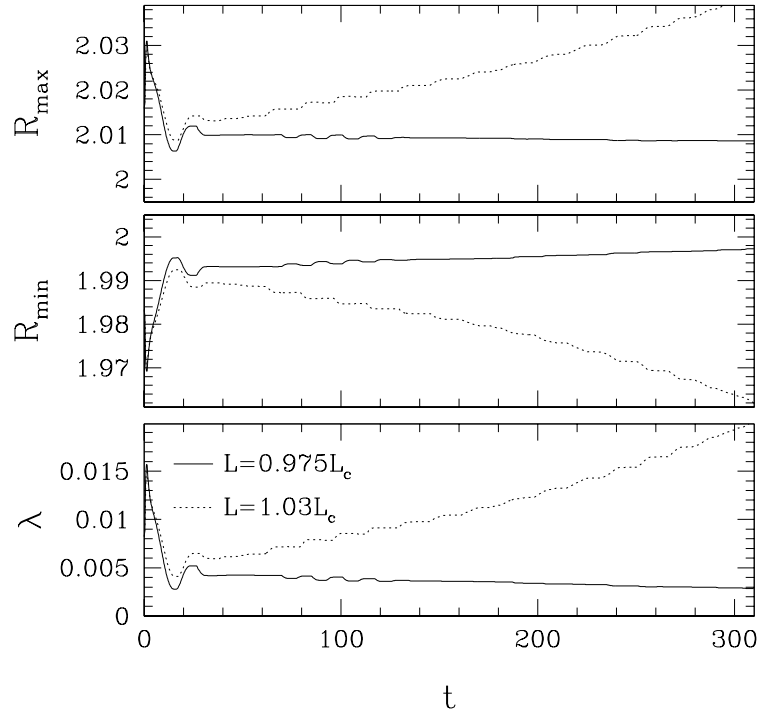


Figure 3.1: Values of the maximum, R_{\max} , and minimum, R_{\min} , areal radius of the apparent horizon as a function of coordinate time for two values of the string length. This calculation has been done for a black string with $M = 1$. The dotted line corresponds to a string length larger than the critical value, $L = 1.03L_c$: one can clearly see the increase of R_{\max} and decrease of R_{\min} as a function of time. The continuous line corresponds to a string length smaller than the critical value, $L = 0.975L_c$. In this case the evolution is stable and the small temporal variations observed can be understood in terms of a combination of numerical errors and the “relaxation” of the black string from a slightly excited state induced by the perturbation.

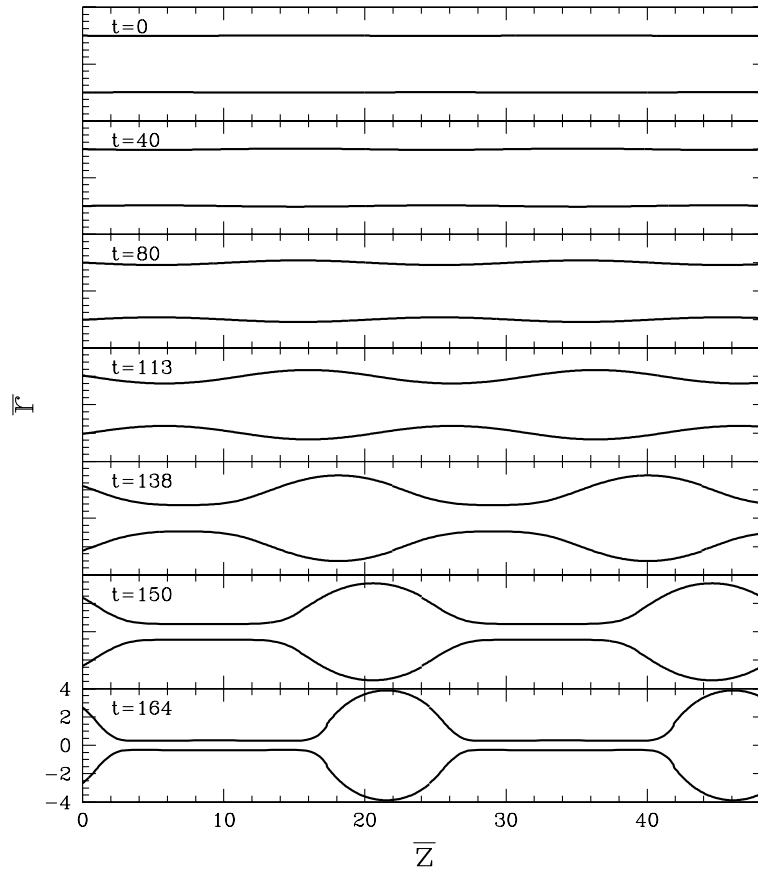


Figure 3.2: This figure shows snapshots of the apparent horizon, computed in coordinates such that coordinate length of the curve corresponds to proper length along the apparent horizon, and where the two angular dimensions have been suppressed. Note that the figure extends for two periods in z (i.e. the z -span is $2L = 2.8L_c$), and that the portion of the curve plotted for negative values of \bar{r} is included only for better visualization of the horizon dynamics.

crash. Second, curvature scalars are calculated, and they appear to remain finite at all events of the evolution indicating that no physical singularity is produced within the computational domain.

Finally, to this point in the analysis, only the dynamics of the apparent horizon, and not the event horizon, has been considered. However, Fig. 3.3 shows a comparison of results computed using the approximate event-horizon-locator described in Sec. 3.3.3, and those from apparent horizon location. For the event horizon location, outgoing null rays are traced back in time from 3 different “initial” (actually final) surfaces. Two of these surfaces are defined by $r_1 = 10$, $r_2 = 4$ and lie outside the apparent horizon, while the third is 5 grid points (in our numerical coordinate x_i) away from the excision surface and inside the position of the apparent horizon. The figure shows how quickly the null surfaces traced backwards from the initial cylinders converge to one another, as well as to the apparent horizon. This indicates that the apparent horizon is indeed a good approximation to the intersection of the event horizon with a given spacelike hypersurface in the spacetimes we have constructed.

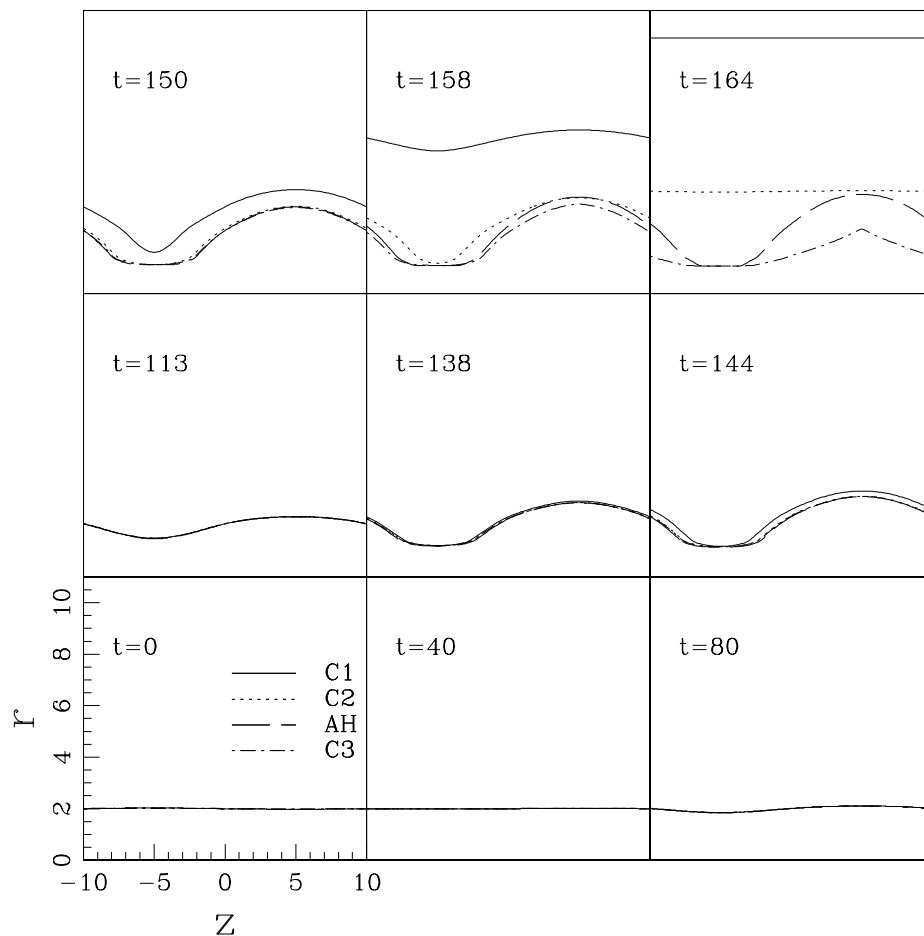


Figure 3.3: Plots of the apparent horizon (labeled AH) and estimates of the event horizon location (C1, C2 and C3) in coordinate space (in contrast to the embedding coordinates used in Fig. 3.2). Here, the C1 (C2) curve marks the evolution of the outgoing radial null rays for the final $t = 164$ surface with $r_0 = 10$ ($r_0 = 4$). C3 denotes the evolution of outgoing radial null rays, emanating from a surface just inside the apparent horizon at $t = 164$. Thus, moving backwards in time, these curves should asymptote towards the event horizon of the spacetime. These plots suggest that for most of the evolution (at least), the apparent horizon is an excellent approximation to the event horizon.

Chapter 4

General Relativistic Hydrodynamics in Spherical Symmetry

4.1 Introduction

In this chapter we describe the code we have developed for solving the fully coupled equations of general relativistic hydrodynamics in spherical symmetry.

From the pioneering work of May and White [68] to more recent codes using HRSC methods, such as that described in Noble's thesis [79], there have been many different implementations of spherically symmetric general relativistic hydrodynamics that have been used to study a wide variety of problems. These problems include supernova explosions [68], [98], the structure of neutron stars [91], and critical collapse [78], [46], [79]. Overall, these studies have been very successful and many results have been obtained. We view our development of yet another spherically symmetric relativistic code as a logical first step towards our ultimate goal of studying axisymmetric self-gravitating hydrodynamics. The spherically symmetric code serves two main roles: (a) it allows us to experiment with the same formalism, and numerical schemes, as well as the same type of coordinates used in the axisymmetric case, within the context of a much simpler model; and (b) it provides us with the means of computing "benchmark" results that can be used to test and calibrate an axisymmetric code, provided that spherically symmetric initial data is evolved by the latter. In the spirit of (a), the code has proven to be quite useful since it has allowed us to identify an appropriate set of variables describing the state of the fluid, so that geometric constraint equations actually have solutions in the strong-field regime. We note that existence of solutions is not always guaranteed for the case of non-linear elliptic equations, as emphasized by York [115] for the particular case of the constraints of general relativity.

The remainder of this chapter is organized as follows. In Sec. 4.2 and using the $3 + 1$ decom-

position explained in Sec. 1.1, we discuss the equations that determine the geometry, as well as the Valencia formalism for the treatment of the fluid variables (see Sec. 1.4 and App. A). In the following section, we detail the numerical approach used to solve the equations, focusing on the HRSC method and finite-volume discretization used for the hydrodynamics. In 4.4.1 we explain the problem we encountered using a standard approach to solve the geometric constraint equations to determine initial data, and describe how this problem was resolved through the introduction of new dynamical variables for the fluid. Finally, in Sec. 4.4, we summarize some of the tests that have been performed in order to check the reliability of our numerical implementation.

4.2 Model/Equations

As discussed in Sec. 1.4 a perfect fluid has a stress energy tensor of the form

$$T^{\mu\nu} = \rho_0 h u^\mu u^\nu + P g^{\mu\nu}, \quad (4.1)$$

where ρ_0 is the rest mass density, h is the specific enthalpy, P is the pressure and u^μ is the fluid four velocity. Note that the specific enthalpy h can be written in terms of the specific internal energy, ϵ , as $h = 1 + \epsilon + P/\rho_0$.

For this study, we choose so-called *maximal/isotropic* coordinates in which the spherically symmetric, time dependent metric takes the 3+1 form

$$ds^2 = [-\alpha(t, r)^2 + \psi(t, r)^4 \beta(t, r)^2] dt^2 + 2\psi^4 \beta dt dr + \psi^4 [dr^2 + r^2 (d\theta^2 + \sin^2 \theta d\phi^2)]. \quad (4.2)$$

As in our study of scalar collapse in Chap. 2, we adopt angular coordinates θ and ϕ that are adapted to the spherical symmetry. The radial coordinate, r , is fixed by demanding that the 3-metric be conformally flat, and the time slicing is fixed by requiring that the slices be *maximal*, which means that the trace of the extrinsic curvature vanishes

$$\text{Tr} [K_{ij}] = K^i_i = K^r_r + K^\theta_\theta + K^\phi_\phi = K^r_r + 2K^\theta_\theta = 0. \quad (4.3)$$

As we will see, this last relation provides an equation for the lapse function that must be solved on each slice as the evolution proceeds. We choose this specific gauge since it is the natural restriction to spherical symmetry of the coordinates used in our axisymmetric implementation, which in turn are based on the coordinates used in [19].

Following [30], and references within, we now introduce hydrodynamic variables as follows

$$D = \rho_0 W, \quad (4.4)$$

$$S_r = \rho_0 h W^2 v_r, \quad (4.5)$$

$$E = \rho_0 h W^2 - P, \quad (4.6)$$

$$\tau = E - D, \quad (4.7)$$

$$v^r = \frac{u^r}{\alpha u^0} + \frac{\beta}{\alpha}, \quad (4.8)$$

$$W = \alpha u^t = (1 - v_r v^r)^{-1/2}. \quad (4.9)$$

We note that the definitions of D , S_r and τ are motivated by our desire to cast the fluid equations into conservation form, as briefly described in Sec. 1.4. Moreover, in our adopted system of coordinates, it is convenient to rescale these variables by an appropriate power of ψ (as we explain in more detail in Sec. 4.4.1). In particular, we will use rescaled variables $\tilde{D} = \psi^6 D$, $\tilde{S}_r = \psi^6 S_r$, $\tilde{\tau} = \psi^6 \tau$ and $\tilde{P} = \psi^6 P$.

Using the 3+1 formalism outlined in Sec. 1.1, we now derive the equations that will determine the geometric variables. Due to our restriction to spherical symmetry, as well as to our choice of coordinates, we can implement a fully-constrained evolution—wherein all geometric quantities are determined at all times either from the coordinate conditions themselves, or from the constraint equations—and we choose to do so.

Given the form of the metric (4.2), and the demand that $K^i_i = 0$, the Hamiltonian constraint (1.18) can be written as

$$\psi'' + \frac{2}{r}\psi' + \frac{3}{16}K^r_r{}^2\psi^5 + 2\pi\frac{(\tilde{\tau} + \tilde{D})}{\psi} = 0, \quad (4.10)$$

while the r component of the momentum constraint gives

$$(K^r_r)' + 3\frac{(r\psi^2)'}{r\psi^2}K^r_r - 8\pi\frac{\tilde{S}_r}{\psi^6} = 0. \quad (4.11)$$

In addition, the coordinate conditions give us two more equations. First, the slicing condition, derived from the demand that (4.3) hold for all t is

$$\frac{1}{r^2\psi^2} [(r^2\psi^2)\alpha'] - \left(\frac{3}{2}\psi^4 (K^r_r)^2 + 4\pi\frac{(\tilde{D} + \tilde{\tau} + 3\tilde{P})}{\psi^2} + 4\pi\frac{\tilde{S}_r^2}{\psi^6(\tilde{\tau} + \tilde{D} + \tilde{P})} \right) \alpha = 0, \quad (4.12)$$

and fixes the lapse at each time. Second, the requirement that the equations for $\dot{\gamma}_{rr}$ and $\dot{\gamma}_{\theta\theta}/r^2$ (which in the 3+1 approach follow immediately from the definition of the extrinsic curvature

components (1.23)) be equal, so that conformal 3-flatness is preserved in time, provides the following ODE (ordinary differential equation) for the single non-trivial shift vector component, $\beta \equiv \beta^r$:

$$\frac{2}{3} \frac{r}{\alpha} \left(\frac{\beta}{r} \right)' = K^r{}_r. \quad (4.13)$$

These complete the set of geometric equations needed to perform the evolution. In addition, we have an evolution equation for the conformal factor which, again, follows from the definition of the extrinsic curvature component, $K^r{}_r$:

$$\dot{\psi} = -\frac{\alpha}{2} \psi K^r{}_r + \psi' \beta + \frac{1}{2} \psi \beta'. \quad (4.14)$$

The hydrodynamical equations can be calculated from local conservation of the fluid stress tensor

$$(T^{\mu\nu})_{;\mu} = 0, \quad (4.15)$$

as well as local conservation of the particle number

$$(J^\mu)_{;\mu} = 0. \quad (4.16)$$

Again, given our restriction to spherical symmetry, two independent equations can be derived from (4.15)

$$\begin{aligned} & \frac{1}{\sqrt{-g}} \frac{\partial}{\partial t} \left(\frac{\sqrt{h}}{\psi^6} \tilde{S}_r \right) + \frac{1}{\sqrt{-g}} \frac{\partial}{\partial r} \left\{ \frac{\sqrt{-g}}{\psi^6} \left[\tilde{S}_r \left(v^r - \frac{\beta}{\alpha} \right) + \tilde{P} \right] \right\} = \\ & \frac{1}{\psi^6} \left\{ \left[6\tilde{P} + 2 \frac{\tilde{S}_r^2}{\psi^4 (\tilde{\tau} + \tilde{D} + \tilde{P})} \right] \frac{\psi'}{\psi} + \tilde{S}_r \frac{\beta'}{\alpha} - (\tilde{\tau} + \tilde{D}) \frac{\alpha'}{\alpha} + 2 \frac{\tilde{P}}{r} \right\}, \end{aligned} \quad (4.17)$$

$$\begin{aligned} & \frac{1}{\sqrt{-g}} \frac{\partial}{\partial t} \left(\frac{\sqrt{h}}{\psi^6} \tilde{\tau} \right) + \frac{1}{\sqrt{-g}} \frac{\partial}{\partial r} \left\{ \frac{\sqrt{-g}}{\psi^6} \left[\tilde{\tau} \left(v^r - \frac{\beta}{\alpha} \right) + \tilde{P} v^r \right] \right\} = \\ & \frac{1}{\psi^6} \left\{ -\frac{\tilde{S}_r}{\psi^4} \frac{\alpha'}{\alpha} - 2\tilde{P} \frac{\beta'}{\alpha} + \left[3\tilde{P} + \frac{\tilde{S}_r^2}{\psi^4 (\tilde{\tau} + \tilde{D} + \tilde{P})} \right] K^r{}_r + 2 \frac{\tilde{P}\beta}{r\alpha} \right\}. \end{aligned} \quad (4.18)$$

Here g is the determinant of the metric (4.2), so that $\sqrt{-g} = \alpha \psi^6 r^2 \sin \theta$. Equations (4.17) and (4.18) represent local conservation of momentum and energy, respectively. From the particle conservation equation (4.16) we get

$$\frac{1}{\sqrt{-g}} \frac{\partial}{\partial t} \left(\frac{\sqrt{h}}{\psi^6} \tilde{D} \right) + \frac{1}{\sqrt{-g}} \frac{\partial}{\partial r} \left\{ \frac{\sqrt{-g}}{\psi^6} \left[\tilde{D} \left(v^r - \frac{\beta}{\alpha} \right) \right] \right\} = 0. \quad (4.19)$$

In summary, the complete set of differential hydrodynamical equations that is discretized in

Sec. 2.3.1 is

$$\frac{1}{\alpha r^2} \frac{\partial}{\partial t} (r^2 \tilde{D}) + \frac{1}{\alpha r^2} \frac{\partial}{\partial r} \left\{ \alpha r^2 \left[\tilde{D} \left(v^r - \frac{\beta}{\alpha} \right) \right] \right\} = 0, \quad (4.20)$$

$$\begin{aligned} \frac{1}{\alpha r^2} \frac{\partial}{\partial t} (r^2 \tilde{S}_r) + \frac{1}{\alpha r^2} \frac{\partial}{\partial r} \left\{ \alpha r^2 \left[\tilde{S}_r \left(v^r - \frac{\beta}{\alpha} \right) + \tilde{P} \right] \right\} = \\ \left[6\tilde{P} + 2 \frac{\tilde{S}_r^2}{\psi^4 (\tilde{\tau} + \tilde{D} + \tilde{P})} \right] \frac{\psi'}{\psi} + \tilde{S}_r \frac{\beta'}{\alpha} - (\tilde{\tau} + \tilde{D}) \frac{\alpha'}{\alpha} + 2 \frac{\tilde{P}}{r}, \end{aligned} \quad (4.21)$$

$$\begin{aligned} \frac{1}{\alpha r^2} \frac{\partial}{\partial t} (r^2 \tilde{\tau}) + \frac{1}{\alpha r^2} \frac{\partial}{\partial r} \left\{ \alpha r^2 \left[\tilde{\tau} \left(v^r - \frac{\beta}{\alpha} \right) + \tilde{P} v^r \right] \right\} = \\ - \frac{\tilde{S}_r}{\psi^4} \frac{\alpha'}{\alpha} - 2\tilde{P} \frac{\beta'}{\alpha} + \left[3\tilde{P} + \frac{\tilde{S}_r^2}{\psi^4 (\tilde{\tau} + \tilde{D} + \tilde{P})} \right] K^r_r + 2 \frac{\tilde{P}\beta}{r\alpha}. \end{aligned} \quad (4.22)$$

As usual, the above differential equations need to be supplemented with regularity and boundary conditions. At $r = 0$ the following regularity conditions are imposed:

$$\psi'(t, 0) = 0, \quad (4.23)$$

$$\alpha'(t, 0) = 0, \quad (4.24)$$

$$K^r_r(t, 0) = 0, \quad (4.25)$$

$$\beta(t, 0) = 0, \quad (4.26)$$

$$D'(t, 0) = 0, \quad (4.27)$$

$$S_r(t, 0) = 0, \quad (4.28)$$

$$\tau'(t, 0) = 0. \quad (4.29)$$

As was the case for our study of scalar collapse, we will approximately solve our equations of motion on a spatially finite computational domain, $0 \leq r \leq r_{\max}$. For the geometric variables, we impose boundary conditions based on the requirement that spacetime be asymptotically flat in the limit $r \rightarrow \infty$, and that our time slices be labelled so that coordinate time coincides with proper time at infinity. Specifically, we must then have

$$\lim_{r \rightarrow \infty} \psi(t, r) = 1 + \frac{A(t)}{r} + O(r^{-2}), \quad (4.30)$$

$$\lim_{r \rightarrow \infty} \alpha(t, r) = 1 + \frac{B(t)}{r} + O(r^{-2}), \quad (4.31)$$

$$\lim_{r \rightarrow \infty} \beta(t, r) = \frac{C(t)}{r} + O(r^{-2}), \quad (4.32)$$

where $A(t)$, $B(t)$, $C(t)$ are general functions of time (which in practice are not independent of each other). Following standard practice in numerical relativity [116], these fall off conditions (4.30–4.32)

can be expressed as the following mixed (or Robin) boundary conditions,

$$\frac{\partial\psi}{\partial r} + \frac{(\psi - 1)}{r} = O(r^{-3}) \approx 0, \quad (4.33)$$

$$\frac{\partial\alpha}{\partial r} + \frac{(\alpha - 1)}{r} = O(r^{-3}) \approx 0, \quad (4.34)$$

$$\frac{\partial\beta}{\partial r} + \frac{\beta}{r} = O(r^{-3}) \approx 0, \quad (4.35)$$

which are independent of the particular form of the functions $A(t)$, $B(t)$, $C(t)$. This technique allows us to implement (4.30–4.32) using (4.33–4.35) without previous knowledge of these functions. Alternatively, we also have used the following outer boundary condition for $\alpha(t, r)$:

$$\lim_{r \rightarrow \infty} \alpha(t, r) = \frac{1 - M(t, r)/(2r)}{1 + M(t, r)/(2r)}, \quad (4.36)$$

where $M(t, r) = 2r(\psi(t, r) - 1)$. This value corresponds to the value of the lapse for the Schwarzschild solution written in isotropic coordinates.

For the fluid, we use boundary conditions based on the demand that the flow be purely outgoing at the boundary. We approximate this condition by assuming that the derivative of the conservation variables is zero at and beyond the boundary of the computational domain. At the discrete level we implement this condition using ghost cells, see Fig. 4.1, where we copy the values of the ghost-cell conservation variables from the last physical cell.

The hydrodynamical equations derived above do not completely fix the evolution of the fluid; we must close the set of equations by specifying a functional relationship between the pressure on one hand, and the energy and particle densities on the other; i.e. we must fix an equation of state. In this thesis we restrict attention to the so-called ideal fluid equation of state (EOS)

$$P = (\Gamma - 1) \rho_0 \epsilon, \quad (4.37)$$

where Γ is the adiabatic index that will be taken to be a constant in the range $(1, 2]$. This choice of equation of state, which is an extension of $P = (k_B/m)\rho_0 T$ (k_B being the Boltzmann constant) see [13] and [99], admits stationary solutions (in contrast to the ultrarelativistic EOS, $P = (\Gamma - 1)\rho_H$, for example). This is a key feature which makes it a popular choice in relativistic hydrodynamics [30].

In ending this section, we reemphasize that we have introduced so-called *conservative variables* $\mathbf{q} = \{D, S, \tau\}$, in order to cast the fluid equations in conservation law form, i.e. in the form of (1.40). In particular, the conservative variables are in no sense independent of the *primitive variables*, $\mathbf{p} = \{\rho_0, v^r, P\}$ (or equivalently $\{\rho_0, v^r, \epsilon\}$), but rather are functionally related to the primitive quantities via equations (4.4)–(4.9).

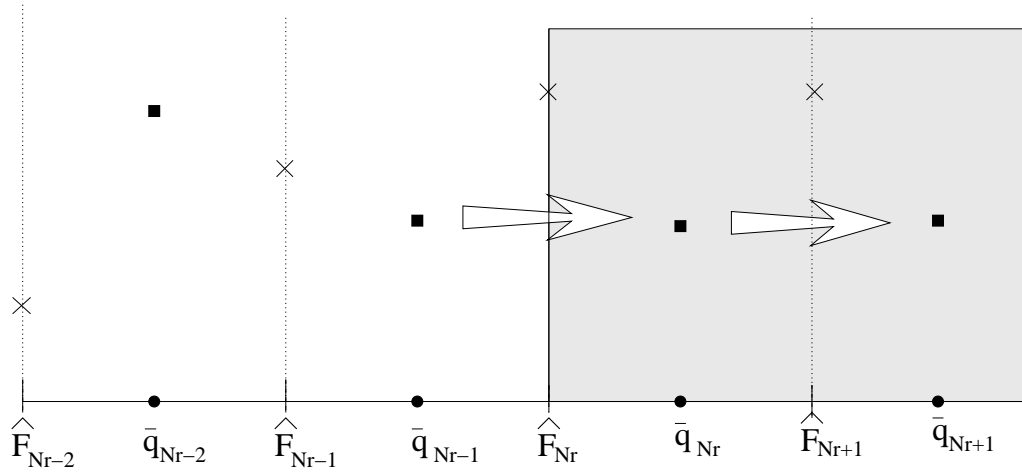


Figure 4.1: In this diagram we show the cells near the boundary of the computational domain in our numerical scheme. The squares denote the discrete values for the conservation variables and the crosses denote the values of the fluxes. We approximate the outflow boundary condition using ghost cells (shaded on the figure): the values of the conservation variables in the ghost cells are identical to the values in the last physical cell.

4.3 Numerics

We now describe the algorithm used to solve the coupled system of equations presented in the previous section. We have already noted that due to the symmetry of the problem and to our choice of coordinates, the geometric variables on a given hypersurface Σ_t can be calculated without resort to equations of evolutionary type, assuming that the values of the hydrodynamical variables are known at that time. In order to calculate the solution on a future hypersurface, $\Sigma_{t+\Delta t}$, we adopt an iterative process. The iteration consists of the following main steps:

1. Make an initial estimate for the geometric variables $\{G_i^{n+1}\}$ at time $t + \Delta t$.
2. Treating the advanced values of the geometric variables as known quantities, evolve the fluid equations to get estimates of the fluid fields $\{Q_j^{n+1}\}$ at $t + \Delta t$.
3. Treating the advanced values of the fluid variables as known quantities, solve the constraint equations to correct the values of $\{G_i^{n+1}\}$.

Here $\{G_i^{n+1}, i = 1, 2, 3\} = \{\alpha, \beta, \psi\}$ and $\{Q_j^{n+1}, j = 1, 2, 3\} = \{\tilde{D}, \tilde{S}_r, \tilde{\tau}\}$, and are evaluated at the advanced discrete time, $t = t + \Delta t$. The two last steps are repeated until the ℓ_2 norm of the

difference between the values of the fluid variables from two successive iterations is below some tolerance (typically 10^{-10}).

In the remainder of this section, we first discuss the numerical solution of the geometric equations (4.10–4.13), and then the numerical treatment of the hydrodynamical equations (4.17–4.19). The geometric equations (which are all ordinary differential equations in r) are solved using second order finite difference techniques. The fluid equations, on the other hand, are solved using a finite volume approach first developed by Godunov [36], which exploits the fact that the equations are written in conservation law form.

4.3.1 Geometric Equations

We first note that, in accord with our 3+1 decomposition of the Einstein equations, neither of the constraint equations (4.10) nor (4.11) involves the lapse function, α or the shift vector component, β (the “kinematical” gravitational variables). Thus, to solve for the geometric variables, we first view the constraints as a system of 2 coupled ODEs for the quantities ψ and K^r_r , then solve that system iteratively, as described below. Once ψ and K^r_r have been determined, (4.12) and (4.13) can be solved for α and β , respectively.

In order to finite-difference the geometric equations, we introduce a uniform spatial grid $\{r_1, r_2, \dots, r_i, \dots, r_{N_r}\}$, where $r_{i+1} = r_i + \Delta r$, Δr is the constant mesh spacing, $r_1 = r_{\min} = 0$, and $r_{N_r} = r_{\max}$ is the outer boundary of the computational domain. Adopting the usual finite difference notation $f_i \equiv f(r_i)$, we use the following second-order ($O(\Delta r^2)$) finite difference approximation of the constraint equations

$$\begin{aligned} \frac{-3\psi_1 + 4\psi_2 - \psi_3}{2\Delta r} &= 0, & (4.38) \\ \frac{\psi_{i+1} - 2\psi_i + \psi_{i-1}}{\Delta r^2} + \frac{2}{r_i} \frac{\psi_{i+1} - \psi_{i-1}}{\Delta r} + \frac{3}{16} (K^r_r)_i^2 \psi_i^5 + 2\pi \frac{(D_i + \tau_i)}{\psi_i} &= 0, & i = 2, \dots, N_r - 1, \\ \frac{\psi_{N_r} - 1}{r_{N_r}} + \frac{3\psi_{N_r} - 4\psi_{N_r-1} + \psi_{N_r-2}}{2\Delta r} &= 0, \end{aligned}$$

$$\begin{aligned} K_1 &= 0, & (4.39) \\ \frac{(K^r_r)_{i+1} - (K^r_r)_i}{\Delta r} + 6 \frac{r_{i+1}\psi_{i+1}^2 - r_i\psi_i^2}{\Delta r (r_{i+1}\psi_{i+1}^2 + r_i\psi_i^2)} \frac{1}{2} [(K^r_r)_{i+1} + (K^r_r)_i] \\ - 8\pi S_{r_{i+1/2}} &= 0, & i = 1, \dots, N_r - 1. \end{aligned}$$

These two sets of equations are solved iteratively by first updating the $\psi_i, i = 1, 2, \dots, N_r$, assuming the $(K^r_r)_i, i = 1, 2, \dots, N_r$ are known, then updating the $(K^r_r)_i$ assuming the ψ_i are known. Fixing the values $(K^r_r)_i$, equations (4.38) comprise a non-linear *system* for the unknowns

ψ_i . This system is solved using a (global) N_r -dimensional Newton-Raphson method, where at each Newton step all N_r values ψ_i are simultaneously updated. Each of these updates requires the solution of a tridiagonal linear system, which is accomplished using a standard LAPACK routine [2]. In the second stage of the constraint-iteration, given the boundary (regularity) condition (4.25), equations (4.39) are solved using a pointwise Newton method for each of the unknowns $(K^r_r)_{i+1}$, $i = 1, 2, \dots, N_r - 1$.

We note that it would be possible to implement a scheme whereby both systems (4.38) and (4.39) are solved simultaneously using a global Newton iteration. The banded systems (bandwidth ~ 6) that would need to be solved at each Newton step could still be solved in $O(N_r)$ time. However, we have not explored this option.

The slicing condition is treated using a second order discretization similar to that used for the Hamiltonian constraint:

$$\begin{aligned} \frac{-3\alpha_1 + 4\alpha_2 - \alpha_3}{2\Delta r} &= 0, & (4.40) \\ \frac{3}{\psi_i^2} \frac{(\alpha_{i+1} - \alpha_i) r_{i+1/2}^2 \psi_{i+1/2}^2 - (\alpha_i - \alpha_{i-1}) r_{i-1/2}^2 \psi_{i-1/2}^2}{\Delta r (r_{i+1/2}^3 - r_{i-1/2}^3)} - \\ \left[\frac{3}{2} \psi_i^4 (K^r_r)_i^2 + 4\pi \psi_i^4 (D_i + \tau_i + 3P_i) + 4\pi \frac{(S_r)_i^2}{(\tau_i + D_i + P_i)} \right] \alpha_i &= 0, \quad i = 2, \dots, N_r - 1, \\ \alpha_{N_r} - \frac{1 - M_{N_r}/(2r_{N_r})}{1 + M_{N_r}/(2r_{N_r})} &= 0, \end{aligned}$$

where $M_{N_r} = 2(\psi_{N_r} - 1)r_{N_r}$. For the bulk equations we have discretized the expression $(1/r^2) \partial/\partial r$ as $3\partial/\partial(r^3)$. This is a particular instance of a standard technique in numerical relativity (originally due to Evans [28]) whereby terms of the form $df(r)/dr$ with $f(r) \sim r^p$ as $r \rightarrow 0$, and for some integer $p > 1$, are rewritten as $p r^{p-1} (d/d(r^p))f(r)$, and then differenced. This approach generally leads to improved behaviour of numerical solutions near $r = 0$, since the difference scheme is, by construction, consistent with the leading order regularity behaviour of the differentiated function.

Equations (4.40) comprise a linear tridiagonal system for the α_i which can again be solved using a standard LAPACK routine. Note that the discrete outer boundary condition used here derives from (4.36).

Finally, we need to discretize equation (4.13) for the shift vector component β . This is done by first introducing a new variable $w \equiv \beta/r$, with discrete representation w_i . In terms of w , second-order discretization of equation (4.13) results in

$$\begin{aligned} w_1 &= 0, \\ \frac{w_{i+1} - w_i}{\Delta r} - \frac{3}{4} \left[\frac{\alpha_{i+1} (K^r_r)_{i+1}}{r_{i+1}} + \frac{\alpha_i (K^r_r)_i}{r_i} \right] &= 0, \quad i = 1, \dots, N_r - 1. & (4.41) \end{aligned}$$

We solve these equations in two stages, first integrating with an arbitrary boundary (initial) condition to give a set of provisional values, \tilde{w}_i , then correcting the \tilde{w}_i to produce final values w_i that satisfy the true boundary condition. Specifically, we set $\tilde{w}_1 = 0$, and integrate outwards. We then set

$$w_i = \tilde{w}_i + k, \quad (4.42)$$

where k is a constant value chosen so that

$$\frac{w_{N_r} - w_{N_r-1}}{\Delta r} + 2 \frac{w_{N_r} + w_{N_r-1}}{(r_{N_r} + r_{N_r-1})} = 0. \quad (4.43)$$

This outer boundary condition is derived from (4.35) and the definition of w . Finally, we compute the values of the shift component using $\beta_i = w_i r_i$.

4.3.2 Hydrodynamic Equations

Treatment of the fluid equations in the discrete domain requires special care. As we have already discussed, the hydrodynamic equations will quite generically develop discontinuities, even if the initial conditions are smooth. In order to handle such discontinuities numerically we have adopted a finite-volume approach, using Roe's approximation for computation of the numerical fluxes. For discussions of these methods in general see [57], [58], for their application to special relativistic hydro see [67], and for the general relativistic case see [30]. Our approach produces a solver of so-called Godunov type, involving the solution of a Riemann problem at the spatial boundary of each of the discrete volume elements (cells). As we have previously noted (Sec. 1.4), Godunov methods are applicable to any set of hyperbolic evolution equations that has been written in conservation law form. In particular, our fluid equations (4.20)-(4.22) can be written as

$$\frac{1}{\alpha r^2} \frac{\partial}{\partial t} (r^2 \mathbf{q}) + \frac{1}{\alpha r^2} \frac{\partial}{\partial r} (\alpha r^2 \mathbf{F}) = \mathbf{S}. \quad (4.44)$$

Here \mathbf{q} , \mathbf{F} , \mathbf{S} are 3-dimensional *vectors* of dynamical variables, fluxes and sources, respectively:

$$\mathbf{q} = [\tilde{D}, \tilde{S}_r, \tilde{\tau}], \quad (4.45)$$

$$\mathbf{F} = \left[\tilde{D} \left(v^r - \frac{\beta}{\alpha} \right), \tilde{S}_r \left(v^r - \frac{\beta}{\alpha} \right) + \tilde{P}, \tilde{\tau} \left(v^r - \frac{\beta}{\alpha} \right) + \tilde{P} v^r \right], \quad (4.46)$$

$$\mathbf{S} = \left[0, \left\{ 6\tilde{P} + 2 \frac{\tilde{S}_r^2}{(\tilde{\tau} + \tilde{D} + \tilde{P})} \right\} \frac{\psi'}{\psi} + \tilde{S}_r \frac{\beta'}{\alpha} - (\tilde{\tau} + \tilde{P}) \frac{\alpha'}{\alpha} + 2 \frac{\tilde{P}}{r}, \right. \\ \left. - \frac{\tilde{S}_r}{\psi^4} \frac{\alpha'}{\alpha} - 2\tilde{P} \frac{\beta'}{\alpha} + \left\{ 3\tilde{P} + \frac{\tilde{S}_r^2}{(\tilde{\tau} + \tilde{D} + \tilde{P})} \right\} K^r{}_r + 2 \frac{\tilde{P}\beta}{r\alpha} \right]. \quad (4.47)$$

In addition we define a vector of primitive variables

$$\mathbf{p} = [\rho_0, v^r, P] \quad (4.48)$$

which can be used to specify the state of the fluid and that we call primitive variables. These variables, related to \mathbf{q} by (4.4-4.9), are useful in order to compute the fluxes \mathbf{F} .

In our finite-volume approach, we discretize the spacetime region bounded by the hypersurfaces Σ_t and $\Sigma_{t+\Delta t}$ with a set of uniform-size rectangular cells $\{C_{i+1/2}^{n+1/2}\}$ having vertices $\{t^n, t^{n+1}, r_i, r_{i+1}\}$, see Fig. 4.2.

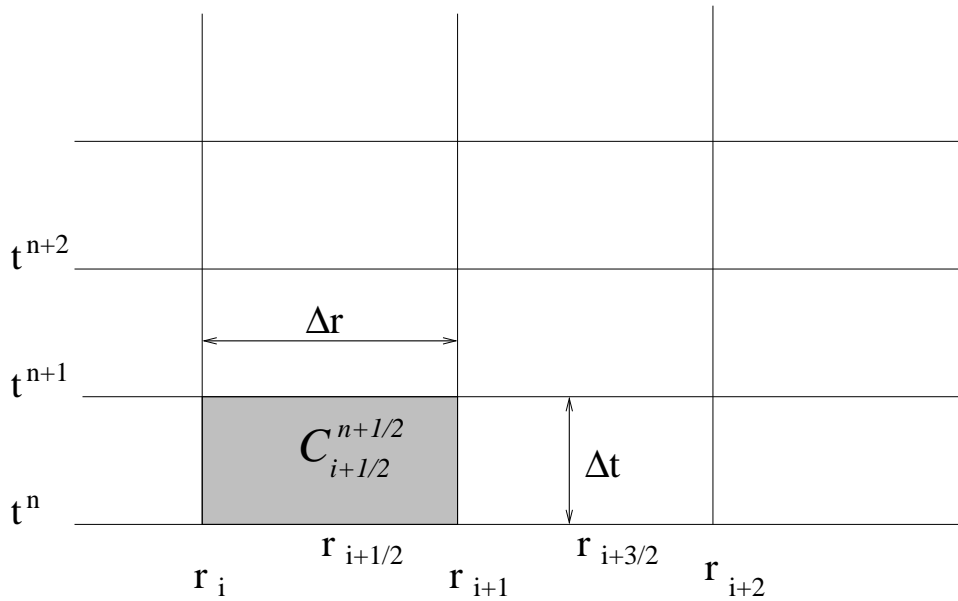


Figure 4.2: Detail of one of the control volumes $C_{i+1/2}^{n+1/2}$ used in order to discretize the hydrodynamic equations of motion. Note that the vertices of the cells correspond to locations (t^n, r_i) , (t^n, r_{i+1}) , (t^{n+1}, r_i) etc., and are the locations at which the discrete geometric variables are defined.

In practice, the cell vertices are the locations at which the geometric variables (which satisfy finite difference equations) are defined.

Integrating these equations over any control volume, $C_{i+1/2}^{n+1/2}$, we get

$$\int_{C_{i+1/2}^{n+1/2}} \frac{\partial}{\partial t} (r^2 \mathbf{q}) dr dt + \int_{C_{i+1/2}^{n+1/2}} \frac{\partial}{\partial r} (\alpha r^2 \mathbf{F}) dr dt = \int_{C_{i+1/2}^{n+1/2}} \mathbf{S} \alpha r^2 dr dt, \quad (4.49)$$

where we have used $dC_{i+1/2}^{n+1/2} = \alpha r^2 dr dt$ for the infinitesimal 2-volume element associated with the cell $C_{i+1/2}^{n+1/2}$. Note that this is not the usual volume element, $\sqrt{-g} = \alpha r^2 \psi^6$, associated with the metric (4.2), because a factor of ψ^6 has been absorbed in the source terms \mathbf{S} through our definition of the new variables \tilde{D} , \tilde{S}^r_r , etc.

Using standard integral theorems this last equation can be expressed as

$$\begin{aligned} & \left(\bar{\mathbf{q}}_{i+1/2}^{n+1} r_{i+1/2}^2 \Delta r - \bar{\mathbf{q}}_{i+1/2}^n r_{i+1/2}^2 \Delta r \right) + \\ & \left(\hat{\mathbf{F}}_{i+1}^{n+1/2} \alpha_{i+1}^{n+1/2} r_{i+1}^2 \Delta t - \hat{\mathbf{F}}_i^{n+1/2} \alpha_i^{n+1/2} r_i^2 \Delta t \right) = \tilde{\mathbf{S}}_{i+1/2}^{n+1/2} \alpha_{i+1/2}^{n+1/2} r_{i+1/2}^2 \Delta t \Delta r, \end{aligned} \quad (4.50)$$

where $\bar{\mathbf{q}}_{i+1/2}^n$, $\hat{\mathbf{F}}_i^{n+1/2}$, and $\tilde{\mathbf{S}}_{i+1/2}^{n+1/2}$ —which are the fundamental discrete hydrodynamical variables—are defined by

$$\bar{\mathbf{q}}_{i+1/2}^n \equiv \frac{1}{r_{i+1/2}^2 \Delta r} \int_{r_i}^{r_{i+1}} \mathbf{q}(t^n, r) r^2 dr, \quad (4.51)$$

$$\hat{\mathbf{F}}_i^{n+1/2} \equiv \frac{1}{\alpha_i^{n+1/2} \Delta t} \int_{t^n}^{t^{n+1}} \mathbf{F}(t, r_i) \alpha dt, \quad (4.52)$$

$$\tilde{\mathbf{S}}_{i+1/2}^{n+1/2} \equiv \frac{1}{\alpha_{i+1/2}^{n+1/2} r_{i+1/2}^2 \Delta t \Delta r} \int_{t^n}^{t^{n+1}} \int_{r_i}^{r_{i+1}} \mathbf{S}(t, r) \alpha r^2 dt dr. \quad (4.53)$$

Eqns. (4.50), along with the above definitions, comprise the basic discretization adopted for eqns. (4.44).

We now schematically write eqns. (4.50) in the following way:

$$\bar{\mathbf{q}}_{i+1/2}^{n+1} = \bar{\mathbf{q}}_{i+1/2}^n + \Delta t G_{i+1/2}^{n+1/2}, \quad (4.54)$$

where

$$G_{i+1/2}^{n+1/2} = \Delta t \left[- \frac{\left(\alpha_{i+1}^{n+1/2} r_{i+1}^2 \hat{\mathbf{F}}_{i+1}^{n+1/2} - \alpha_i^{n+1/2} r_i^2 \hat{\mathbf{F}}_i^{n+1/2} \right)}{r_{i+1/2}^2 \Delta r} + \tilde{\mathbf{S}}_{i+1/2}^{n+1/2} \alpha_{i+1/2}^{n+1/2} \right]. \quad (4.55)$$

Note that $\hat{\mathbf{F}}_i^{n+1/2}$ and $\tilde{\mathbf{S}}_{i+1/2}^{n+1/2}$ depend on the fluid quantities at both the advanced and retarded discrete times, t^{n+1} and t^n , respectively. In order to approximate the fluxes, $\hat{\mathbf{F}}_i^{n+1/2}$, we use Roe's approximation [90], which is given by

$$\hat{\mathbf{F}}_i = \frac{1}{2} \left(\mathbf{F}(\tilde{\mathbf{p}}^R) + \mathbf{F}(\tilde{\mathbf{p}}^L) - \sum |\lambda_\alpha| \omega_\alpha \boldsymbol{\eta}_\alpha \right). \quad (4.56)$$

We will explain in detail below the calculation of the different elements that appear in this last expression. For the time being, we note that λ_n and $\boldsymbol{\eta}_n$ are the eigenvalues and right eigenvectors, respectively, of the velocity matrix $\mathbf{V} = \partial \mathbf{F} / \partial \mathbf{q}$. $\mathbf{F}(\tilde{\mathbf{p}}^R)$, $\mathbf{F}(\tilde{\mathbf{p}}^L)$ are computed from equation (4.46) using approximations $\tilde{\mathbf{p}}^R$ and $\tilde{\mathbf{p}}^L$ for the primitive variables. In fact, $\tilde{\mathbf{p}}^R$ and $\tilde{\mathbf{p}}^L$ are approximations to the primitive variables at the same spatial location—the location of the cell interface, $r = r_i$ —but are computed using values defined either to the right or to the left, respectively, of the interface. The process of computing approximations at the cell interfaces is known as *reconstruction*. In our case we use a “minmod slope limiter” type [106] of reconstruction which results in equations (4.61)

and (4.62) for $\tilde{\mathbf{p}}^L$ and $\tilde{\mathbf{p}}^R$. We note that the calculation of the primitive variables, \mathbf{p} , from the conservative variables, \mathbf{q} , is not completely trivial due to the non-linear algebraic relationship between the two sets of quantities. The specific method that we use to compute $\mathbf{p}(\mathbf{q})$ is also explained below.

Expression (4.56) results in a second order (in space) approximation for the fluxes, that holds in regions of smooth flow, and away from any extrema of the functions being reconstructed. On the other hand, computation of the source term, $\tilde{\mathbf{S}}_{i+1/2}^{n+1/2}$, using the values $\bar{\mathbf{q}}_{i+1/2}^n$ yields only a first order (in time) approximation. To maintain overall second order accuracy in the cell size (again, in regions of smooth flow and away from any maxima in $\bar{\mathbf{q}}$), we decompose the time step into two sub-steps:

$$\bar{\mathbf{q}}_{i+1/2}^{n+1/2} = \bar{\mathbf{q}}_{i+1/2}^n + \frac{\Delta t}{2} G_{i+1/2}^n, \quad (4.57)$$

$$\bar{\mathbf{q}}_{i+1/2}^{n+1} = \bar{\mathbf{q}}_{i+1/2}^n + \Delta t G_{i+1/2}^{n+1/2}. \quad (4.58)$$

$G_{i+1/2}^n$ corresponds to expression (4.55) evaluated using $\hat{\mathbf{F}}_i^n$, $\tilde{\mathbf{S}}_{i+1/2}^n$ and α_i^n , while $G_{i+1/2}^{n+1/2}$ is computed using $\hat{\mathbf{F}}_i^{n+1/2}$, $\tilde{\mathbf{S}}_{i+1/2}^{n+1/2}$ and $\alpha_i^{n+1/2}$ (an interpolation of the lapse function at the half time step). $\hat{\mathbf{F}}_i^{n+1/2}$ and $\tilde{\mathbf{S}}_{i+1/2}^{n+1/2}$ are calculated from the conservative variables obtained from (4.57) and their corresponding primitive variables. This completes the description of the basic update scheme for the fluid variables $\bar{\mathbf{q}}_{i+1/2}^{n+1}$.

We conclude with two additional remarks concerning our numerical scheme. First, we note that the flux for the \tilde{S}_r equation (4.46) is actually split into two distinct pieces, one that contains a term that goes as $2\tilde{P}/r$, and the second that absorbs the remaining terms. The first term is manifestly divergent as $r \rightarrow 0$ and directly cancels with the analogous term appearing in the source of (4.47). Second, we observe that difference quotients such as

$$\frac{(\alpha_{i+1} r_{i+1}^2 F_{i+1} - \alpha_i r_i^2 F_i)}{r_{i+1/2}^2 \Delta r}, \quad (4.59)$$

which appear in $G_{i+1/2}$ (see (4.55)) are rewritten in the following way

$$\frac{3(\alpha_{i+1} r_{i+1}^2 F_{i+1} - \alpha_i r_i^2 F_i)}{r_{i+1}^3 - r_i^3}, \quad (4.60)$$

in the same spirit as for the finite difference case explained in the discussion of (4.40).

Calculation of the Roe flux

We now explain in more detail how to compute the different expressions appearing in formula (4.56). Fig. 4.3 shows the main steps in the calculation of the Roe flux. The reconstructed values $\tilde{\mathbf{p}}^R$ and $\tilde{\mathbf{p}}^L$ —from which the quantities $\mathbf{F}(\tilde{\mathbf{p}}^R)$ and $\mathbf{F}(\tilde{\mathbf{p}}^L)$ that appear in the Roe approximation are

calculated—are computed using

$$\tilde{\mathbf{p}}_{i+1/2}^L = \bar{\mathbf{p}}_i + \boldsymbol{\sigma}_i (r_{i+1/2} - r_i), \quad (4.61)$$

$$\tilde{\mathbf{p}}_{i+1/2}^R = \bar{\mathbf{p}}_{i+1} + \boldsymbol{\sigma}_{i+1} (r_{i+1/2} - r_{i+1}). \quad (4.62)$$

in equation (4.46). Note that $\bar{\mathbf{p}}_i$ are the primitive values defined at the cell centres, their computation from the conservative variables is explained in detail in the next section. In equations (4.61) and (4.62), $\boldsymbol{\sigma}_i$ is given by

$$\boldsymbol{\sigma}_i = \text{minmod}(\mathbf{s}_{i-1/2}, \mathbf{s}_{i+1/2}). \quad (4.63)$$

with

$$\mathbf{s}_{i+1/2} = \frac{\bar{\mathbf{p}}_{i+1} - \bar{\mathbf{p}}_i}{r_{i+1} - r_i}. \quad (4.64)$$

Finally the minmod function is defined by

$$\text{minmod}(a, b) = \begin{cases} 0 & \text{if } ab < 0 \\ a & \text{if } |a| < |b| \text{ and } ab > 0 \\ b & \text{if } |a| > |b| \text{ and } ab > 0. \end{cases} \quad (4.65)$$

Note that this function is used as a “slope-limiter” in order to decrease spurious oscillations that may appear at discontinuities. If the two slopes $\boldsymbol{\sigma}_i$ and $\boldsymbol{\sigma}_{i+1}$ have the same sign, then the one with smaller absolute value is used to linearly reconstruct the fluid variables. On the other hand if the slopes have differing signs (e.g. at an extremum), a first order reconstruction is performed, i.e. the values of the fluid at the cell centre are assigned to the cell interface. At the extrema, this produces a reduction of the accuracy of the overall scheme from second to first order in the mesh spacing Δr . This reconstruction procedure introduces a certain amount of dissipation in the overall scheme [79]. We also note that this is by no means the only viable way of reconstructing; for discussion of other approaches see [58] and [77].

We now explain in detail the characteristic structure of \mathbf{V} , which is needed to compute the Roe approximation for the numerical fluxes. The eigenvalues, λ_α , and right eigenvectors, $\boldsymbol{\eta}_\alpha$, of \mathbf{V} are (see [30])

$$\lambda_0 = \alpha v^r - \beta, \quad (4.66)$$

$$\lambda_\pm = \frac{\alpha}{1 - v^2 c_s^2} \left\{ v^r (1 - c_s^2) \pm c_s \sqrt{(1 - v^2) \left[\frac{1}{\psi^4} (1 - v^2 c_s^2) - v^r v^r (1 - c_s^2) \right]} \right\} - \beta, \quad (4.67)$$

$$\boldsymbol{\eta}_0 = \left(\frac{\mathcal{K}}{hW}, v_r, 1 - \frac{\mathcal{K}}{hW} \right), \quad (4.68)$$

$$\boldsymbol{\eta}_\pm = \left(1, hW C_\pm^r, hW \tilde{\mathcal{A}}_\pm^r - 1 \right), \quad (4.69)$$

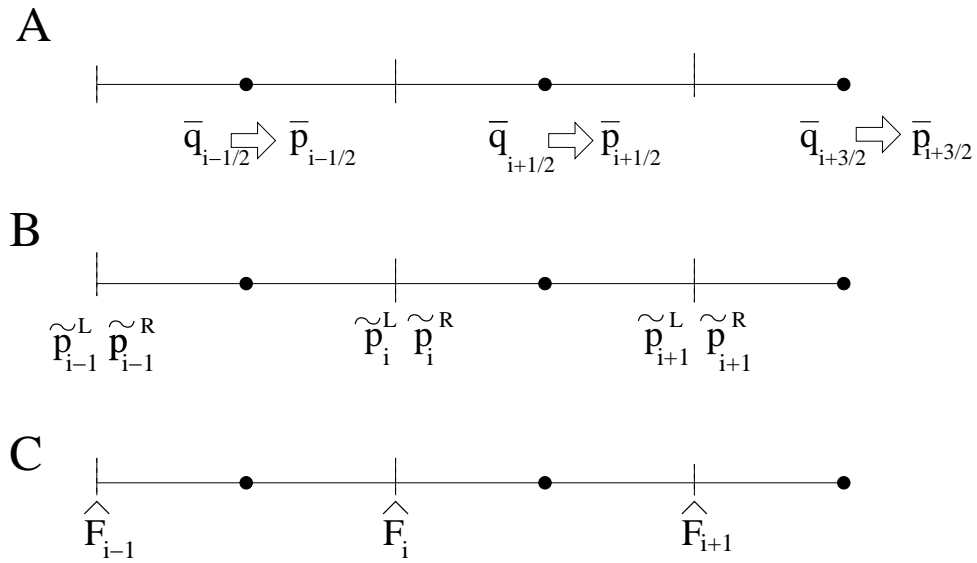


Figure 4.3: This figure illustrates the main stages in the computation of the Roe approximation for the numerical flux \hat{F} . First, in stage A, the primitive variables are computed from the conservative variables at the location of each cell center. In stage B, two approximations for the primitive variables are computed at each cell interface, one from values defined at, or to the left of the interface ($\tilde{\mathbf{p}}^L$, equation (4.61)), and the other using values defined at, or to the right of the interface ($\tilde{\mathbf{p}}^R$, equation (4.62)). Finally, using these last approximations, the characteristic structures of \mathbf{V} , $\mathbf{F}(\tilde{\mathbf{p}}^R)$ and $\mathbf{F}(\tilde{\mathbf{p}}^L)$ are calculated in stage C, enabling the computation of the Roe fluxes, $\hat{\mathbf{F}}$, using (4.56).

where we have defined the following quantities:

$$\mathcal{K} = \frac{\kappa/\rho_0}{\kappa/\rho_0 - c_s^2}, \quad (4.70)$$

$$\mathcal{C}_\pm^r = v_r - \mathcal{V}_\pm^r, \quad (4.71)$$

$$\mathcal{V}_\pm^r = \frac{v^r - \Lambda_\pm^r}{1/\psi^4 - v^r \Lambda_\pm^r}, \quad (4.72)$$

$$\tilde{\mathcal{A}}_\pm^r = \frac{1/\psi^4 - v^r v^r}{1/\psi^4 - v^r \Lambda_\pm^r}, \quad (4.73)$$

$$\Lambda_\pm^r = \lambda_\pm/\alpha + \beta/\alpha. \quad (4.74)$$

In addition, we have introduced the sound speed, c_s , in the above, defined by $c_s^2 = 1/h (\chi + P/\rho_0^2 \kappa)$, with $\chi = \partial P/\partial \rho_0$ and $\kappa = \partial P/\partial \epsilon$. The particular values of the primitive variables used in order to compute these characteristic fields are $1/2 (\mathbf{p}^L + \mathbf{p}^R)$.

The last ingredient we need in order to compute the Roe flux are the ω_α ; these are the jumps in the characteristic variables associated with the local Riemann problem, and are implicitly defined by

$$\tilde{\mathbf{q}}_{i+1/2}^R - \tilde{\mathbf{q}}_{i+1/2}^L = \sum_\alpha \omega_\alpha \boldsymbol{\eta}_\alpha. \quad (4.75)$$

Here $(\tilde{\mathbf{q}}^R, \tilde{\mathbf{q}}^L)$ are the values of the conservative variables, which are calculated from the reconstructed primitive variables $(\tilde{\mathbf{p}}^R, \tilde{\mathbf{p}}^L)$, using (4.61–4.62). We first reconstruct the primitive variables, then transform to conservative variables, since this approach leads to increased numerical stability relative to direct reconstruction of the conservative variables [79].

Calculation of the primitive variables

The final piece of the algorithm for evolution of the discrete fluid quantities involves the calculation of the primitive variables $\mathbf{p} = [\rho_0, v, P]$ from the conservative variables $\mathbf{q} = [\tilde{D}, \tilde{S}_r, \tilde{\tau}]$. From the definition of the conservative variables (4.4)–(4.9), as well as the relation $h = 1 + \epsilon + P/\rho_0$, we can derive the following equation for the pressure

$$f(P) = D(1 + \epsilon)W + P(W^2 - 1) - D - \tau = 0. \quad (4.76)$$

Noting that $W(P) = \sqrt{\mathcal{Z}^2/(\mathcal{Z}^2 - S^2)}$, where $\mathcal{Z} = (\tau + D + P)$, and assuming that the equation of state can be cast in the form $\epsilon = \epsilon(\rho_0, P) = (D/W, P)$, we see that, for given values of D , S_r and τ , (4.76) becomes a non-linear equation for P . Given a good initial guess for P , we can find a solution to (4.76) using a Newton-Raphson method, for which we need to be able to compute the derivative $df(P)/dP \equiv f'(P)$. To this end, the following relations are useful:

$$W'(P) = (1 - W^2) / \sqrt{\mathcal{Z}^2 - S^2}, \quad (4.77)$$

$$\epsilon'(P) = \frac{DW'(P)}{W^2} \frac{\chi}{\kappa} + \frac{1}{\kappa}. \quad (4.78)$$

Furthermore, in order to calculate (4.78) we use

$$\begin{aligned}
\epsilon' &= \left. \frac{\partial \epsilon}{\partial P} \right|_{D, \tau, S_i} = \left. \frac{\partial \epsilon}{\partial \rho_0} \right|_P \left. \frac{\partial \rho_0}{\partial P} \right|_{D, \tau, S_i} + \left. \frac{\partial \epsilon}{\partial P} \right|_{\rho_0} \\
&= -\frac{D}{W^2} \left. \frac{\partial W}{\partial P} \right|_{D, \tau, S_i} \left. \frac{\partial \epsilon}{\partial \rho_0} \right|_P + \left. \frac{\partial \epsilon}{\partial P} \right|_{\rho_0} \\
&= -\frac{D}{W^2} \left. \frac{\partial W}{\partial P} \right|_{D, \tau, S_i} (-1) \left. \frac{\partial P}{\partial \rho_0} \right|_{\epsilon} / \left. \frac{\partial P}{\partial \epsilon} \right|_{\rho_0} + \frac{1}{\kappa} \\
&= \frac{D}{W^2} \left. \frac{\partial W}{\partial P} \right|_{D, \tau, S_i} \frac{\chi}{\kappa} + \frac{1}{\kappa}.
\end{aligned} \tag{4.79}$$

Collecting results, we have

$$f'(P) = D \left[1 + \epsilon \left(\frac{D}{W}, P \right) \right] W' + DW \left[W' \frac{D}{W^2} \frac{\chi}{\kappa} + \frac{1}{\kappa} \right] + W^2 - 1 + 2PWW'. \tag{4.80}$$

For the specific equation of state considered here, $P = (\Gamma - 1) \rho_0 \epsilon$, we have

$$f'(P) = W' \left[D + 2PW \frac{\Gamma}{\Gamma - 1} \right] + W^2 \frac{\Gamma}{\Gamma - 1} - 1. \tag{4.81}$$

The following relations are also needed at various stages of the update algorithm:

$$\epsilon = \frac{PW}{(\Gamma - 1)D}, \tag{4.82}$$

$$\kappa = (\Gamma - 1)\rho_0 = (\Gamma - 1)\frac{D}{W}, \tag{4.83}$$

$$\chi = (\Gamma - 1)\epsilon = \frac{PW}{D}, \tag{4.84}$$

$$c_s^2 = \frac{PW\Gamma(\Gamma - 1)}{D(\Gamma - 1) + PWT} = \left[\frac{D}{PWT} + \frac{1}{\Gamma - 1} \right]^{-1}. \tag{4.85}$$

Once the pressure is calculated the rest of the primitive variables can be computed using:

$$v_r = \frac{S_r}{\tau + D + P}, \tag{4.86}$$

$$v^r = \frac{1}{\psi^4} v_r, \tag{4.87}$$

$$\rho_0 = D\sqrt{1 - v_r v^r}, \tag{4.88}$$

$$\epsilon = \frac{P}{(\Gamma - 1)\rho_0}. \tag{4.89}$$

The calculation v_r using (4.86) can lead to non-physical velocities larger than 1. We note that in order to avoid this problem, an alternative expression to compute v_r , which ensures $v_r < 1$, was proposed in [78].

4.4 Results

4.4.1 New Variables

As explained in Sec. 4.2, the variables, \tilde{D}, \tilde{S}_r and $\tilde{\tau}$ that we have introduced in order to write the hydrodynamic equations in conservative form are not precisely those— D, S_r and τ —which are proposed and used by other authors [66], [30]. Although use of either set allows us to write the fluid equations in conservation law form, we will now argue that the set \tilde{D}, \tilde{S}_r and $\tilde{\tau}$ is a better choice when viewed in the context of providing sources for the geometrical constraint equations.

Let us consider the initial data problem for our self-gravitating fluid. In spherical symmetry the gravitational field has no dynamical degrees of freedom, and as a consequence the initial state of the geometry is totally fixed by the state of the matter sources at $t = 0$.

Specifically (and strictly for simplicity of presentation), if we consider time symmetric initial conditions (so that the resulting spacetime has a $t \rightarrow -t$ symmetry about $t = 0$), then the complexity of the differential equations governing our model is considerably reduced. In particular, the radial 3-velocity, v^r , of the fluid must identically vanish, and this simplifies or eliminates many of the terms in the constraints that involve the fluid variables. Time symmetry also implies that the entire extrinsic curvature tensor vanishes, so the radial momentum constraint is trivially satisfied. The only non-trivial constraint is the Hamiltonian constraint, which written in terms of D and τ (S_r vanishes due to the time symmetry) takes the form

$$\frac{1}{r^2} \partial_r (r^2 \partial_r \psi) + 2\pi (D + \tau) \psi^5 = 0, \quad (4.90)$$

with boundary conditions given by (4.33). Here we note that the operator acting on ψ is simply the radial piece of the Laplacian written in spherical-polar coordinates, taking into account the fact that ψ is spherically symmetric. Given the condition $v^r = 0$, we can view D and τ as freely-specifiable quantities that fix the initial state of the fluid. For the sake of concreteness, we consider an initial profile for D given by a gaussian pulse

$$D(0, r) = A \exp \left[- (r - r_0)^2 / \Delta_r^2 \right], \quad (4.91)$$

and then compute $\tau(0, r)$, from the polytropic equation of state $P = K\rho_0^\Gamma$. This gives us the condition that $P(r) = D(r)^\Gamma$, so that $\tau(r, 0) = P(r)/(\Gamma - 1) = D(r)^\Gamma/(\Gamma - 1)$.

We investigate the behaviour of solutions of (4.90) using the following shooting method. For given values of A , r_0 and Δ_r , and adopting the notation $\psi(r) \equiv \psi(0, r)$, we choose a trial value for $\psi(0)$ (the shooting parameter). Given the second initial condition, $\psi'(0) = 0$ (which follows from regularity, and where a prime now denotes differentiation with respect to r), (4.90) can be integrated radially outwards to some final radius $r = r_{\max}$. The value $\psi(0)$ is then iteratively

refined until the value $\psi(r_{\max})$ satisfies the discrete boundary condition given in (4.38) to some specified tolerance.

For sufficiently small values of the amplitude parameter, A , we encountered no problems in finding solutions of (4.90) using this technique. However, for large values of A the situation was quite different: in such cases, in fact, there seemed to be *no* values of $\psi(0)$ that would produce solutions of (4.90) satisfying the outer boundary condition, $\lim_{r \rightarrow \infty} \psi(r) = 1$. In Fig. 4.4 we show the estimates, $\lim_{r \rightarrow \infty} \psi(r; A)$ for various values of A , and for $\Gamma = 1.8$.

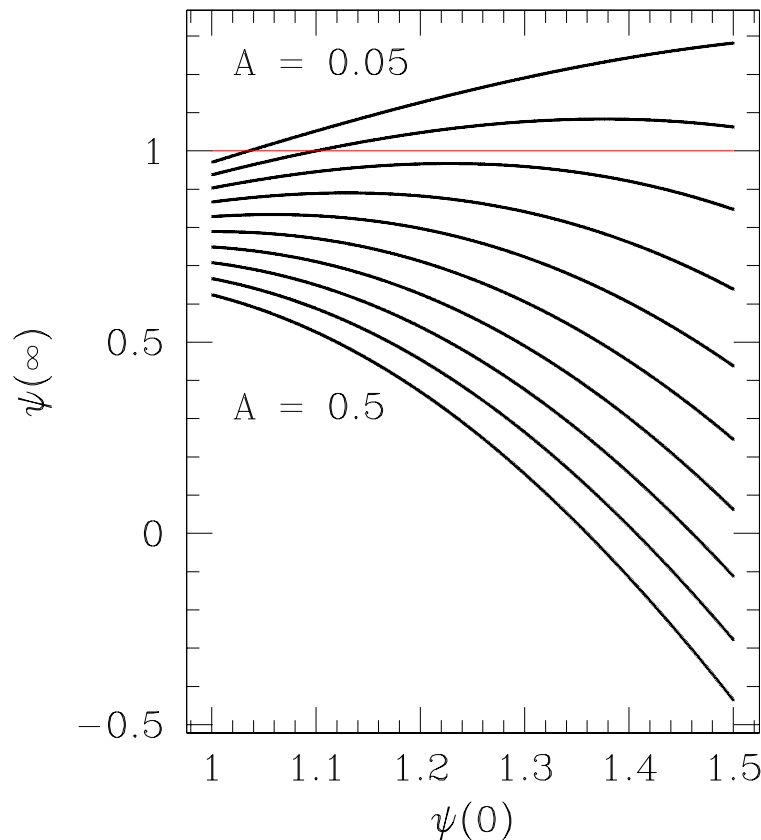


Figure 4.4: This figure plots estimated values of $\psi(\infty)$ as a function of the shooting parameter $\psi(0)$, for 10 different values of the amplitude A in the range $0.05 \leq A \leq 0.5$ and spaced by $\Delta A = 0.05$. All calculations have been done with $r_0 = 0.5$, $\Delta_r = 0.1$ (see (4.91)), $r_{\max} = 1$ and $\Gamma = 1.8$. $\psi(\infty)$ is estimated from the assumption that $\lim_{r \rightarrow \infty} \psi(r) = \psi(\infty) + C/r$. These results clearly suggest that above a certain threshold amplitude (which in this case is approximately $A \sim 0.13$), there are *no* solutions of (4.90) that satisfy the outer boundary condition, $\lim_{r \rightarrow \infty} \psi(r) = 1$.

We note that the solutions plotted in Fig. 4.4 do not correspond to particularly large values of

the conformal factor $\psi(r)$, and that all solutions computed are smooth. We also note that the use of continuation (or homotopic) processes, which use information about the solution for a parameter value A as input (or initialization) for the solution for parameter value $A + \delta A > A$, did not help matters. In addition, we verified that the failure to find solutions of (4.90) was not a consequence of the discretization schemes used. In particular, we used several different solution methods and several distinct discretizations and found the same results in all cases.

The results of the above experiment agree with an observation made by York [115], who analyzed an equation similar to (4.90). York argues that in order for the full non-linear equation to have a solution, the linearization of the equation with respect to $\psi + \delta\psi$,

$$\left[\frac{1}{r^2} \partial_r (r^2 \partial_r) + 10\pi (D + \tau) \psi^4 \right] \delta\psi = -2\pi\psi^5 (\delta D + \delta\tau), \quad (4.92)$$

must also have a solution. The claim is that, in general, the linearized equation will *not* have a solution satisfying $\delta\psi \rightarrow 0$ as $r \rightarrow \infty$. The reasoning that York follows involves analysis of the homogeneous equation (i.e the linear equation without sources) which he shows does not satisfy a maximum principle (as one generally wants for elliptic equations), but instead admits solutions that tend to be oscillatory as $r \rightarrow \infty$. York therefore concludes that the full equation will generally have no solution satisfying the boundary conditions at infinity, when the analogue of $D + \tau$ is freely specified.

The argument that the homogeneous equation does not have solutions that asymptotically tend to zero (applied to our Hamiltonian constraint) is based on the fact that $(D + \tau) \psi^4$ is positive-definite. The sign of this term can be changed by a suitable conformal rescaling of τ and D , i.e. by choosing to freely specify conformally related functions \tilde{D} and $\tilde{\tau}$ defined by $\tilde{D} = D\psi^n$ and $\tilde{\tau} = \tau\psi^n$ for some integer $n > 1$. In terms of these new variables the linearization of the Hamiltonian constraint is

$$\left[\frac{1}{r^2} \partial_r (r^2 \partial_r) + 2\pi (5 - n) (\tilde{D} + \tilde{\tau}) \psi^{4-n} \right] \delta\psi = -2\pi\psi^{5-n} (\delta\tilde{D} + \delta\tilde{\tau}). \quad (4.93)$$

By York's argument, if the second term on the left hand side of the above equation is *negative*-definite, then the theory of elliptic equations tells us that the solution of the equation exists and is unique. The choice $n = 6$ in our definitions of \tilde{D} and $\tilde{\tau}$ thus not only allows us to demonstrate linear stability of the Hamiltonian constraint, it also absorbs the factor ψ^6 that originates from the determinant of the 4-metric, and which appears in the fluid equations of motion. (Here we note that a factor of ψ^6 was also introduced in the definitions of \tilde{S}_r and \tilde{P} in order to simplify the equations of motion).

4.4.2 Evolution of TOV solution

The Tolman-Oppenheimer-Volkoff (TOV) solutions [80], [102], and [103] are the static solutions of the spherically symmetric equations of general relativistic hydrodynamics. These solutions were initially studied by Tolman [102] and [103] and then generalized by Oppenheimer and Volkoff [80] in order to describe neutron stars (stars supported against gravitational collapse by the degeneracy of neutrons). To construct these solutions we adopt a polytropic equation of state

$$P = K\rho_0^\Gamma, \quad (4.94)$$

which can be considered as an equation for non-interacting degenerate matter [94]. This equation can be seen as a particular case of the ideal gas equation $P = (\Gamma - 1)\rho_0\epsilon$ in the limit of zero temperature [79].

Let us remind the reader that one of the main uses of the spherically symmetric code explained in this chapter is as a calibrator of our axisymmetric implementation. Ultimately we want to use the axisymmetric code to study the critical collapse of rotating stars. The corresponding spherically symmetric problem is the critical collapse of perturbed TOV solutions, and was studied by Noble [79]. Since the lifetimes of near critical solutions can grow without bound as the critical limit is approached, it is thus crucial that we are able to evolve TOV solutions for long physical times.

It is particularly convenient to compute TOV solutions in Schwarzschild-like coordinates (\tilde{t}, \tilde{r}) , where the time-independent, spherically-symmetric metric takes the form

$$ds^2 = -\exp(2\phi(\tilde{r})) d\tilde{t}^2 + \left(1 - \frac{2m(\tilde{r})}{\tilde{r}}\right)^{-1} d\tilde{r}^2 + \tilde{r}^2 d\Omega^2. \quad (4.95)$$

Using the polytropic equation of state (4.94), the resulting equations for the metric coefficients and pressure are

$$\frac{dm}{d\tilde{r}} = 4\pi\tilde{r}^2\rho, \quad (4.96)$$

$$\frac{d\phi}{d\tilde{r}} = -\frac{1}{\rho + P} \frac{dP}{d\tilde{r}}, \quad (4.97)$$

$$\frac{dP}{d\tilde{r}} = -\frac{(\rho + P)(m + 4\pi\tilde{r}^3 P)}{\tilde{r}(\tilde{r} - 2m)}. \quad (4.98)$$

The equations give rise to a continuous family of solutions which can be parametrized by the central pressure $P(0)$. Choosing a particular value for $P(0)$, and with the additional initial conditions $m(0) = 0$ (regularity) and $\phi(0) = 0$ (normalization of time parameter to central proper time), the set of ODEs (4.96) is integrated outwards from $\tilde{r} = 0$ using the LSODA integration package [84]. After the metric coefficients $m(\tilde{r})$, $\phi(\tilde{r})$ and the pressure $P(\tilde{r})$ have been computed

in the Schwarzschild-like coordinates, we must perform a coordinate transformation to the maximal/isotropic coordinates, (t, r) , used in our evolution code.

Since the TOV solutions are static, we have $t(\tilde{t}, \tilde{r}) = \tilde{t}$ and $r(\tilde{t}, \tilde{r}) = r(\tilde{r})$. We can determine $r(\tilde{r})$ by integrating

$$\frac{dr}{d\tilde{r}} = \left(1 - \frac{2m(\tilde{r})}{\tilde{r}}\right)^{-1/2} \frac{r}{\tilde{r}}. \quad (4.99)$$

This equation can be obtained by first comparing the angular parts of the two metrics, which yields the relationship $\psi^4(r)r^2 = \tilde{r}^2$, then comparing the radial parts,

$$\left(1 - \frac{2m(\tilde{r})}{\tilde{r}}\right)^{-1/2} d\tilde{r} = \psi^2(r)dr, \quad (4.100)$$

and combining the two results.

We now discuss the integration of (4.99). Considering the limit $\tilde{r} \rightarrow 0$ of the equation, and taking into account that $m(\tilde{r}) \sim O(\tilde{r}^3)$ by regularity, we obtain the following equation valid for $\tilde{r} \rightarrow 0$:

$$\frac{dr}{d\tilde{r}} = \frac{r}{\tilde{r}}. \quad (4.101)$$

Therefore the behaviour of r for small values of \tilde{r} is given by $r = A\tilde{r}$, with A a constant that will be fixed by demanding that the solution tend to the Schwarzschild form as $r \rightarrow \infty$. We thus first integrate the following outwards from $r = 0$:

$$\frac{d\tilde{r}}{dr} = 1, \quad \text{if } r = 0, \quad (4.102)$$

$$\frac{dr}{d\tilde{r}} = \left(1 - \frac{2m(\tilde{r})}{\tilde{r}}\right)^{-1/2} \frac{r}{\tilde{r}}, \quad \text{otherwise,} \quad (4.103)$$

which amounts to choosing $A = 1$. Once this integration is complete, we rescale the solution, $r(\tilde{r})$, so that it satisfies the correct asymptotic boundary condition by exploiting the fact that if $r(\tilde{r})$ is a solution to (4.99), then $kr(\tilde{r})$ (with k constant) is also a solution. In particular, we set

$$r(\tilde{r}_{\max}) = \frac{\tilde{r}_{\max}}{2} \left(1 - \frac{m(\tilde{r}_{\max})}{\tilde{r}_{\max}} + \sqrt{1 - \frac{2m(\tilde{r}_{\max})}{\tilde{r}_{\max}}}\right). \quad (4.104)$$

This condition is computed by comparing the metric coefficients of Schwarzschild in the two coordinate systems considered, i.e. by comparing

$$ds^2 = -\left(1 - \frac{2M_s}{r}\right) dt^2 + \left(1 - \frac{2M_s}{r}\right)^{-1} dr^2 + r^2 d\Omega^2, \quad (4.105)$$

$$\text{and } ds^2 = -\left(1 - \frac{2M_s}{\tilde{r}}\right)^2 \left(1 + \frac{M_s}{2\tilde{r}}\right)^{-2} dt^2 + \left(1 + \frac{M_s}{2\tilde{r}}\right)^4 (d\tilde{r}^2 + \tilde{r}^2 d\Omega^2), \quad (4.106)$$

where M_s is the ADM mass of the star.

Finally, we note that once $r = r(\tilde{r})$ is found, $\psi(r)$ is calculated using

$$\psi(r) = \sqrt{\frac{\tilde{r}}{r}}. \quad (4.107)$$

As mentioned above, the different TOV solutions can be parametrized by the value of the pressure at the centre of the star or, equivalently, by the central density. Fig. 4.5 shows plots of solution curves for TOV initial conditions. Specifically, the left plot shows the ADM masses of the stars obtained for $\Gamma = 5/3$ (which corresponds to a non-relativistic degenerate fermi gas) and $K = 1$ as a function of the base-10 logarithm of the stellar radius (we note that the radius of the star, \tilde{r}_* , has been defined somewhat arbitrarily by $P(\tilde{r}_*) < 10^{-10}$). The right plot shows the ADM mass as a function of the base-10 logarithm of the central density. Such plots have been calculated by many authors [44], [79]. Our equilibrium curves qualitatively agree with the ones calculated by [79], and we note that direct comparison is not possible since we are using a different coordinate system.

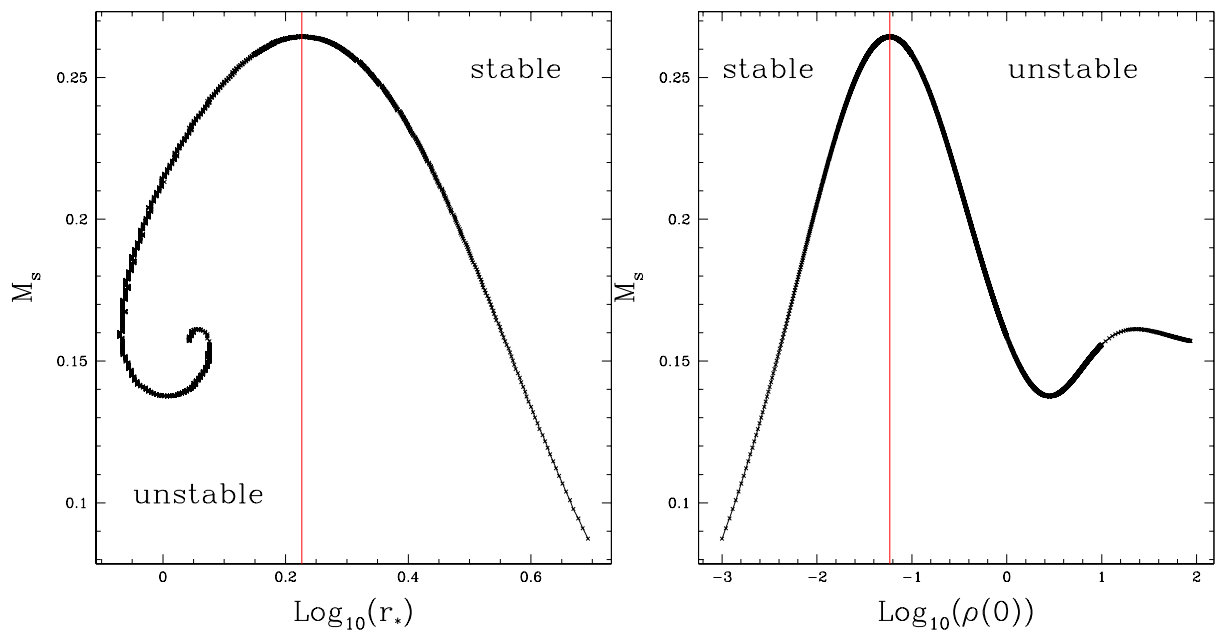


Figure 4.5: These plots show solution curves for TOV initial conditions, computed with $\Gamma = 5/3$ and $K = 1$. The figure on the left plots the ADM mass of each star against the base-10 logarithm of its radius, \tilde{r}_* . The plot on the right shows the ADM mass of the stars as a function of the base-10 logarithm of the central density. In each case, the vertical line indicates a transition between stable and unstable stars.

We now proceed to a discussion of typical results computed using our *dynamical* spherically symmetric hydro code, using TOV configurations as initial data. First, in order to demonstrate

convergence of our code, Fig. 4.6 shows the time evolution of the rescaled central pressure, $\tilde{P}(t, 0)$, from calculations at three different mesh spacings (resolutions). The initial condition for each of the three runs is a TOV solution with a central pressure $P(0) = 0.002157$, and calculated using a polytropic equation of state with $K = 0.1$ and $\Gamma = 5/3$. In order to perform the evolution we choose an integration domain with outer radius at $r_{\max} = 5$ (approximately 8 times larger than the radius of the star) which we discretize with $N_r = 1025, 2049, 4097$ points. Note that we use $\Delta t = \lambda \Delta r$, with $\lambda = 0.2$ held fixed as the spatial resolution is varied, so that each run is characterized by a *single* discretization scale, Δr . This figure provides evidence that the evolution is second order accurate since the least-squares slope, $m \sim dP(t, 0)/dt$, which should be zero in the continuum limit, is apparently $O(\Delta r^2)$.

Although the code is convergent, it is also quite dissipative (a result of the particular Godunov scheme that we are using), which leads to dispersal of the stars after some time (see Fig. 4.6). This effect seems to be more acute in the current maximal/isotropic coordinates than in the polar/areal coordinate system used, for example, in [79]. In order to decrease the amount of dissipation introduced by the update algorithm, we replace the original equation for the numerical flux (4.56) by

$$\hat{F}_i = \frac{1}{2} (\mathbf{F}(\mathbf{p}^R) + \mathbf{F}(\mathbf{p}^L)) - \frac{\epsilon}{2} \sum |\lambda_\alpha| \omega_\alpha \boldsymbol{\eta}_\alpha, \quad (4.108)$$

where ϵ is a tunable parameter. Fig. 4.7 shows the evolution of $\tilde{P}(t, 0)$ for different values of ϵ . Note that for $\epsilon = 1$ we recover the usual Roe approximation for the numerical flux, whereas for $\epsilon = 0$ the discretization corresponds to a particular finite-difference approximation of the hydrodynamic equations. From the figure we can see that a decrease in ϵ leads to a decrease in the slope of $d\tilde{P}(t, 0)/dt$, but that it also makes the solution increasingly irregular. It is thus evident that at least some amount of the significant dissipativity exhibited by the code can be attributed to our particular computation of the numerical flux.

In this chapter we have described a spherical symmetric code to solve the fully coupled equations of general relativistic hydrodynamics. This implementation has not only served as a preliminary step in the construction of the axisymmetric code described in the following chapter, it has allowed us to identify a new set of dynamical variables $\{\tilde{D}, \tilde{S}_r, \tilde{\tau}\}$ with which to describe the fluid. These variables give rise to a well-posed elliptic problem for the constraint equations in the particular coordinate system considered. Moreover, we have also learned that our numerical method is so dissipative that we have difficulty achieving long-term evolution of static, stable, TOV solutions. In order to solve this latter problem, a new numerical implementation that uses adaptive mesh refinement—so that increased grid resolution can be automatically increased where needed—is being developed. This too will be briefly discussed in the next chapter.

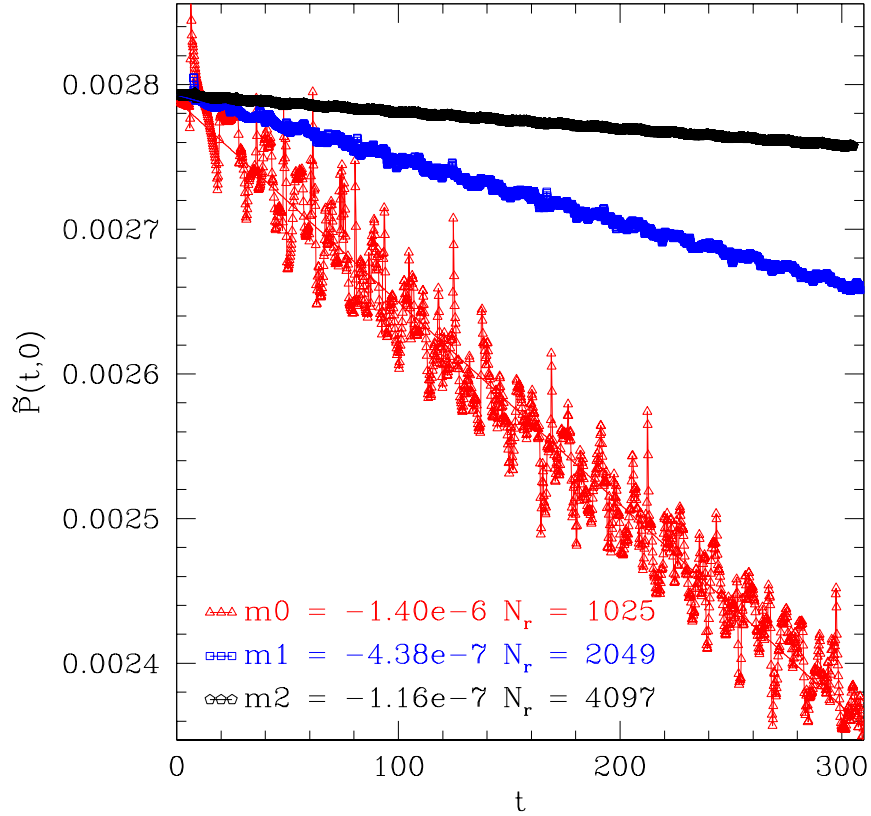


Figure 4.6: This plot shows the evolution of the central value of the rescaled pressure, $\tilde{P}(t, 0)$, using fixed initial data, and three separate finite-difference resolutions: $N_r = 1025$, 2049 and 4097 , with $\lambda = \Delta t / \Delta r = 0.2$. The initial data are computed with a polytropic equation of state ($K = 0.1$ and $\Gamma = 5/3$) and a central pressure $P(0) = 0.002157$. The outer boundary of the computational domain for these calculations is $r_{\max} = 5$, which is approximately 8 times larger than the radius of the star. We see clear evidence for convergence in the sense that the temporal variation in $\tilde{P}(t, 0)$ decreases as the mesh spacing decreases. More quantitatively, the slopes m_0 , m_1 , m_2 (indicated in the figure legend) are tending to zero quadratically in the mesh spacing, as expected for a second order accurate code.

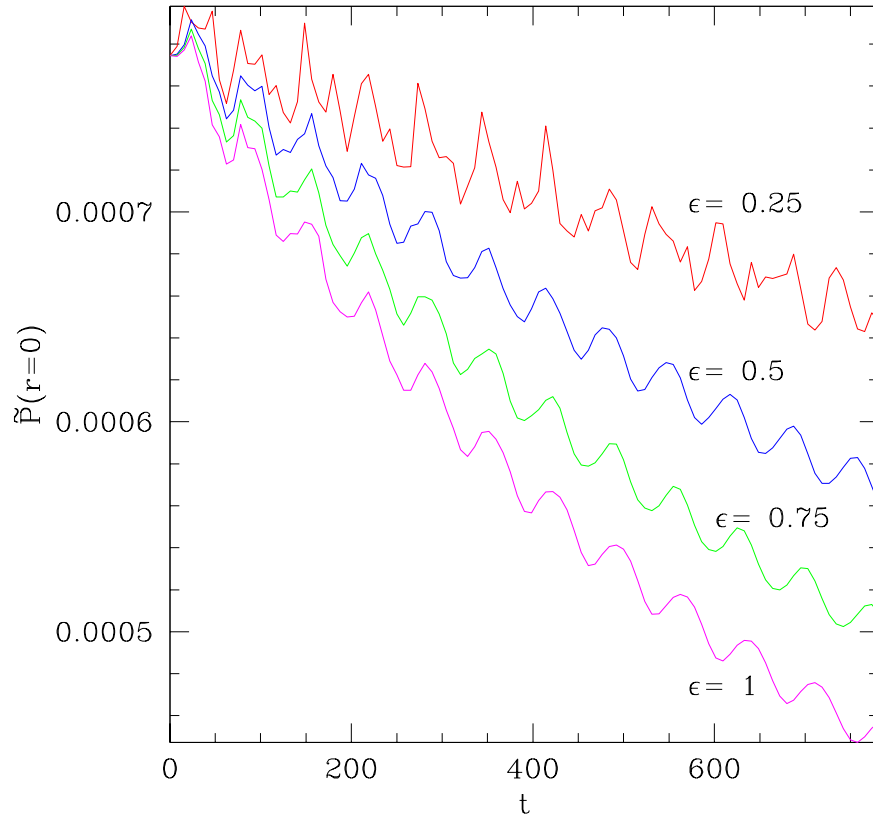


Figure 4.7: This figure shows the evolution of the central value of the conformally rescaled pressure, $\tilde{P}(t, 0)$, for a sequence of evolutions starting from the same TOV initial data ($P(0) = 0.00046$, $\Gamma = 5/3$ and $K = 1$), but using varying amounts of numerical flux (see (4.108)). It is clear that addition of the numerical flux tends to make the code more dissipative (and hence more stable), and that this in turn can have a significant influence on the long-time evolution of the stars. It is also apparent that the numerical solution becomes increasingly irregular as the numerical flux tends to zero (again, consistent with the stabilizing property of the numerical flux).

Chapter 5

Axisymmetric Hydrodynamics

5.1 Introduction

In this chapter we discuss a numerical code that evolves the hydrodynamic equations coupled to the Einstein field equations in axisymmetry. This work makes use of a previously developed code due to Choptuik, Hirschmann, Liebling and Pretorius [19] which solves the Einstein equations in axisymmetry with an optional scalar field matter source. The code described in [19] implements both fully- or partially-constrained evolution (i.e. at least some of the constraint equations are resolved at each time step to fix certain geometric quantities), and has been used to investigate the critical collapse of a massless scalar field in axisymmetry [20].

The work described here involved the following modifications to the existing code: (1) a perfect fluid was incorporated as a source for the geometric evolution and constraint equations, and (2) a routine to integrate the hydrodynamic equations, using an extension of the numerical method described in the previous chapter was included.

This chapter is organized as follows. In Sec. 5.2, a brief introduction to the 2+1+1 formalism is given; this includes a summary of the equations that are to be integrated. Our particular implementation is restricted to the case without rotation around the axis of symmetry. Nevertheless, because one of our long-term goals is the study of rotating configurations, we present, in Sec. 5.3, the equilibrium equations for determining initial data describing a rotating star. This system of equations has an integrability condition that we explain in some detail, following the treatment of Bonazzola et al. [8], but recasting their development in the framework of the 2+1+1 approach. Some explanation concerning the numerics is provided in Sec. 5.4. Finally, results, as well as future plans, are summarized in Sec. 5.5.

5.2 2+1+1 Formalism

We begin with a brief summary of the 2+1+1 approach, and follow with a discussion of the equations of motion that result from the application of this approach in the context of perfect-fluid-containing spacetimes. The 2+1+1 formalism, originally introduced by R. Geroch [34], exploits

the fact that, by definition, there is a (spatial) axial Killing vector field in any axisymmetric spacetime. We remind the reader that the standard approach to numerical relativity involves the 3+1 decomposition summarized in Sec. 1.1, and used in previous chapters. The 3+1 approach involves slicing the spacetime into constant- t spacelike hypersurfaces, and describes the 4-geometry in terms of the 3-geometry intrinsic to each hypersurface, as well as how each slice is embedded in the full spacetime. In the 2+1+1 approach, on the other hand, the spacetime is first decomposed on hypersurfaces orthogonal to the axial Killing vector field, ξ^α . In the remaining quotient spacetime, which has 2 spatial dimensions, as well as 1 temporal dimension, a space-plus-time (i.e. 2+1) decomposition is then performed, in complete analogy to the usual 3+1 split. From the 2+1 perspective, the net effects of the initial decomposition with respect to the “symmetry dimension” are the appearance of additional fields (relative to what one would have for regular 2+1 relativistic gravity), and the appearance of additional source terms in the equations of motion. These fields and source terms are analogous to those that arise in a Kaluza-Klein decomposition (see [83] for a review of this type of decomposition).

We now define ϕ to be the coordinate associated with the axial symmetry, and denote the Killing vector field by $\xi^\alpha = (\partial/\partial\phi)^\alpha$. Paralleling the development in Sec. 1.1, where we defined the 3-dimensional *spatial* metric (1.7) induced on the spacelike hypersurfaces Σ_t , we now define the 3-dimensional *space-time* metric, $\gamma_{\alpha\beta}$,

$$\gamma_{\alpha\beta} = g_{\alpha\beta} - \frac{1}{s^2} \xi_\alpha \xi_\beta, \quad (5.1)$$

induced on *the* 3-dimensional hypersurface orthogonal to ξ^α , where $s = \xi_\alpha \xi^\alpha$ is the norm of the Killing field (by symmetry, we need consider only a *single* 3-dimensional hypersurface in this case). We note that the relative minus sign between the two terms in the definition (5.1) is due to the fact that ξ^α is spacelike. The mixed form of $\gamma_{\alpha\beta}$ is the operator that projects onto the hypersurface:

$$\gamma^\alpha{}_\beta = \delta^\alpha{}_\beta - \frac{1}{s^2} \xi^\alpha \xi_\beta, \quad (5.2)$$

(We again remind the reader of our index conventions: 4-dimensional spacetime tensor indices are denoted by greek letters, 3-dimensional ones are denoted by lower case latin characters, and finally 2-dimensional spatial ones are denoted with upper case latin letters.) We reemphasize that in this case the metric on the three dimensional hypersurface is Lorentzian, not Riemannian, as is the case for the standard 3 + 1 decomposition. Therefore the three dimensional indexes i, j, \dots now take on both spatial and temporal values.

The covariant derivative compatible with $\gamma_{\alpha\beta}$ (γ_{ab}) is denoted by D_a , and can be defined via projection of the 4-dimensional spacetime covariant derivative in the usual manner. Following [20]

the 2+1+1 Einstein equations can be written as:

$$D^a D_a s = -\frac{\omega_a \omega^a}{2s^3} - \frac{8\pi}{s} \left(T_{\phi\phi} - \frac{1}{2} T_{\alpha}^{\alpha} \right), \quad (5.3)$$

$$D_{[a} \omega_{b]} = 8\pi s \epsilon_{ab}{}^c T_{c\phi}, \quad (5.4)$$

$${}^{(3)}R_{ab} = \frac{1}{s} D_a D_b s + \frac{1}{2} s^2 Z_{ac} Z_b{}^c + 8\pi \left(T_{\alpha\beta} \gamma^{\alpha}{}^a \gamma^{\beta}{}^b - \frac{1}{2} \gamma_{ab} T_{\alpha}^{\alpha} \right), \quad (5.5)$$

where we have introduced the twist vector, ω_{α}

$$\omega_{\alpha} = \frac{s^2}{2} \epsilon_{\alpha\beta\lambda\sigma} \xi^{\beta} Z^{\lambda\sigma}, \quad (5.6)$$

and the antisymmetric tensor, $Z_{\alpha\beta}$

$$Z_{\alpha\beta} = \partial_{\alpha} \left(\frac{1}{s^2} \xi_{\beta} \right) - \partial_{\beta} \left(\frac{1}{s^2} \xi_{\alpha} \right). \quad (5.7)$$

As can be easily verified from the definition (5.6), ω_a/s^3 is divergence free:

$$D^a \left(\frac{\omega_a}{s^3} \right) = 0. \quad (5.8)$$

Let us point out at this point that if $s \equiv 1$, in analogy with Kaluza's original work in reducing 4+1 dimensions to 3+1, ξ_a plays the role of a Maxwell field, and then Z_{ab} is simply an electromagnetic field strength tensor.

Equation (5.3) can be viewed as an evolution equation for the scalar quantity s . Additionally, two of the three equations (5.4) provide evolution equations for ω_{ρ} and ω_z while the third is a constraint on those components of the twist vector. Finally, the remaining 3-dimensional field equations (5.5) are to be further decomposed using a space-plus-time split. Performing this split, we can then write the spacetime metric as

$$\begin{aligned} ds^2 = & \left(-\alpha^2 + \frac{1}{s^2} \xi_t^2 + H_{IJ} \beta^I \beta^J \right) dt^2 + 2\xi_t dt d\phi + s^2 d\phi^2 + 2 \left(H_{IJ} \beta^I + \frac{1}{s^2} \xi_t \xi_J \right) dt dx^J \\ & + 2\xi_I dx^I d\phi + \left(H_{IJ} + \frac{1}{s^2} \xi_I \xi_J \right) dx^I dx^J, \end{aligned} \quad (5.9)$$

where H_{AB} is the 2-dimensional spatial metric, α is the lapse function, and β^A is the 2-dimensional shift vector. In order to describe the perfect fluid, and in analogy with the spherically symmetric

case discussed in Chap. 4, we define the following variables:

$$D = \rho_0 W, \quad (5.10)$$

$$S_A = \rho_0 h W^2 v_A, \quad (5.11)$$

$$S_\phi = \rho_0 h W^2 v_\phi, \quad (5.12)$$

$$E = \rho_0 h W^2 - P, \quad (5.13)$$

$$\tau = E - D, \quad (5.14)$$

$$v^A = \frac{u^A}{\alpha u^0} + \frac{\beta^A}{\alpha}, \quad (5.15)$$

$$v_\phi = \frac{u_\phi}{\alpha u^0}, \quad v^\phi = \frac{1}{s^2} \frac{u_\phi}{\alpha u^0}, \quad (5.16)$$

$$W = \alpha u^0 = (1 - v^A v_A - v^\phi v_\phi)^{-1/2}. \quad (5.17)$$

In terms of these quantities the hydrodynamic equations take the form of conservation laws (see section 5.2.2). Note the non-standard, and original to our work, definitions of v_ϕ and v^ϕ , which are made in order to get equations adapted to the 2+1+1 formalism. We now have all of the necessary elements needed to discuss the equations of motion for the geometric and hydrodynamic variables.

5.2.1 Geometry

We fix our spatial coordinates by demanding that the 2-metric H_{AB} be conformally flat, so that

$$H_{IJ} = \psi^4(t, \rho, z) f_{IJ}, \quad (5.18)$$

where $f_{IJ} = \text{diag}[1, 1]$ is the Euclidean metric in cylindrical coordinates (ρ, z) . The time coordinate is fixed by requiring that the trace of the *three* dimensional extrinsic curvature, ${}^{(3)}K^a_a$, be zero, and where we note that

$${}^{(3)}K = {}^{(3)}K^i_i = -n^i \partial_i (\ln s) + {}^{(2)}K^I_I. \quad (5.19)$$

Here, n^i are the components of a unit vector field orthogonal to the constant- t spacelike hypersurfaces. Equations (5.18-5.19), along with appropriate boundary conditions completely determine α and β^I and thus exhaust the 2+1+1 coordinate freedom.

In order to improve near-axis ($\rho \rightarrow 0$) regularity of our numerical solutions, we introduce a (roughly) dynamically conjugate pair of variables, $\bar{\sigma}$ and $\bar{\Omega}$, defined as follows:

$$\rho \bar{\sigma} = \log \left(\frac{s}{\rho \psi^2} \right), \quad (5.20)$$

$$\rho \bar{\Omega} = -2K_\rho^\rho - K_z^z. \quad (5.21)$$

These are evolved in lieu of s and its dynamical conjugate. In addition, we make the following definitions:

$$\sigma \equiv \rho \bar{\sigma}, \quad (5.22)$$

$$\tilde{\omega}^t \equiv \omega^t \sqrt{\gamma} / \rho^3, \quad (5.23)$$

$$\tilde{\omega}_\rho \equiv \omega_\rho / \rho^2, \quad (5.24)$$

$$\tilde{\omega}_z \equiv \omega_z / \rho^3, \quad (5.25)$$

$$\tilde{D} \equiv \psi^6 D, \quad (5.26)$$

$$\tilde{S}_I \equiv \psi^6 S_I, \quad (5.27)$$

$$\tilde{S}_\phi \equiv \psi^6 S_\phi, \quad (5.28)$$

$$\tilde{\tau} \equiv \psi^6 \tau, \quad (5.29)$$

$$\tilde{P} \equiv \psi^6 P. \quad (5.30)$$

In the equations presented below, we generally use the variable σ in order to minimize the complexity of expressions; the actual variable used in our numerical scheme, however, is $\bar{\sigma}$.

The variables $\tilde{\omega}^t$, $\tilde{\omega}_\rho$ and $\tilde{\omega}_z$ were originally introduced in the study [21] of a complex scalar field, $\Psi(t, \rho, z, \phi)$, endowed with angular momentum via an ansatz

$$\Psi(t, \rho, z, \phi) = \Phi(t, \rho, z) e^{im\phi}, \quad (5.31)$$

for the specific case $m = 1$, i.e. with

$$\Psi(t, \rho, z, \phi) = \Phi(t, \rho, z) e^{i\phi}. \quad (5.32)$$

The specific powers of ρ chosen in the definitions (5.23-5.25) facilitate the construction of finite difference schemes whose solutions have good regularity properties. In particular, for the case of ansatz (5.32), it can be shown that the leading order behavior of the twist components is

$$\lim_{\rho \rightarrow 0} \omega^t = \rho^3 f(t, z) + O(\rho^5), \quad (5.33)$$

$$\lim_{\rho \rightarrow 0} \omega_\rho = \rho^3 g(t, z) + O(\rho^4), \quad (5.34)$$

$$\lim_{\rho \rightarrow 0} \omega_z = \rho^4 h(t, z) + O(\rho^5). \quad (5.35)$$

These expansions then imply that $\tilde{\omega}^t$, $\tilde{\omega}_\rho$ and $\tilde{\omega}_z$ are all $O(\rho)$ as $\rho \rightarrow 0$ —this behavior is more readily maintained in the finite difference domain than $O(\rho^2)$, $O(\rho^3)$ etc.

An important point is that these regularity conditions—again, derived for the case of coupling to a scalar field with the ansatz (5.32)—are more stringent than the most general condition in the

fluid case. Forcing the twist vector to have the above leading order behavior forces the angular momentum to go to zero quadratically, i.e.:

$$\lim_{\rho \rightarrow 0} \tilde{S}_\phi = \rho^2 q(t, z) + O(\rho^4), \quad (5.36)$$

whereas in the general case we would have $\tilde{S}_\phi = p(t, z) + O(\rho^2)$. This restrictive condition is chosen so that we can use equations which are as similar as possible to those described in [19], thereby minimizing the number of required modifications of the code.

We also note that in (5.23) a factor of $\sqrt{\gamma}$, where γ is the determinant of the 3-metric, has been factored out so that time derivatives of the lapse do not appear in the equations of motion. Finally, expressions (5.26-5.30) define conformally rescaled conservative variables, paralleling the definitions made in the spherically symmetric case (see Sec. 4.4.1).

We can now summarize the equations for the geometry. We have two equations which are derived from the momentum constraints, and which govern the shift vector components, β^ρ and β^z :

$$\begin{aligned} & \frac{2}{3}\beta_{,\rho\rho}^\rho + \beta_{,zz}^\rho + \frac{1}{3}\beta_{,\rho z}^z + \frac{1}{\alpha} \left[\frac{2}{3} (\beta_{,z}^z - \beta_{,\rho}^\rho) \alpha_{,\rho} - (\beta_{,\rho}^z + \beta_{,z}^\rho) \alpha_{,z} \right] + \sigma_{,z} (\beta_{,z}^\rho + \beta_{,\rho}^z) \\ & + \frac{1}{\psi} \left[4 (\beta_{,\rho}^\rho - \beta_{,z}^z - \rho\alpha\bar{\Omega}) \psi_{,\rho} + 6 (\beta_{,z}^\rho + \beta_{,\rho}^z) \psi_{,z} \right] - \frac{2}{3}\rho\alpha [3\bar{\Omega}\sigma_{,\rho} + \bar{\Omega}_{,\rho}] - \frac{8}{3}\alpha\bar{\Omega} \\ & - 16\pi \frac{\alpha\tilde{S}_\rho}{\psi^6} - \frac{\alpha\rho\tilde{\omega}_\rho\tilde{\omega}^t}{\psi^{12}e^{4\sigma}} = 0, \end{aligned} \quad (5.37)$$

$$\begin{aligned} & \beta_{,\rho\rho}^z + \frac{4}{3}\beta_{,zz}^z - \frac{1}{3}\beta_{,\rho z}^\rho + \frac{1}{\alpha} \left[\frac{4}{3} (\beta_{,\rho}^\rho - \beta_{,z}^z) \alpha_{,z} - (\beta_{,\rho}^z + \beta_{,z}^\rho) \alpha_{,\rho} \right] + \frac{1}{\rho} (\beta_{,z}^\rho + \beta_{,\rho}^z) + \sigma_{,\rho} (\beta_{,z}^\rho + \beta_{,\rho}^z) \\ & + \frac{1}{\psi} \left[4 (2\beta_{,z}^z - 2\beta_{,\rho}^\rho - \rho\alpha\bar{\Omega}) \psi_{,z} + 6 (\beta_{,z}^\rho + \beta_{,\rho}^z) \psi_{,\rho} \right] - \frac{2}{3}\rho\alpha [3\bar{\Omega}\sigma_{,z} + \bar{\Omega}_{,z}] + 2 (\beta_{,z}^z - \beta_{,\rho}^\rho) \sigma_{,z} \\ & - 16\pi \frac{\alpha\tilde{S}_z}{\psi^6} - \frac{\alpha\rho^2\tilde{\omega}_z\tilde{\omega}^t}{\psi^{12}e^{4\sigma}} = 0. \end{aligned} \quad (5.38)$$

The Hamiltonian constraint provides an equation for ψ :

$$\begin{aligned} & \frac{8}{\psi} \left[\psi_{,\rho\rho} + \psi_{,zz} + \frac{1}{\rho}\psi_{,\rho} + \psi_{,z}\sigma_{,z} + \psi_{,\rho}\sigma_{,\rho} \right] + 2(\sigma_{,\rho})^2 + 2(\sigma_{,z})^2 + \frac{4}{\rho}\sigma_{,\rho} + 2\sigma_{,zz} + 2\sigma_{,\rho\rho} \\ & + \psi^4 \left\{ \frac{2}{3}\rho^2\bar{\Omega}^2 + \frac{2\rho\bar{\Omega}}{3\alpha} (\beta_{,\rho}^\rho - \beta_{,z}^z) + \frac{1}{\alpha^2} \left[\frac{2}{3} (\beta_{,z}^z)^2 + \frac{2}{3} (\beta_{,\rho}^\rho)^2 + \frac{1}{2} (\beta_{,z}^\rho)^2 + \beta_{,z}^\rho\beta_{,\rho}^z + \frac{1}{2} (\beta_{,\rho}^z)^2 - \frac{4}{3}\beta_{,\rho}^\rho\beta_{,z}^z \right] \right\} \\ & + 16\pi \frac{(\tilde{\tau} + \tilde{D})}{\psi^2} + \frac{\tilde{\omega}_\rho^2 + \tilde{\rho}^2\tilde{\omega}_z^2}{2e^{4\sigma}\psi^8} + \frac{1}{2} \frac{\rho^2\tilde{\omega}^t{}^2}{\psi^{12}e^{4\sigma}} = 0, \end{aligned} \quad (5.39)$$

The slicing condition, which fixes the lapse, α , is derived from ${}^{(3)}K^i_i = 0$ and $\partial/\partial t ({}^{(3)}K^i_i) = 0$:

$$\begin{aligned} & \alpha_{,\rho\rho} + \alpha_{,zz} + \alpha_{,z}\sigma_{,z} + \alpha_{,\rho}\sigma_{,\rho} + \frac{1}{\rho}\alpha_{,\rho} + \frac{2}{\psi}(\psi_{,\rho}\alpha_{,\rho} + \psi_{,z}\alpha_{,z}) \\ & + \psi^4 \left\{ -\frac{2}{3} [\rho^2 \bar{\Omega}^2 \alpha + (\beta_{,\rho}^\rho - \beta_{,z}^z) \rho \bar{\Omega}] + \frac{1}{\alpha} \left[-\frac{2}{3} (\beta_{,\rho}^\rho)^2 - \frac{2}{3} (\beta_{,z}^z)^2 - \frac{1}{2} (\beta_{,z}^\rho)^2 - \frac{1}{2} (\beta_{,\rho}^z)^2 - \beta_{,z}^\rho \beta_{,\rho}^z + \frac{4}{3} \beta_{,\rho}^\rho \beta_{,z}^z \right] \right\} \\ & - 4\pi \frac{\alpha}{\psi^2} (\tilde{\tau} + 3\tilde{P} + \tilde{D}) - 4\pi \frac{\alpha}{\psi^6} \left[\frac{\tilde{S}_z^2 + \tilde{S}_\rho^2}{\tilde{\tau} + \tilde{D} + \tilde{P}} + \frac{\tilde{S}_\phi^2}{\rho^2 e^{2\sigma} (\tilde{\tau} + \tilde{D} + \tilde{P})} \right] - \frac{\alpha}{2e^{4\sigma} \psi^8} (\rho^2 \tilde{\omega}_z^2 + \tilde{\omega}_\rho^2) = 0. \end{aligned} \quad (5.40)$$

The spatial components of the twist, ω_A , satisfy the following constraint, calculated from (5.4):

$$3\rho \tilde{\omega}_z + \rho^2 \tilde{\omega}_{z,\rho} - \rho \tilde{\omega}_{\rho,z} + 16\pi \tilde{S}_\phi e^\sigma = 0. \quad (5.41)$$

In addition, the twist components satisfy the following evolution equations, also obtained from (5.4):

$$\begin{aligned} \tilde{\omega}_{\rho,t} &= 16\pi \frac{e^\sigma \beta^z}{\rho} \tilde{S}_\phi + (\tilde{\omega}_{z,\rho} \beta^z + \beta_{,\rho}^z \tilde{\omega}_z) \rho + 3\tilde{\omega}_z \beta^z + \beta^\rho \tilde{\omega}_{\rho,\rho} + \beta_{,\rho}^\rho \tilde{\omega}_\rho + 2 \frac{\beta^\rho \tilde{\omega}_\rho}{\rho} \\ &+ \frac{1}{\psi^4} \left[-16\pi \alpha e^\sigma \frac{\tilde{S}_\phi \tilde{S}_z}{\rho (\tilde{\tau} + \tilde{D} + \tilde{P})} - (\tilde{\omega}_{,\rho}^t \alpha + \tilde{\omega}^t \alpha_{,\rho}) \rho - 3\tilde{\omega}^t \alpha \right] \\ &+ 4 \frac{\psi_{,\rho} \rho \alpha \tilde{\omega}^t}{\psi^5}, \end{aligned} \quad (5.42)$$

$$\begin{aligned} \tilde{\omega}_{z,t} &= -16\pi \frac{e^\sigma \beta^\rho}{\rho^2} \tilde{S}_\phi + \beta_{,z}^z \tilde{\omega}_z + \beta^z \tilde{\omega}_{z,z} + \frac{1}{\rho} (\tilde{\omega}_{\rho,z} \beta^\rho + \beta_{,\rho}^z \tilde{\omega}_\rho) \\ &+ \frac{1}{\psi^4} \left[16\pi \frac{\tilde{S}_\phi \tilde{S}_\rho \alpha e^\sigma}{\rho^2 (\tilde{\tau} + \tilde{D} + \tilde{P})} - \tilde{\omega}_{,z}^t \alpha - \tilde{\omega}^t \alpha_{,z} \right] + 4 \frac{\psi_{,z} \alpha \tilde{\omega}^t}{\psi^5}. \end{aligned} \quad (5.43)$$

Expression (5.8) provides an evolution equation for $\tilde{\omega}^t$:

$$\begin{aligned} \tilde{\omega}_{,t}^t &= -2\tilde{\omega}^t \alpha \bar{\Omega} \rho + (-\tilde{\omega}_{z,z} + 3\tilde{\omega}_z \sigma_{,z}) \alpha - \tilde{\omega}_z \alpha_{,z} + 2\beta_{,z}^z \tilde{\omega}^t + \beta^z \tilde{\omega}_{,z}^t + \beta^\rho \tilde{\omega}_{,\rho}^t \\ &+ \frac{1}{\rho} [(3\tilde{\omega}_{\rho}\sigma_{,\rho} - \tilde{\omega}_{\rho,\rho}) \alpha - \omega_\rho \alpha_{,\rho} + 3\tilde{\omega}^t \beta^\rho] + \frac{\tilde{\omega}_\rho \alpha}{\rho^2} + \frac{6\tilde{\omega}_z \psi_{,z} \alpha}{\psi} + 6 \frac{\tilde{\omega}_\rho \alpha \psi_{,\rho}}{\rho \psi}. \end{aligned} \quad (5.44)$$

From the definition of $\bar{\Omega}$ we get an evolution equation for σ :

$$\sigma_{,t} = \frac{1}{\rho} (\beta^\rho \sigma_{,\rho} \rho + \beta^z \sigma_{,z} \rho - \rho^2 \alpha \bar{\Omega} - \beta_{,\rho}^\rho \rho + \beta^\rho). \quad (5.45)$$

The evolution equation for $\bar{\Omega}$ is derived from (5.3):

$$\begin{aligned} \bar{\Omega}_{,t} &= \beta^\rho \bar{\Omega}_{,\rho} + \beta^z \bar{\Omega}_{,z} + \frac{\beta^\rho \bar{\Omega}}{\rho} + \frac{1}{2} \frac{(\beta_{,\rho}^\rho)^2 - (\beta_{,z}^z)^2}{\rho \alpha} - \alpha \frac{(\sigma_{,z})^2 + \sigma_{,zz}}{\psi^4 \rho} - \frac{\alpha_{,z} \sigma_{,z} + \alpha_{,\rho} \sigma_{,\rho} - \alpha_{,\rho\rho}}{\rho \psi^4} - \frac{\alpha_{,\rho}}{\rho^2 \psi^4} \\ &- 2 \frac{(\sigma_{,\rho} \rho + 1) \alpha + 2\alpha_{,\rho} \rho}{\rho^2 \psi^5} \psi_{,\rho} - 2 \frac{\sigma_{,z} \alpha \psi_{,z}}{\rho \psi^5} + 2 \frac{\psi_{,\rho} \rho \alpha}{\psi^5 \rho} - 6 \frac{\alpha (\psi_{,\rho})^2}{\rho \psi^6} - \frac{\alpha}{2} \frac{2\tilde{\omega}_z^2 \rho^2 + \tilde{\omega}_\rho^2}{\rho e^{4\sigma} \psi^{12}} + \frac{\tilde{\omega}^t \rho \alpha}{e^{4\sigma} \psi^{16}} \\ &+ 8\pi \frac{\alpha}{\psi^{10}} \left[\frac{\tilde{S}_\rho^2}{\rho (\tilde{\tau} + \tilde{D} + \tilde{P})} - \frac{\tilde{S}_\phi^2}{\rho^3 (\tilde{\tau} + \tilde{D} + \tilde{P}) e^{2\sigma}} \right]. \end{aligned} \quad (5.46)$$

Finally, an evolution equation for the conformal factor ψ can be derived from ${}^{(3)}K_i{}^i = 0$:

$$\psi_{,t} = \beta^\rho \psi_{,\rho} + \frac{1}{3} \beta^\rho_{,\rho} \psi + \beta^z \psi_{,z} + \frac{1}{6} \psi \beta^z_{,z} + \frac{1}{6} \psi \rho \alpha \bar{\Omega}. \quad (5.47)$$

This completes the set of equations that we consider for the geometry. Note that not all the equations are independent of each other. In particular, equations (5.47) and (5.55) are both equations which can be used to update ψ . In the case of fully constrained evolution we use (5.55) for that purpose, while (5.47) is used in a partially constrained evolution.

5.2.2 Fluids

We now consider the axisymmetric hydrodynamic equations within the 2+1+1 formalism. As usual, the equations governing the evolution of the fluid may be derived from the conservation laws (1.36) and (1.37). Since we want to take advantage of HRSC methods (which have been proven to be very successful in the study of relativistic hydrodynamics) we need to cast the equations in conservation law form. In addition, the equations need to be adapted to the 2+1+1 decomposition of the spacetime. Since the complete derivation of the equations is somewhat lengthy, we simply state them here; details of the derivation are included in App. C.

$$\frac{\partial}{\partial t} \left\{ e^\sigma \tilde{D} \right\} + \frac{1}{\rho} \frac{\partial}{\partial \rho} \left\{ \alpha \rho e^\sigma \tilde{D} \left[v^\rho - \frac{\beta^\rho}{\alpha} \right] \right\} + \frac{\partial}{\partial z} \left\{ \alpha e^\sigma \tilde{D} \left[v^z - \frac{\beta^z}{\alpha} \right] \right\} = 0, \quad (5.48)$$

$$\begin{aligned} & \frac{\partial}{\partial t} \left\{ e^\sigma \tilde{\tau} \right\} + \frac{1}{\rho} \frac{\partial}{\partial \rho} \left\{ \alpha \rho e^\sigma \left[\tilde{\tau} \left(v^\rho - \frac{\beta^\rho}{\alpha} \right) + \tilde{P} v^\rho \right] \right\} + \frac{\partial}{\partial z} \left\{ \alpha e^\sigma \left[\tilde{\tau} \left(v^z - \frac{\beta^z}{\alpha} \right) + \tilde{P} v^z \right] \right\} \\ & = \frac{S_{\tilde{\tau}}}{\rho}, \end{aligned} \quad (5.49)$$

$$\begin{aligned} & \frac{\partial}{\partial t} \left\{ e^\sigma \tilde{S}_A \right\} + \frac{1}{\rho} \frac{\partial}{\partial \rho} \left\{ \alpha \rho e^\sigma \left[\tilde{S}_A \left(v^\rho - \frac{\beta^\rho}{\alpha} \right) + \tilde{P} \delta_A^\rho \right] \right\} + \frac{\partial}{\partial z} \left\{ \alpha e^\sigma \left[\tilde{S}_A \left(v^z - \frac{\beta^z}{\alpha} \right) + \tilde{P} \delta_A^z \right] \right\} \\ & = \frac{S_{\tilde{S}_A}}{\rho}, \end{aligned} \quad (5.50)$$

$$\frac{\partial}{\partial t} \left\{ e^\sigma \tilde{S}_\phi \right\} + \frac{1}{\rho} \frac{\partial}{\partial \rho} \left\{ \alpha \rho e^\sigma \tilde{S}_\phi \left[v^\rho - \frac{\beta^\rho}{\alpha} \right] \right\} + \frac{\partial}{\partial z} \left\{ \alpha e^\sigma \tilde{S}_\phi \left[v^z - \frac{\beta^z}{\alpha} \right] \right\} = 0. \quad (5.51)$$

In the above equations we have introduced the following source terms, noting that they do not contain any explicit derivatives of the hydrodynamical variables:

$$\begin{aligned}
S_{\tilde{\tau}} = & \left\{ \tilde{P}\rho e^\sigma + \frac{\tilde{S}_\phi^2}{\psi^4 \rho e^\sigma (\tilde{\tau} + \tilde{D} + \tilde{P})} \right\} \left[\frac{2}{\psi} \left(-\frac{\partial \psi}{\partial t} + \beta^\rho \frac{\partial \psi}{\partial \rho} + \beta^z \frac{\partial \psi}{\partial z} \right) - \frac{\partial \sigma}{\partial t} + \beta^\rho \frac{\partial \sigma}{\partial \rho} + \beta^z \frac{\partial \sigma}{\partial z} \right] + \\
& \frac{1}{3} \rho e^\sigma \left\{ \tilde{P} - \frac{(\tilde{S}_\rho^2 - 2\tilde{S}_z^2)}{(\tilde{\tau} + \tilde{D} + \tilde{P}) \psi^4} \right\} \left(-\frac{\partial \beta^\rho}{\partial \rho} + \frac{\partial \beta^z}{\partial z} \right) - \frac{\rho e^\sigma}{\psi^4} \left(\tilde{S}_\rho \frac{\partial \alpha}{\partial \rho} + \tilde{S}_z \frac{\partial \alpha}{\partial z} \right) + \\
& \rho e^\sigma \frac{\tilde{S}_\rho \tilde{S}_z}{\psi^4 (\tilde{\tau} + \tilde{D} + \tilde{P})} \left(\frac{\partial \beta^\rho}{\partial z} + \frac{\partial \beta^z}{\partial \rho} \right) + \tilde{P} \left[-\frac{2}{3} \rho^2 \tilde{\Omega} \alpha e^\sigma + \beta^\rho e^\sigma \right] - \frac{1}{3} \rho^2 \alpha e^\sigma \tilde{\Omega} \frac{(\tilde{S}_\rho^2 + \tilde{S}_z^2)}{(\tilde{\tau} + \tilde{D} + \tilde{P}) \psi^4} + \\
& \frac{\tilde{S}_\phi}{\psi^4 \rho e^\sigma (\tilde{\tau} + \tilde{D} + \tilde{P})} \left[\tilde{S}_\phi \frac{\beta^\rho}{\rho} + \frac{\alpha \rho e^{-\sigma}}{\psi^6} (-\rho \tilde{\omega}_z \tilde{S}_\rho + \tilde{\omega}_\rho \tilde{S}_z) \right], \tag{5.52}
\end{aligned}$$

$$\begin{aligned}
S_{\tilde{S}_\rho} = & \left\{ \frac{2\alpha \rho e^\sigma}{(\tilde{\tau} + \tilde{D} + \tilde{P}) \psi^5} \left[\tilde{S}_\rho^2 + \tilde{S}_z^2 + \frac{e^{-2\sigma}}{\rho^2} \tilde{S}_\phi^2 \right] + 6 \frac{\rho \alpha e^\sigma}{\psi} \tilde{P} \right\} \frac{\partial \psi}{\partial \rho} + \\
& \left\{ \frac{\alpha e^{-\sigma}}{\rho \psi^4} \frac{\tilde{S}_\phi^2}{(\tilde{\tau} + \tilde{D} + \tilde{P})} + \alpha \rho e^\sigma \tilde{P} \right\} \frac{\partial \sigma}{\partial \rho} - \rho e^\sigma (\tilde{\tau} + \tilde{D}) \frac{\partial \alpha}{\partial \rho} + \\
& \rho e^\sigma \left[\tilde{S}_\rho \frac{\partial \beta^\rho}{\partial \rho} + \tilde{S}_z \frac{\partial \beta^z}{\partial \rho} \right] + \tilde{P} \alpha e^\sigma + \\
& \frac{\alpha}{\psi^4 \rho e^\sigma} \left\{ \frac{e^{-\sigma}}{\psi^6} \rho^2 \tilde{\omega}^t \frac{\tilde{S}_z}{(\tilde{\tau} + \tilde{D} + \tilde{P})} + \frac{1}{\rho} \frac{\tilde{S}_\phi}{(\tilde{\tau} + \tilde{D} + \tilde{P})} - \tilde{\omega}_z \frac{\rho^2}{\psi^2} e^{-\sigma} \right\} \tilde{S}_\phi, \tag{5.53}
\end{aligned}$$

$$\begin{aligned}
S_{\tilde{S}_z} = & \left\{ \frac{2\alpha \rho e^\sigma}{(\tilde{\tau} + \tilde{D} + \tilde{P}) \psi^5} \left[\tilde{S}_\rho^2 + \tilde{S}_z^2 + \frac{e^{-2\sigma}}{\rho^2} \tilde{S}_\phi^2 \right] + 6 \frac{\rho \alpha e^\sigma}{\psi} \tilde{P} \right\} \frac{\partial \psi}{\partial z} + \\
& \left\{ \frac{\alpha e^{-\sigma}}{\rho \psi^4} \frac{\tilde{S}_\phi^2}{(\tilde{\tau} + \tilde{D} + \tilde{P})} + \alpha \rho e^\sigma \tilde{P} \right\} \frac{\partial \sigma}{\partial z} - \rho e^\sigma (\tilde{\tau} + \tilde{D}) \frac{\partial \alpha}{\partial z} + \\
& \rho e^\sigma \left[\tilde{S}_\rho \frac{\partial \beta^\rho}{\partial z} + \tilde{S}_z \frac{\partial \beta^z}{\partial z} \right] + \\
& \frac{\alpha}{\psi^4 \rho e^\sigma} \left\{ -\frac{e^{-\sigma}}{\psi^6} \rho^2 \tilde{\omega}^t \frac{\tilde{S}_\rho}{(\tilde{\tau} + \tilde{D} + \tilde{P})} + \tilde{\omega}_\rho \frac{\rho}{\psi^2} e^{-\sigma} \right\} \tilde{S}_\phi. \tag{5.54}
\end{aligned}$$

Exploiting the fact that the coupled Einstein/hydrodynamical field equations presented in this and the previous section are over-determined due to the general covariance of the theory (equivalently the existence of the constraint equations), we can perform a non-trivial check of their overall

consistency. In particular we have demonstrated that the expression resulting from application of $(\partial^2_{\rho\rho} + \partial^2_{zz})$ to the right hand side of (5.47) coincides with the expression obtained by taking the time derivative of the right hand side of the Hamiltonian constraint (5.55) written in the form

$$\begin{aligned}
& \psi_{,\rho\rho} + \psi_{,zz} = \\
& -\frac{1}{\rho}\psi_{,\rho} - \psi_{,z}\sigma_{,z} - \psi_{,\rho}\sigma_{,\rho} - \frac{\psi}{8} \left\{ 2(\sigma_{,\rho})^2 + 2(\sigma_{,z})^2 + \frac{4}{\rho}\sigma_{,\rho} + 2\sigma_{,zz} + 2\sigma_{,\rho\rho} \right. \\
& \left. + \psi^4 \left\{ \frac{2}{3}\rho^2\bar{\Omega}^2 + \frac{2}{3}\frac{\rho\bar{\Omega}}{\alpha}(\beta^{\rho} - \beta^z) + \frac{1}{\alpha^2} \left[\frac{2}{3}(\beta^z)^2 + \frac{2}{3}(\beta^{\rho})^2 + \frac{1}{2}(\beta^z_{,z})^2 + \beta^{\rho}_{,z}\beta^z_{,\rho} + \frac{1}{2}(\beta^z_{,\rho})^2 - \frac{4}{3}\beta^{\rho}_{,\rho}\beta^z_{,z} \right] \right\} \right. \\
& \left. + 16\pi \frac{(\tilde{\tau} + \tilde{D})}{\psi^2} + \frac{\tilde{\omega}_{\rho}^2 + \tilde{\rho}^2\tilde{\omega}_z^2}{2e^{4\sigma}\psi^8} + \frac{1}{2}\frac{\rho^2\tilde{\omega}^{t2}}{\psi^{12}e^{4\sigma}} \right\}. \tag{5.55}
\end{aligned}$$

Demonstration of the equivalence of the two expressions requires the use of most of the equations of motion. The calculation was carried out using the algebraic manipulation program, Maple [64].

5.2.3 Boundary and Regularity conditions

In order to solve the differential equations presented in the previous section, we need to provide boundary and regularity conditions. Here we restrict attention to the non-rotating case, since we have yet to incorporate angular momentum into our code. The boundary conditions at the outer edges of the (finite) computational domain are a combination of approximate Sommerfeld conditions and relations that follow from asymptotic flatness. More specifically, quantities governed by elliptic equations, i.e. α , ψ , β^A , satisfy boundary conditions of the form (see [87])

$$f - f_{\infty} + \rho f_{,\rho} + z f_{,z} = 0, \tag{5.56}$$

where $\psi_{\infty} = \alpha_{\infty} = 1$ and $\beta^J_{\infty} = 0$. These conditions can be derived from the known large- r fall-off of the metric components for the case of an asymptotically flat spacetime. The variables $\bar{\sigma}$ and $\bar{\Omega}$, which are radiative in nature, satisfy approximate Sommerfeld conditions at the outer boundary of the computational domain, i.e. asymptotically these variables are assumed to be of the form $g = g(t-r)/r$, where $r \equiv \sqrt{\rho^2 + z^2}$. All of the dynamical fluid variables obey outflow boundary conditions.

Near the z -axis, regularity dictates that α , ψ , β^z , \tilde{D} , $\tilde{\tau}$ and \tilde{S}_z are even functions of ρ , which implies that their first derivatives vanish at $\rho = 0$. On the other hand $\bar{\sigma}$, β^{ρ} and \tilde{S}_{ρ} are odd functions and thus go to zero at least linearly in ρ as $\rho \rightarrow 0$.

5.3 Initial Data for Rotating Stars

Although the particular implementation to solve the relativistic hydrodynamic equations presented in this thesis does not allow for rotating configurations, one of our long-term goals is to study the collapse of rotating stars. For that reason the equilibrium equations for self gravitating perfect fluid configurations with non-trivial angular momentum are presented in this section. A good introduction to this topic is the review paper by Stergioulas [97], where the basic formalism and the main implementations to date are discussed. Here, we will derive the equilibrium equations directly from the dynamical equations introduced in the Secs. 5.2.1 and 5.2.2. In addition to assuming that the time derivatives of the metric and the fluid quantities vanish, we impose the following conditions: $\beta^A = \tilde{S}_A = \tilde{\Omega} = 0 = \tilde{\omega}^t = 0$. These choices are made to eliminate any terms that “source” time derivatives in the evolution equations. If upon setting the time derivatives of the dynamical variables to be zero at the initial time, we find that the evolution equations imply that the time derivatives vanish for *all* times, then the spacetime is stationary and our coordinates are adapted to the time-translational symmetry, i.e. to the timelike Killing vector field. We thus believe that by imposing the above conditions we have not restricted the type of axisymmetric stationary solutions that can be obtained.

From (5.50) we then get the following two equations:

$$\begin{aligned} \tilde{P}_{,\rho} = & \left[\frac{2e^{-2\sigma}\tilde{S}_\phi^2}{\rho^2\psi^4(\tilde{\tau} + \tilde{D} + \tilde{P})} + 6\tilde{P} \right] \frac{\psi_{,\rho}}{\psi} + \frac{e^{-2\sigma}\tilde{S}_\phi^2}{\rho^2\psi^4(\tilde{\tau} + \tilde{D} + \tilde{P})} \sigma_{,\rho} \\ & - (\tilde{\tau} + \tilde{D} + \tilde{P}) \frac{\alpha_{,\rho}}{\alpha} + \frac{1}{\psi^4\rho^2e^{2\sigma}} \left[\frac{\tilde{S}_\phi^2}{\rho(\tilde{\tau} + \tilde{D} + \tilde{P})} - \frac{\rho^2e^{-\sigma}\tilde{\omega}_z}{\psi^2}\tilde{S}_\phi \right], \end{aligned} \quad (5.57)$$

$$\begin{aligned} \tilde{P}_{,z} = & \left[\frac{2e^{-2\sigma}\tilde{S}_\phi^2}{\rho^2\psi^4(\tilde{\tau} + \tilde{D} + \tilde{P})} + 6\tilde{P} \right] \frac{\psi_{,z}}{\psi} + \frac{e^{-2\sigma}\tilde{S}_\phi^2}{\rho^2\psi^4(\tilde{\tau} + \tilde{D} + \tilde{P})} \sigma_{,z} \\ & - (\tilde{\tau} + \tilde{D} + \tilde{P}) \frac{\alpha_{,z}}{\alpha} + \frac{\tilde{\omega}_\rho}{\rho\psi^6e^{3\sigma}}\tilde{S}_\phi. \end{aligned} \quad (5.58)$$

Equation (5.46) gives the following condition:

$$\begin{aligned} & -(\sigma_{,z})^2 - \sigma_{,zz} - \sigma_{,z} \frac{\alpha_{,z}}{\alpha} - \sigma_{,\rho} \frac{\alpha_{,\rho}}{\alpha} + \frac{\alpha_{,\rho\rho}}{\alpha} - \frac{\alpha_{,\rho}}{\rho\alpha} - 2 \left[\left(\sigma_{,\rho} + \frac{1}{\rho} \right) + 2 \frac{\alpha_{,\rho}}{\alpha} \right] \frac{\psi_{,\rho}}{\psi} - 2\sigma_{,z} \frac{\psi_{,z}}{\psi} \\ & + 2 \frac{\psi_{,\rho\rho}}{\psi} - 6 \left(\frac{\psi_{,\rho}}{\psi} \right)^2 - \frac{1}{2} \frac{2\tilde{\omega}_z^2\rho^2 + \tilde{\omega}_\rho^2}{e^{4\sigma}\psi^8} - 8\pi \frac{\tilde{S}_\phi^2}{\psi^6\rho^2(\tilde{\tau} + \tilde{D} + \tilde{P})e^{2\sigma}} = 0. \end{aligned} \quad (5.59)$$

The equation for the evolution of $\tilde{\omega}^t$ (5.44), yields:

$$\begin{aligned} & (-\tilde{\omega}_{z,z} + 3\tilde{\omega}_z\sigma_{,z})\alpha - \tilde{\omega}_{,z}\alpha_{,z} + \frac{1}{\rho} [(3\tilde{\omega}_\rho\sigma_{,\rho} - \tilde{\omega}_{\rho,\rho})\alpha - \tilde{\omega}_\rho\alpha_{,\rho}] \\ & \frac{\tilde{\omega}_\rho\alpha}{\rho^2} + 6\alpha \left[\tilde{\omega}_z \frac{\psi_{,z}}{\psi} + \frac{\tilde{\omega}_\rho}{\rho} \frac{\psi_{,\rho}}{\psi} \right] = 0, \end{aligned} \quad (5.60)$$

while the constraint equation for $\tilde{\omega}_A$ gives:

$$3\rho\tilde{\omega}_z + \rho^2\tilde{\omega}_{z,\rho} - \rho\tilde{\omega}_{\rho,z} + 16\pi\tilde{S}_\phi e^\sigma = 0. \quad (5.61)$$

The Hamiltonian constraint,

$$\begin{aligned} & \frac{8}{\psi} \left[\psi_{,\rho\rho} + \psi_{,zz} + \frac{1}{\rho}\psi_{,\rho} + \psi_{,z}\sigma_{,z} + \psi_{,\rho}\sigma_{,\rho} \right] + 2(\sigma_{,\rho})^2 + 2(\sigma_{,z})^2 + \frac{4}{\rho}\sigma_{,\rho} + 2\sigma_{,zz} + 2\sigma_{,\rho\rho} \\ & + 16\pi \frac{(\tilde{\tau} + \tilde{D})}{\psi^2} + \frac{\tilde{\omega}_\rho^2 + \rho^2\tilde{\omega}_z^2}{2e^{4\sigma}\psi^8} = 0, \end{aligned} \quad (5.62)$$

and the slicing condition,

$$\begin{aligned} & \alpha_{,\rho\rho} + \alpha_{,zz} + \alpha_{,z}\sigma_{,z} + \alpha_{,\rho}\sigma_{,\rho} + \frac{1}{\rho}\alpha_{,\rho} + \frac{2}{\psi}(\psi_{,\rho}\alpha_{,\rho} + \psi_{,z}\alpha_{,z}) \\ & - 4\pi \frac{\alpha}{\psi^2} (\tilde{\tau} + 3\tilde{P} + \tilde{D}) - 4\pi \frac{\alpha}{\psi^6} \frac{\tilde{S}_\phi^2}{\rho^2 e^{2\sigma} (\tilde{\tau} + \tilde{D} + \tilde{P})} - \frac{\alpha}{2e^{4\sigma}\psi^8} (\rho^2\tilde{\omega}_z^2 + \tilde{\omega}_\rho^2) = 0 \end{aligned} \quad (5.63)$$

must also be satisfied. Equations (5.57-5.63) are the equations of general relativistic, hydrostatic equilibrium for a rotating perfect fluid.

Following Stergioulas [97], we introduce a new function $\omega(\rho, z)$ such that $\xi_\mu = (s^2, \omega, 0, 0)$. We note that since our coordinates are adapted to the timelike and axial Killing vector fields, this function has an invariant geometric meaning. Specifically, if η^α is the timelike Killing vector field, then we have

$$\xi_\mu \eta^\mu = \xi_t = \omega(\rho, z), \quad (5.64)$$

where ω is a spacetime scalar. Moreover since $\xi_t = g_{t\phi}$ —again by our choice of coordinates— $\omega(\rho, z)$ is, asymptotically, proportional to the angular momentum of the spacetime.

In terms of this new function we can then write the spatial components of the twist vector as

$$\tilde{\omega}_\rho = -\frac{2\omega^{3/2}}{\rho\alpha} \left(\frac{\psi^2 e^\sigma}{\sqrt{\omega}} \right)_{,z} = -\frac{\psi^2 e^\sigma}{\rho\alpha} \left[4\omega \frac{\psi_{,z}}{\psi} + 2\omega\sigma_{,z} - \omega_{,z} \right], \quad (5.65)$$

$$\tilde{\omega}_z = \frac{2\omega^{3/2}}{\rho^3\alpha} \left(\frac{\rho\psi^2 e^\sigma}{\sqrt{\omega}} \right)_{,\rho} = \frac{2\psi^2 e^\sigma}{\rho^2\alpha} \left[\frac{\omega}{\rho} + 2\omega \frac{\psi_{,\rho}}{\psi} + \omega\sigma_{,\rho} - \frac{\omega_{,\rho}}{2} \right]. \quad (5.66)$$

These expressions for the twist vector components automatically satisfy equation (5.60). They also

yield an elliptic equation for ω that can be derived from (5.61):

$$\begin{aligned}
& \omega_{,\rho\rho} + \omega_{,zz} - \frac{(\rho\alpha\psi^2 e^\sigma)_{,\rho}}{\rho\alpha\psi^2 e^\sigma} \omega_{,\rho} - \frac{(\alpha\psi^2 e^\sigma)_{,z}}{\alpha\psi^2 e^\sigma} \omega_{,z} \\
& - 2 \left[\sigma_{,\rho\rho} + \sigma_{,zz} + (\sigma_{,\rho})^2 + (\sigma_{,z})^2 \right] \omega - \frac{4\sigma_{,\rho}}{\rho} \omega + 2 [\alpha_{,z}\sigma_{,z} + \alpha_{,\rho}\sigma_{,\rho}] \frac{\omega}{\alpha} + 2 \frac{\alpha_{,\rho}\omega}{\rho\alpha} \\
& - 4 [\psi_{,\rho\rho} + \psi_{,zz} + 2\psi_{,\rho}\sigma_{,\rho} + 2\psi_{,z}\sigma_{,z}] \frac{\omega}{\psi} - 8 \frac{\psi_{,\rho}\omega}{\rho\psi} + 4 [\psi_{,\rho}\alpha_{,\rho} + \psi_{,z}\alpha_{,z}] \frac{\omega}{\alpha\psi} \\
& - 4\omega \frac{(\psi_{,\rho})^2 + (\psi_{,z})^2}{\psi^2} - 16\pi \frac{\alpha\tilde{S}_\phi}{\psi^2} = 0.
\end{aligned} \tag{5.67}$$

Defining $\omega = u\rho$, where u is yet another function that satisfies $\lim_{\rho \rightarrow 0} u(\rho, z) = \rho u_1(z) + O(\rho^3)$, we get

$$\begin{aligned}
& u_{,\rho\rho} + u_{,zz} + \left(\frac{u}{\rho} \right)_{,\rho} - \frac{(\alpha\psi^2 e^\sigma)_{,\rho} (\rho u)_{,\rho}}{\alpha\psi^2 e^\sigma \rho} - \frac{(\alpha\psi^2 e^\sigma)_{,z}}{\alpha\psi^2 e^\sigma} u_{,z} - 2 \left[\sigma_{,\rho\rho} + \sigma_{,zz} + (\sigma_{,\rho})^2 + (\sigma_{,z})^2 \right] u \\
& - \frac{4}{\rho} \sigma_{,\rho} u + 2 [\alpha_{,z}\sigma_{,z} + \alpha_{,\rho}\sigma_{,\rho}] \frac{u}{\alpha} + 2 \frac{\alpha_{,\rho}}{\alpha} \frac{u}{\rho} - 4 [\psi_{,\rho\rho} + \psi_{,zz} + 2\psi_{,\rho}\sigma_{,\rho} + 2\psi_{,z}\sigma_{,z}] \frac{u}{\psi} - 8 \frac{\psi_{,\rho}}{\psi} \frac{u}{\rho} \\
& + 4 [\psi_{,\rho}\alpha_{,\rho} + \psi_{,z}\alpha_{,z}] \frac{u}{\alpha\psi} - 4 \frac{u}{\psi^2} \left[(\psi_{,\rho})^2 + (\psi_{,z})^2 \right] - 16 \frac{\alpha\tilde{S}_\phi}{\rho\psi^2} = 0.
\end{aligned} \tag{5.68}$$

We now have a complete set of equilibrium equations. Naively, we might think that if we provide the form of the angular momentum function \tilde{S}_ϕ we could integrate equations (5.57), (5.58), (5.59), (5.62), (5.63) and (5.68), and obtain an equilibrium configuration. In practice, however, not all functions \tilde{S}_ϕ would produce a solution. In the next section we investigate the possible forms for the rotation function.

5.3.1 Integrability Condition

The equations presented in the previous section have an integrability condition. In particular we have two equations that could be used to compute the pressure—namely (5.57) and (5.58). For our system of equations to be consistent, it is clear that we must obtain the same result irrespective of which of the two is used. This condition restricts the allowable functional form of \tilde{S}_ϕ . In theory, we should be able to obtain the appropriate integrability condition, i.e. the condition on \tilde{S}_ϕ , by demanding that the derivative with respect to z of the right hand side of (5.57) agrees with the derivative with respect to ρ of the right hand side of (5.58). This specific procedure is somewhat difficult to carry through, and has not proven to be very illuminating. Instead we will follow Bonazzola et al. [8], but write their results in terms of the variables used in the other sections of this chapter.

The four velocity for the case of a stationary star can be written as

$$u^\mu = (u^\phi, W/\alpha, 0, 0), \tag{5.69}$$

where W is defined by equation (5.17) and α is the lapse function.

Starting from

$$u_\phi = g_{\phi\mu}u^\mu = \xi_t \frac{W}{\alpha} + s^2 u^\phi = W \frac{S_\phi}{\rho_0 h W^2}, \quad (5.70)$$

and assuming that $\xi_t = \omega$ (as was done previously), u^ϕ can be expressed in terms of the conservative variables as follows:

$$u^\phi = \frac{1}{s^2} \left(\frac{S_\phi}{\rho_0 h W} - \omega \frac{W}{\alpha} \right). \quad (5.71)$$

Again, following [8], this allows us to define a quantity Ω^* (not to be confused with $\bar{\Omega}$):

$$\Omega^* = \frac{u^\phi}{u^t} = \frac{1}{s^2} \left(\frac{\alpha S_\phi}{\rho_0 h W^2} - \omega \right) = \frac{1}{\rho^2 \psi^4 e^{2\sigma}} \left[\frac{\alpha \tilde{S}_\phi}{(\tilde{\tau} + \tilde{D} + \tilde{P})} - \omega \right]. \quad (5.72)$$

In terms of Ω^* , equations (5.57) and (5.58) take the compact form

$$\frac{\psi^6 W^2}{(\tilde{\tau} + \tilde{D} + \tilde{P})} P_{,A} = -\frac{\alpha_{,A}}{\alpha} + \frac{W_{,A}}{W} - \frac{W^2 \tilde{S}_\phi}{\alpha (\tilde{\tau} + \tilde{D} + \tilde{P})} \Omega^*_{,A}. \quad (5.73)$$

The above expressions can be further simplified by taking into account the following relationship,

$$\frac{\psi^6 W^2}{(\tilde{\tau} + \tilde{D} + \tilde{P})} = \frac{1}{\rho_0 (1 + \epsilon) + P} = \frac{1}{\rho_0 h} = \frac{1}{\rho_H + P}, \quad (5.74)$$

where we have used definitions (5.26-5.30) and the definition of ρ_H introduced in equation (1.33).

At least formally, we can define the following functions:

$$\mathcal{H} = \int \frac{dP}{\rho_H(P) + P}, \quad (5.75)$$

$$\mathcal{F} = -\frac{W^2 \tilde{S}_\phi}{\alpha (\tilde{\tau} + \tilde{D} + \tilde{P})}. \quad (5.76)$$

This allows us to write (5.73) in the following compact form:

$$(\mathcal{H} + \ln \alpha - \ln W)_{,A} = -\mathcal{F} \Omega^*_{,A}. \quad (5.77)$$

It is now easy to see that the demand that the mixed derivative of the left hand side of this expression give the same answer independently of the order of differentiation can be expressed as a condition on the variables appearing in the right hand side, namely

$$\mathcal{F}_{,z} \Omega^*_{,\rho} - \mathcal{F}_{,\rho} \Omega^*_{,z} = 0. \quad (5.78)$$

In [8] it is argued that the left hand side of (5.78) can be viewed as the Jacobian of the transformation between (ρ, z) to (\mathcal{F}, Ω^*) . The fact that the Jacobian is zero then implies that there exists a function Φ that relates \mathcal{F} and Ω^* , i.e. that:

$$\Phi(\mathcal{F}, \Omega^*) = 0. \quad (5.79)$$

In this case two possibilities exist:

- If $\Phi_{,\mathcal{F}} = 0$, then $\Phi(\Omega^*) = 0$ expresses the constancy of Ω^* ; this case is called *rigid rotation*.
- If $\Phi_{,\mathcal{F}} \neq 0$, then there is a relationship between \mathcal{F} and Φ that can be written as $\mathcal{F} = \mathcal{F}(\Omega^*)$; this case is called *differential rotation*.

In the case of differential rotation we can calculate the value of Ω^* in different parts of the star by fixing the form of $\mathcal{F}(\Omega^*)$ and then solving

$$\mathcal{F}(\Omega^*) + \frac{s^2 (s^2 \Omega^* + \omega)}{\alpha^2 s^2 - (s^2 \Omega^* + \omega)^2} = 0 \quad (5.80)$$

for Ω^* . In both cases (5.77) has a first integral. For the case of rigid rotation we have

$$\mathcal{H}(\rho, z) + \ln\left(\frac{\alpha}{W}\right)(\rho, z) = k, \quad (5.81)$$

while for differential rotation the integral is

$$\mathcal{H}(\rho, z) + \ln\left(\frac{\alpha}{W}\right)(\rho, z) + \int_{\Omega_0^*}^{\Omega^*(\rho, z)} \mathcal{F}(\Omega^*) d\Omega^* = k. \quad (5.82)$$

In both instances k is a constant. Finally let us point out that the Newtonian limit ($\rho\Omega^* \ll 1$) of case (5.80) takes the form

$$\mathcal{F}(\Omega^*) = -\rho^2 \Omega^*, \quad (5.83)$$

which implies that $\Omega^* = \Omega^*(\rho^2)$ —hence the terminology “differential rotation”.

5.4 Numerics

In this section we briefly describe several aspects of our numerical implementation. We start with a discussion of the treatment of the geometric equations, follow with a description of the integration of the hydrodynamic equations, then end with a discussion of issues arising from the coupling of the two systems of PDEs. To date we have only implemented the case of no rotation and therefore will restrict attention to the case $\tilde{S}_\phi = \tilde{\omega}^i = \xi^i = 0$ for the remainder of the thesis. The code has been implemented using RNPL (Rapid Numerical Prototyping Language) [65] with some specific routines written in Fortran 77.

The numerical approximation used for the geometric equations is explained in detail in [19] and [87]. It is based on second order centred finite difference approximations on a uniform grid in the (ρ, z) plane. More specifically the geometry is computed on a grid of points (see Figure 5.1) denoted by (ρ_i, z_j) where $i = 1, 2, \dots, N_\rho$, $j = 1, 2, \dots, N_z$ such that $\rho_{i+1} = \rho_i + \Delta\rho$ and $z_{j+1} = z_j + \Delta z$. Here $\Delta\rho$ and Δz constants and $\rho_1 = 0$, $\rho_{N_\rho} = \rho_{\max}$ and $z_1 = z_{\min}$, $z_{N_z} = z_{\max}$. In practice, we always compute with $\rho_{\max} = -z_{\min} = z_{\max}$, so that $\Delta z = \Delta\rho = h$ (which implies $N_z - 1 = 2(N_\rho - 1)$). In

addition we choose a discrete time step $\Delta t = \lambda h$, where the so-called Courant factor λ —which must generally satisfy $\lambda < 1/\sqrt{2}$ for stability of our numerical scheme—is held constant when we vary the spatial discretization scale, keeping the initial data fixed. Thus, the entire numerical scheme is characterized by the single discretization scale, h , which facilitates convergence testing of the results. The fluid is solved using a finite volume approximation which considers finite difference cells $C_{i+1/2 j+1/2}^{n+1/2}$ centred at $(\rho_{i+1/2}, z_{j+1/2})$.

As we have discussed in Sec. 5.2.1, when we perform a fully constrained evolution the only geometric evolution equations are those for σ and $\bar{\Omega}$, (5.45) and (5.46) respectively. These are discretized using a Crank-Nicholson scheme and second order centred differences for the spatial derivatives as in Chap. 2. We also again apply Kreiss-Oliger style dissipation [52] in order to damp high frequency components which cannot be properly represented at any given resolution, and which tend to result in instabilities in the code, especially near the z -axis. When we perform partially constrained evolution, we update ψ using (5.47) rather than via the Hamiltonian constraint. This evolution equation is also discretized using a Crank-Nicholson scheme.

Along with the evolution equations, discrete versions of the constraints (5.37-5.55) and the slicing condition (5.40) must be solved at each time step. These equations, which we assume are always elliptic, are discretized using second order centred finite difference approximations of the spatial derivatives. The resulting discrete systems are solved using an FAS (Full Approximation Storage) multigrid algorithm [9] to determine the advanced values of the discrete lapse and shift components, and, in the case of fully constrained evolution, the discrete conformal factor. The choice of multigrid is motivated by the fact that it is unique among general methods for the solution of finite-differenced non-linear elliptic systems in being able to produce a solution in $O(N)$ time, where N is the number of points in the spatial discretization ($N = N_z N_\rho$ in our case).

Multigrid algorithms are based on the observation that the decades-old technique of *relaxation*, while not a very efficient *solver* of discrete elliptic equations, is often a very efficient *smoother* of the equations. In particular, for the purposes of illustration, we consider a (scalar) elliptic problem written in the form

$$Lu = f, \tag{5.84}$$

where L is some elliptic differential operator (possibly nonlinear), u is the continuum solution, and f is a source function. (Note that u and f are functions of some number of independent variables; the multigrid technique can be applied in any number of spatial dimensions. Also, although the treatment of boundary conditions is an important issue, we will not consider it here since we only wish to illustrate the key ideas underlying the method.) We discretize (5.84) at some grid

resolution, h , as

$$L^h u^h = f^h. \quad (5.85)$$

Here, L^h is the discrete (difference) operator that approximates L , while u^h and f^h are the discrete solution and source, respectively. We note that at a given resolution, (5.85) will comprise N algebraic equations, where N is the number of grid points, and that we will generally be able to naturally associate one unknown (component of u^h) and one equation with any given grid point.

We now consider the specific case of *Gauss-Seidel relaxation*, which, as with all relaxation algorithms, proceeds iteratively. Each iteration, or relaxation sweep, consists of a visit to each grid point (in some prescribed order), where the value of the discrete unknown associated with that point is modified so that, instantaneously, its equation is satisfied. Denote by \tilde{u}^h the approximate solution of (5.85) at any stage of the iteration (so that, assuming that the relaxation converges, $\tilde{u}^h \rightarrow u^h$ in the limit of an infinite number of sweeps). Then we define the residual, \tilde{r}^h by

$$\tilde{r}^h \equiv L^h \tilde{u}^h - f^h, \quad (5.86)$$

and the solution error \tilde{e}^h by

$$\tilde{e}^h \equiv \tilde{u}^h - u. \quad (5.87)$$

By the observation noted above, (Gauss-Seidel) relaxation is generally not very efficient at *annihilating* \tilde{r}^h and \tilde{e}^h , but it *is* effective at smoothing (i.e. annihilating high frequency components) those quantities. This brings us to another key ingredient of multigrid algorithms—from which their name derives—and that is the use of a sequence of ever-coarser grids that are employed to accelerate the solution process.

In particular, once the residual (5.86) has been sufficiently smoothed (this generally requires only a few sweeps, typically 2-4), we can sensibly transfer the discrete problem to a coarser grid, which, from considerations of optimal efficiency, as well as programming convenience, is almost always characterized by a discretization scale $2h$. Specifically, on the coarse grid we pose the problem

$$L^{2h} u^{2h} = f^{2h} + \tilde{\tau}_h^{2h}, \quad (5.88)$$

where $\tilde{\tau}_h^{2h}$ is computed from

$$\tilde{\tau}_h^{2h} \equiv L^{2h} I_h^{2h} \tilde{u}^h - I_h^{2h} L^h \tilde{u}^h, \quad (5.89)$$

and I_h^{2h} is a so-called *restriction* operator that transfers a fine grid function to the coarse grid. It can be shown that $\tilde{\tau}_h^{2h}$ is an estimate of the truncation error, τ_h^{2h} , of the solution of the coarse grid discrete system $L^{2h} u^{2h} = f^{2h}$ relative to the fine grid problem (5.85). τ_h^{2h} has the property that the solution, \hat{u}^{2h} , of

$$L^{2h} \hat{u}^{2h} = f^{2h} + \tau_h^{2h}, \quad (5.90)$$

is *precisely* the solution of the fine grid problem (5.85), transferred to the coarse grid, i.e.

$$\hat{u}^{2h} = I_h^{2h} u^h. \quad (5.91)$$

Thus, τ_h^{2h} (and thus also the approximation $\tilde{\tau}_h^{2h}$) *corrects* the right hand side of a coarse grid problem, allowing—in principle—solutions with fine grid accuracy to be computed on the coarse grid.

The coarse problem (5.88) is significantly less costly to solve than the original fine grid equations (5.85), since in d dimensions it involves $N/2^d$ unknowns. More importantly, however, we can apply the above strategy recursively. That is, we perform relaxation sweeps of (5.88) until the corresponding residuals and solution errors are smooth, then transfer to a grid with resolution $4h$ etc., until we eventually are using a grid that has so few points, that actually *solving* the discrete equations is very cheap, even if we use a direct method (i.e. *simultaneous* solution of all of the algebraic equations) rather than relaxation.

Once the coarsest-level problem is solved, we begin to work our way back to the fine grid, via a sequence of coarse-to-fine grid transfers. In particular, having (approximately) solved a $2h$ problem, yielding \tilde{u}^{2h} , we update the finer-grid unknown, \tilde{u}^h using

$$\tilde{u}^h := I_{2h}^h (\tilde{u}^{2h} - I_h^{2h} \tilde{u}^h) \quad (5.92)$$

where I_{2h}^h is a so-called prolongation operator that transfers coarse grid functions to a fine grid. After each of these updates, we again apply a few relaxation sweeps to (5.85) in order to kill any high frequency components produced by the prolongation operation. Once we are back on the fine grid, we will have completed what is known as a V -cycle, and will generally find that the norm of the residuals and solution errors will have been reduced by some constant factor. Additional V -cycles can then be applied as needed in order to drive the residual below some convergence threshold.

This completes the description of the basic operation of a multigrid method. The particular choice of restriction and propagation operators, and some other specifics of the algorithm used in the axisymmetric code are explained in [19],[87].

We now move on to the hydrodynamic equations, (5.48-5.50), which are integrated via a finite volume approximation similar to the one described in Chap. 4. Note that these equations are of the type:

$$\frac{\partial}{\partial t} (e^\sigma \rho \mathbf{q}) s + \frac{1}{\rho} \frac{\partial}{\partial \rho} (\alpha \rho e^\sigma \mathbf{F}^\rho) + \frac{\partial}{\partial z} (\alpha e^\sigma \mathbf{F}^z) = \mathbf{S}. \quad (5.93)$$

In order to derive a finite volume approximation, the equations are integrated over a control volume defined by $C_{i+1/2, j+1/2}^{n+1/2} \equiv (t^n, t^{n+1}) \times (\rho_i, \rho_{i+1}) \times (z_j, z_{j+1})$, as shown in Fig. 5.1.

In solving the hydrodynamical equations, we also decided to implement a generalization of the HRSC method explained in Sec. 4.3.2. With this approach an approximate Riemann problem is solved at each cell interface to find an expression for the numerical flux. More specifically, the two fluxes \mathbf{F}^ρ and \mathbf{F}^z are evaluated via Roe approximations of the type given by expression (4.56). In turn, the Roe fluxes depend on the characteristic structure of equations (5.48-5.50) as described in App. D. The calculation of the fluid quantities at cell boundaries is performed using a one dimensional minmod reconstruction, also described in 4.3.2.

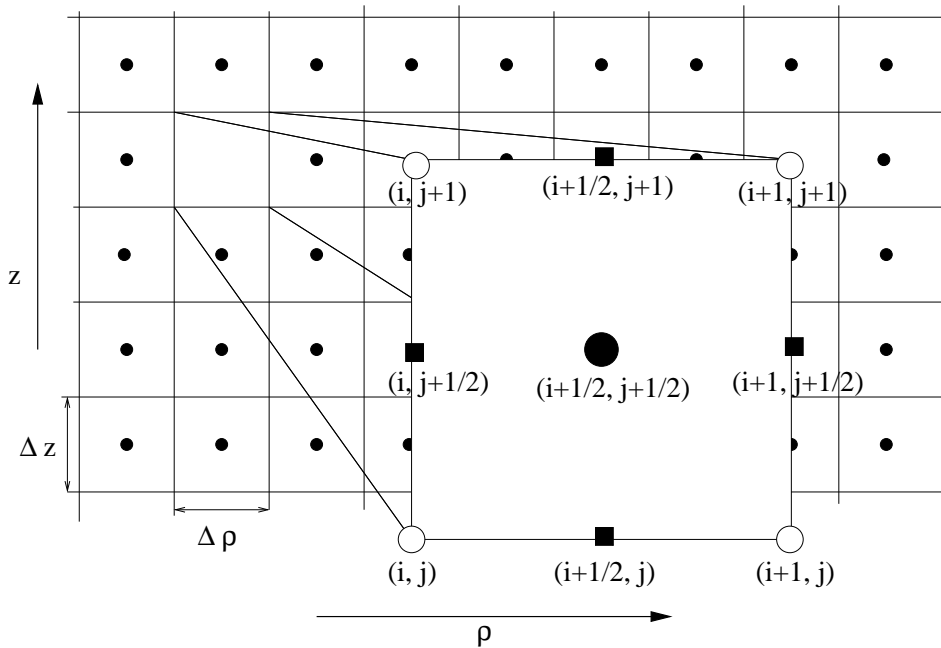


Figure 5.1: This figure shows a detail of the projection onto the ρ - z plane of the finite-volume (cell-based) grid used in the numerical solution of the coupled Einstein/hydrodynamical equations in axisymmetry. Note that the fluid variables are computed at points denoted by $(i + 1/2, j + 1/2)$. The ρ fluxes are computed at a location $(i, j + 1/2)$, and the z fluxes at $(i + 1/2, j)$. Geometric variables, on the other hand, are computed at locations labelled with open circles. In order to obtain values of the fluid variables at these last locations, or to compute values of the geometric variables at the cell centres, second order (bi-linear) interpolation is used.

As was the case in spherical symmetry, because of our choice of (topologically) cylindrical coordinates, one of the fluid equations contains a term which is explicitly divergent as ρ approaches zero. In particular one contribution to the ρ flux in (5.50), which governs S_ρ , contains a term P/ρ . This term is explicitly canceled, before discretization, by a corresponding term in the source

of (5.50).

Finally, the way in which we perform the update of the coupled Einstein/hydrodynamical variables to advance the discrete solution from time t to time $t + \Delta t$ is as follows.

1. Initialize the values of the geometry and the fluid at $t + \Delta t$ (advanced values) to the previously computed values at time t (retarded values).
2. Improve the estimate of the advanced geometric variables governed by evolution equations by performing a Crank-Nicholson iteration.
3. Improve the estimate of the advanced constrained geometric variables by performing a multi-grid V-cycle on the system of constraint equations.
4. Improve the advanced fluid quantities, \mathbf{q}^{n+1} , using a two step method analogous to that described in Sec. 4.3.2.
5. Repeat steps 2-4 until the the norm of the change in \mathbf{q}^{n+1} , the norm of the residual of the constraints, and the norm of the residuals of the Crank-Nicholson iteration are below some tolerance.

5.5 Results

In order to test the validity of our numerical implementation, we have performed various tests. Setting all the metric coefficients to be those of Minkowski spacetime—namely $\alpha \equiv 1$, $\beta^A \equiv 0$, $\bar{\sigma} \equiv 0$, $\psi \equiv 1$ —we have tested the part of the code that solves the hydrodynamic equations. Specifically, we have verified that the code is able to properly evolve discontinuous initial data, with surfaces of discontinuity defined by $\rho = \text{const.}$, $z = \text{const.}$ or $\rho + z = \text{const.}$ We note this last case (oblique discontinuity) is particularly non-trivial, since our reconstruction to compute the numerical fluxes is one-dimensional at each stage (i.e. at each time step reconstruction is performed along lines of constant ρ and constant z independently).

In addition, convergence tests of smooth initial data have shown second order convergence (see Fig. 5.2), in regions of the computational domain removed from the extrema of the fluid variables. Due to the specifics of the reconstruction procedure explained in Sec. 4.3, the code is, as expected, only first order accurate in the vicinity of local extrema of the solution.

Still restricting to the case of flat spacetime, we have been able to evolve more complicated situations. One interesting scenario is the onset of a Kelvin-Helmholtz instability (Figs. 5.3 and 5.4). This type of instability occurs at a tangential discontinuity between two different states of a fluid (or two different fluids) which are sliding parallel to the discontinuity [54]. An example

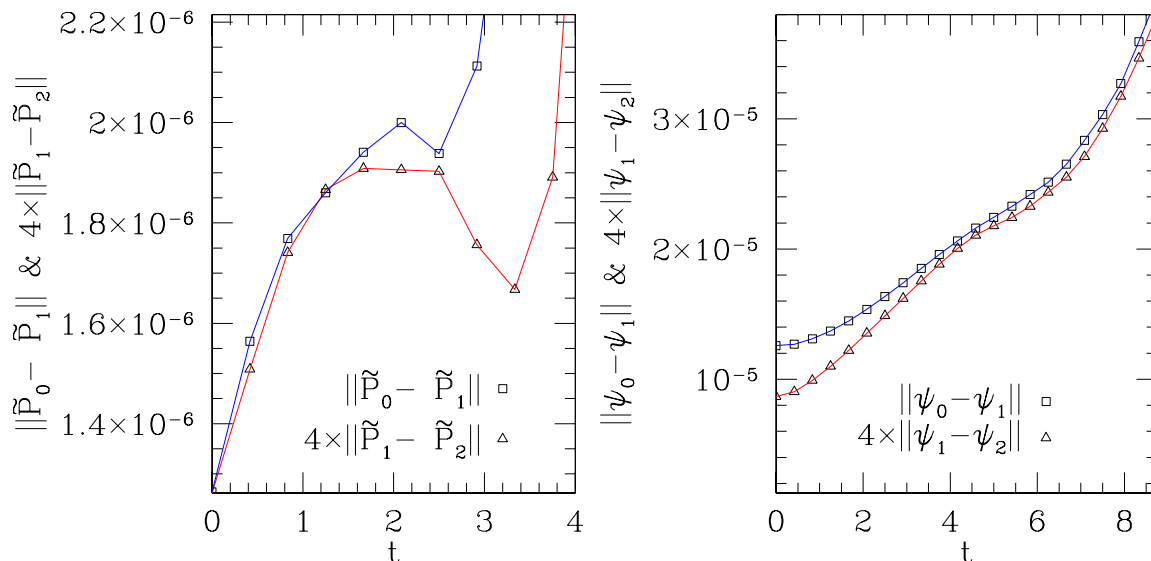


Figure 5.2: Here we show ℓ_2 norms of the estimated solution errors computed at two different levels of discretizations (mesh spacings $h_0 = 10/96$ and $h_1 = h_0/2 = 10/128$). Time development of the estimated errors is shown for the pressure, $\tilde{P}_{i+1/2j+1/2}$, on the left, and for the conformal factor, ψ_{ij} , on the right. The solution errors (at each level of discretization) are themselves computed via subtraction of values calculated using two discretization levels, i.e. as $f_k - f_{k+1}$, $k = 0, 1$, where f_k is the solution computed on a grid with cell spacing h_k , and $h_{k+1} = h_k/2$. For a second order scheme, these differences should be quadratic in the mesh spacing, h , as $h \rightarrow 0$, so that when we reduce the grid spacing by 2, the differences should decrease by roughly a factor of 4. Thus, we multiply the ℓ_2 norm of the finer-grid error estimate by 4 to show more explicitly that our code is second order convergent. We note that the results plotted here came from the evolutions described in more detail in Fig. 5.5 and accompanying text. We also note that at $t \sim 3$ the pressure becomes discontinuous and we can no longer expect $\tilde{P}_{i+1/2j+1/2}$ to be second order convergent. On the other hand, the conformal factor ostensibly remains second-order convergent throughout the evolution (only the early stages are depicted here), which is a manifestation of the facts that: (a) the constraint equation, being elliptic, tends to smooth discontinuities in its sources; and (b) (related) the gravitational field (particularly the spherical or monopole piece) tends to be responsive to extended, rather than localized, distributions of matter/energy. However, in principle, if we could go to the $h \rightarrow 0$ limit, we would necessarily find that the conformal factor would only be twice differentiable at the locations of shocks, and hence we would observe “loss of convergence” in the geometric variables as well.

of this effect is the generation of waves on the surface of a body of water due to the wind. In our case we have simulated the contact discontinuity (meaning that the pressure remains constant across the discontinuity) of two coaxial cylinders of fluid. The fluid in the inner cylinder is initially at rest with constant density D_I , while the fluid in the inner cylinder is initially moving with a uniform velocity in the z direction—parallel to the discontinuity—and has a constant density D_O , with $D_O < D_I$. (We have not simulated any situations where any of the fluid is rotating about the symmetry axis). In order to excite the instability, we deform the initial contact discontinuity, so that it has a small amount of curvature along the z -axis. Fig. 5.3 shows a schematic of the initial setup.

Fig. 5.4 shows snapshots, from simulations using the same initial data, but two different resolutions, during the evolution of the instability. For the specific case shown here, the initial speed of the fluid is $v = 1/2$. The initial data has been specified using a polytropic equation of state $P = K\rho_0^\Gamma$ (like the one used in 4.4.2), with $\Gamma = 3/2$ throughout the fluid, but with distinct values of K chosen for the two cylinders. The initial values of D in the inner and outer cylinders are $D_I = 1.0$ and $D_O = 0.115$ respectively. The limits of the computational domain are $\rho_{\max} = 20$, $z_{\min} = -z_{\max} = -10$, and the two discretizations used to generate the results shown in Fig. 5.4 are $\Delta\rho = \Delta z = 20/256$ (top figure) and $\Delta\rho = \Delta z = 20/512$ (bottom figure) (for these particular simulation we have *not* adopted the usual choice $\rho_{\max} = z_{\max}$, explained in Sec. 5.4.) Full MPEG animations of this simulation can be viewed at [109].

In the continuum limit, the fluid should become totally turbulent due to the lack of viscosity in our hydrodynamical equations of motion. In practice, there is effective *numerical* viscosity, due to the fact that the equations are always solved using a finite mesh spacing, but also since, as we have seen in the spherically symmetric calculations, the Roe numerical flux adds dissipation. We find, however, that as the discretization scale h is reduced, our simulations always tend to develop features all of the way down to the particular mesh size being used.

We have also performed some evolutions of the hydrodynamic equations fully coupled to gravity. Figs. 5.5 and 5.6 show results from the evolution of a weakly self-gravitating pulse of fluid. The initial conditions in this case are time symmetric with initial distributions of \tilde{D} and $\tilde{\tau}$ given by

$$\tilde{D}(0, \rho, z) = A_D \exp\left\{-\left[(\rho - 3)^2 + z^2\right]\right\}, \quad (5.94)$$

$$\tilde{\tau}(0, \rho, z) = A_\tau \exp\left\{-\left[(\rho - 3)^2 + z^2\right]\right\}, \quad (5.95)$$

with $A_D = 1.0 \times 10^{-2}$ and $A_\tau = 1.0 \times 10^{-2}$. This implies that the initial fluid distribution is toroidal in shape. For the runs described below, the computational domain had $\rho_{\max} = 10.0$, $z_{\max} = -z_{\min} = 10.0$, $N_\rho = 96$, $N_z = 192$, and we used an adiabatic index $\Gamma = 3/2$. The initial maximum value of the pressure is $\tilde{P}_0 = 4.97 \times 10^{-3}$. In Fig. 5.5 we can see that the

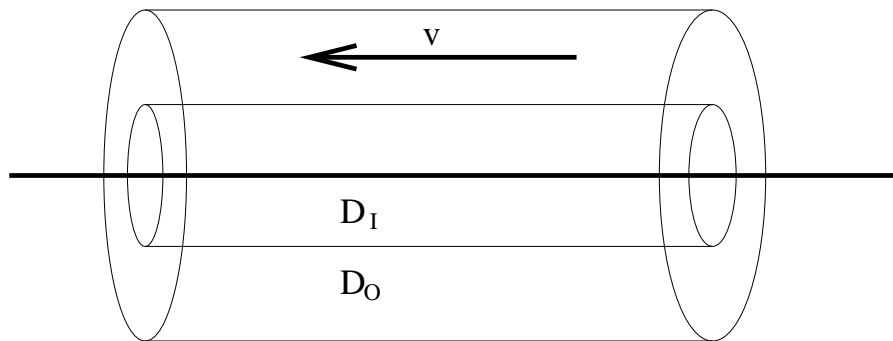


Figure 5.3: Geometry of the system used to study the Kelvin-Helmholtz instability. Initially, the system state describes two constant-density coaxial fluid cylinders, separated by a contact discontinuity. The inner, more dense cylinder (with $D = D_I$) of fluid starts at rest in the lab frame, while the outer, less dense cylinder (with $D = D_O$) has a uniform velocity in the z -direction v (along the axis of symmetry). Although not shown in this schematic, in order to trigger the instability the initial discontinuity is perturbed, and is thus *not* everywhere parallel to the z -axis (or, therefore, to the velocity of the fluid in the outer cylinder).

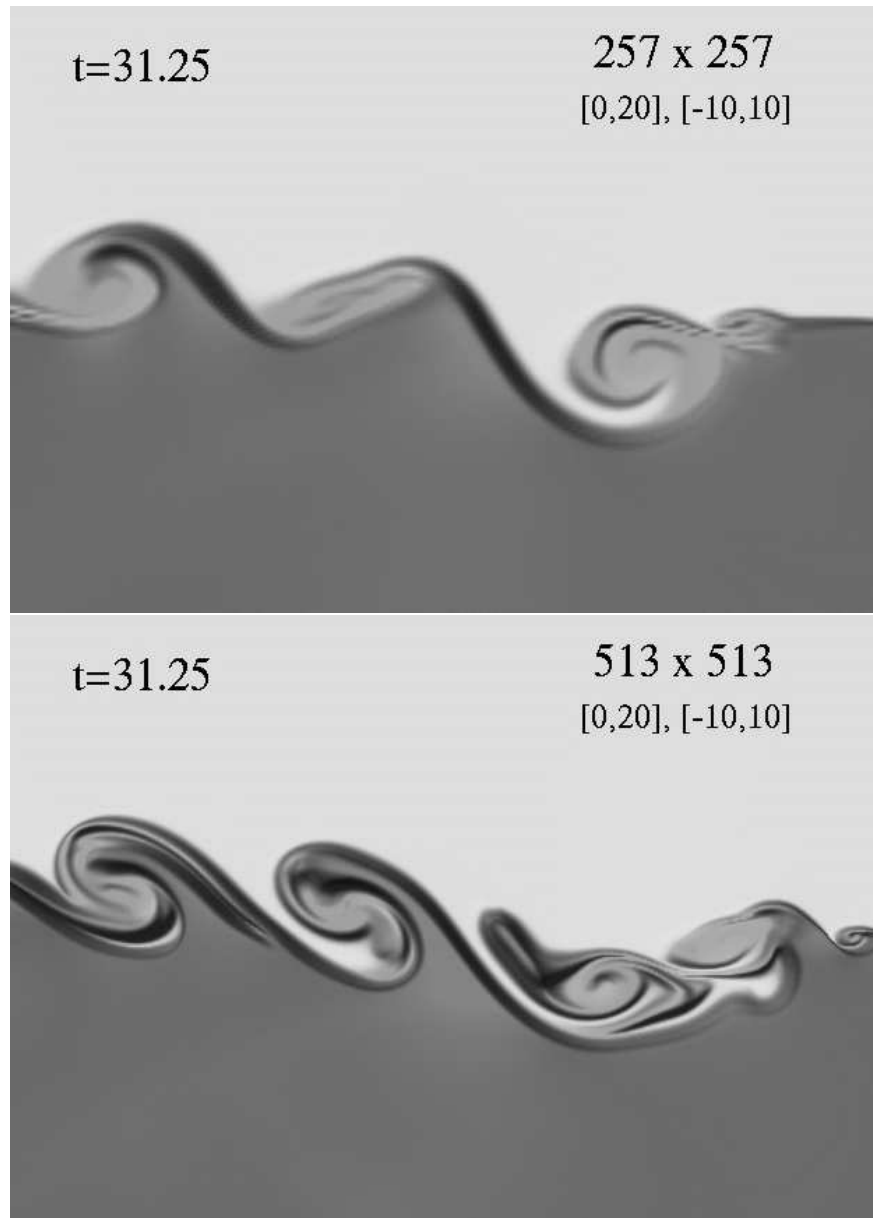


Figure 5.4: This figure shows $t = \text{const.}$ snapshots (zooming in close to the surface of discontinuity) from simulations of the Kelvin-Helmholtz instability discussed in the text, starting from the same initial conditions, but using two different resolutions: $h = \Delta r = \Delta z = 20/256$ (top) and $h = \Delta r = \Delta z = 20/512$ (bottom). Variations in the grey scale highlight regions with different values of D (white to black, low to high density). We can see how the dynamics is highly dependent on the cell spacing, h , which, among other things, sets the amount of numerical viscosity in the discrete equations.

pulse immediately begins to disperse due to hydrostatic pressure. A rough estimation of the force density due to hydrostatic pressure gives $\tilde{P}_0/\delta \approx 5 \times 10^{-3}$ where $\delta = 1$ is the width of the pulse given by (5.94) and (5.95). On the other hand the gravitational force can be estimated by $M\tilde{P}_0/((\Gamma - 1)\rho^2) \approx 8 \times 10^{-4}$ where the mass M is approximated using the spherical symmetric formula $M \approx 2(\psi_0 - 1)$, $\rho \approx 3$ is the position of the centre of the pulse and $\psi_0 \approx 1.1$ is the initial maximum of the conformal factor shown in Fig. 5.6. This calculation shows that the force due to hydrostatic pressure is about an order of magnitude more important than the gravitational force at the initial time.

The ingoing part of the fluid then propagates towards the axis and produces a shock wave—all the variables describing the fluid become discontinuous—that subsequently propagates outwards. For these initial conditions the fluid eventually completely disperses. Fig. 5.6 shows the evolution of the conformal factor from the same simulation. Note that the self-gravitation of the fluid remains very small throughout the evolution; for example, $\max_{t,\rho,z} \psi(t, \rho, z) \approx 1.1$, which is close to the Minkowskian value, $\psi \equiv 1.0$, and which is attained at $t = 0$.

In Fig. 5.7 we show another time-symmetric simulation, with initial profiles for \tilde{D} and $\tilde{\tau}$ again given by (5.94) and (5.95), but this time with $A_D = 5.0 \times 10^{-2}$ and $A_\tau = 5 \times 10^{-2}$, i.e. with initial amplitudes for the dynamical variables that are 5 times larger than for the weak field simulation just described ($\max_{\rho,z} \tilde{P}(0, \rho, z) = 2.5 \times 10^{-2}$).

Compared to the weak-field case, the evolution is now quite different. The first thing to notice is that, with respect to coordinate time, the fluid evolution unfolds more slowly. This is probably at least partly a coordinate effect, due to the spatio-temporal variation of the lapse function. For example, the minimum value of the lapse at the initial time is $\min_{\rho,z} \alpha(0, \rho, z) \approx 0.8$ while at the end of the evolution we have $\min_{\rho,z} \alpha(0, \rho, z) \approx 0.3$. The second thing that is apparent from Fig. 5.7 is the fact that the fluid pulse does *not* spread out due to its pressure in this case. Rather, the fluid is apparently compressed—producing a more compact configuration—and we believe that this is a direct consequence of the self-gravitational interaction. At late stages in the evolution, this concentrated configuration moves closer to the axis, again, probably due to gravitational self-interaction. Shortly after the time shown in the final frame of the figure, the solver for the primitive variables fails (produces unphysical values) and the evolution cannot proceed.

At the current time, the code is prone to numerical instabilities, tending to produce unphysical negative pressures and speeds > 1 in many situations. We believe that at least some of these problems are due to inadequate grid resolution. The maximum resolution that we can obtain is currently constrained by the memory size of the computers on which we run the simulations, as well as on the position of the outer boundaries of the computational domain. In particular, since the boundary conditions explained in Sec. 5.2.3 are only valid for large values of $r \sim \sqrt{\rho^2 + z^2}$, if we do

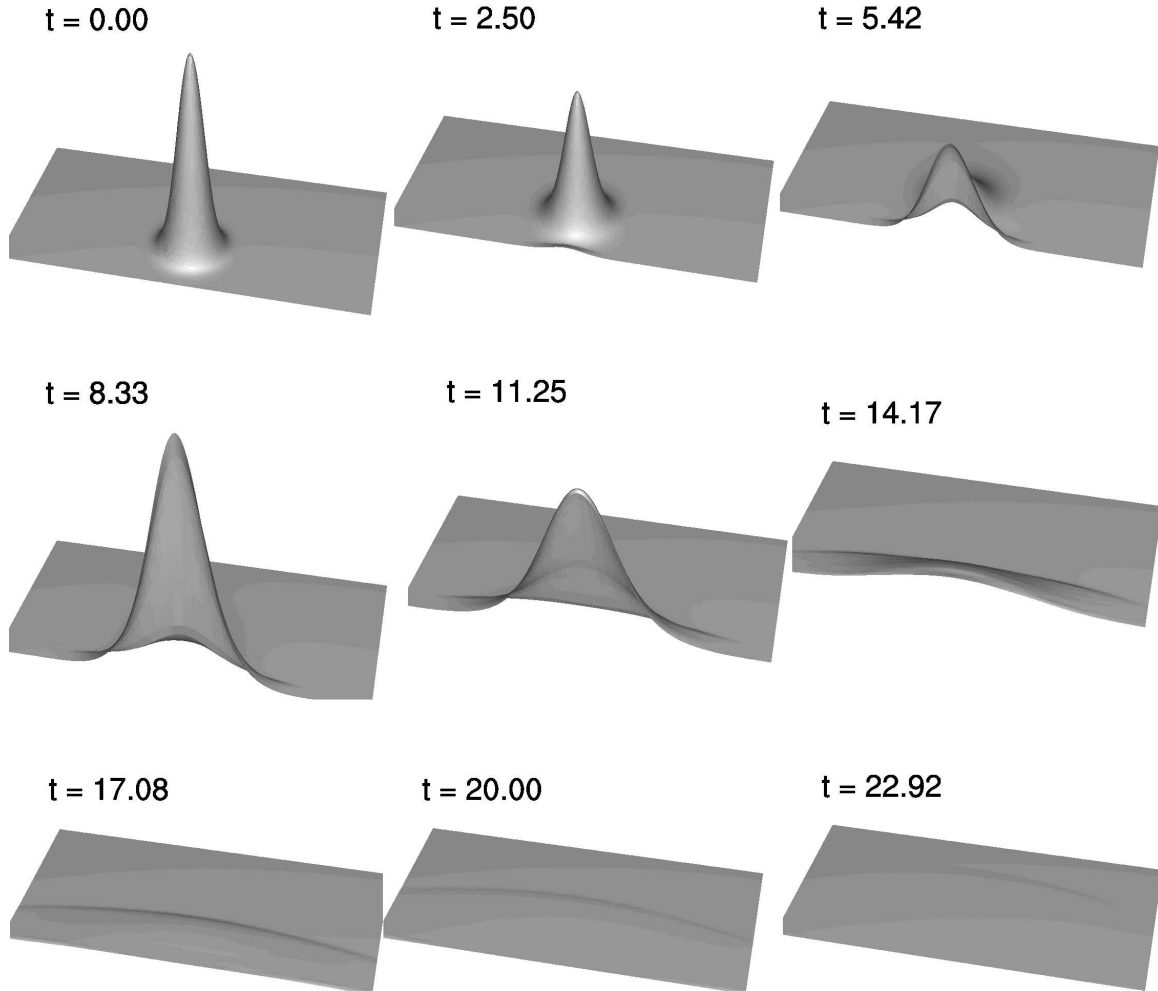


Figure 5.5: Time evolution of a weakly self-gravitating pulse of perfect fluid. Here, the initial conditions are time symmetric (i.e. zero initial velocity), with initial profiles for \tilde{D} and $\tilde{\tau}$ given by (5.94)-(5.95). The computational domain extends from $\rho_{\min} = 0$ to $\rho_{\max} = 10$ and from $z_{\min} = -10$ to $z_{\max} = 10$. The figure shows the time development of the pressure $\tilde{P}(t, \rho, z)$ (z axis roughly horizontal in the plots) which has an initial maximum amplitude $\tilde{P}_0 = 4.97 \times 10^{-3}$. The evolution shows how the pulse initially spreads out due to pressure forces. At $t \approx 5.0$, the ingoing part of the pulse reaches the axis of symmetry and subsequently “self-reflects”, producing a shock that marches outwards, and which is most clearly visible in the $t = 14.17$ and $t = 17.08$ frames.

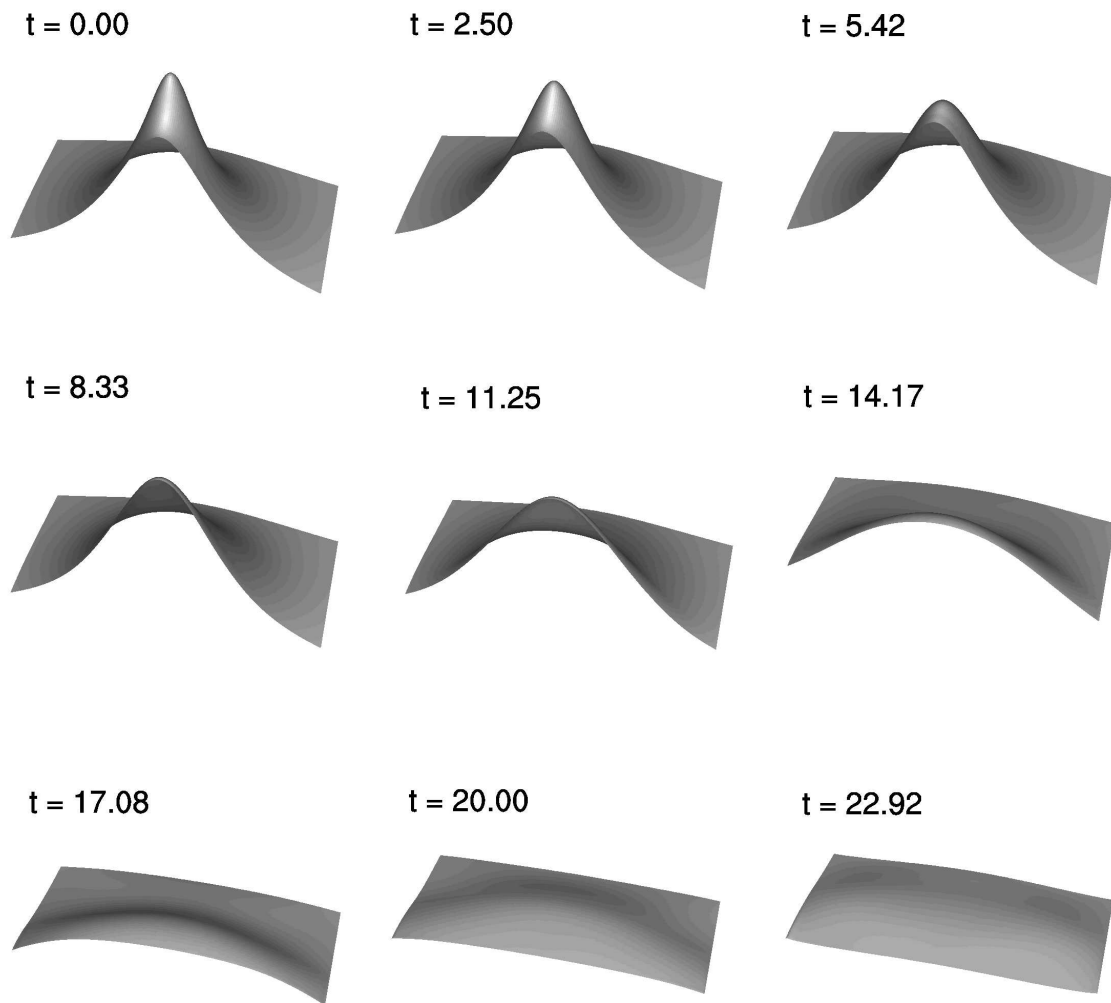


Figure 5.6: This figure shows the time evolution of the conformal factor $\psi(t, \rho, z)$ for the weakly self-gravitating pulse described in the text (see also Fig. 5.5). The maximal value, $\max_{t, \rho, z} \psi(t, \rho, z)$, is about 1.1 and occurs at the initial time. Note that towards the end of the evolution, when the fluid is dispersing to large distances, the conformal factor tends to its Minkowski value, $\psi = 1.0$.

not set the boundaries at large enough distances, we can also get unphysical results. For example the conformal factor, $\psi(r, t)$ may actually start growing, rather than falling off, as $r \rightarrow r_{\max}$.

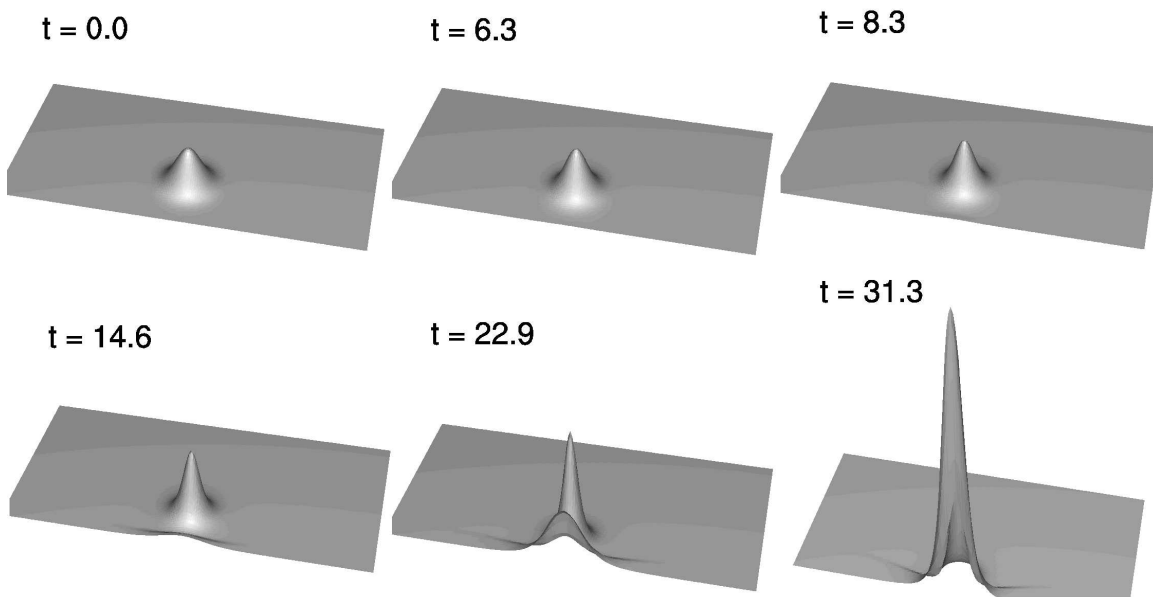


Figure 5.7: Evolution of a strongly self-gravitating pulse of fluid. Initial conditions are the same as that for the evolution showed in Figs. 5.5 and 5.6 but with amplitude parameters A_D and A_τ two orders of magnitude larger than in the weak-field case. Note that the vertical scale here is very different from that of Fig. 5.5; in particular, in this case, $\max_{\rho, z} \tilde{P}(0, \rho, z) = 2.5 \times 10^{-2}$. We can see how the pressure evolution in this case is very different than that in the weak field simulation. Here the dynamics is apparently dominated by gravity. Instead of dispersing due to its pressure, the fluid *compresses* as a result of its self-gravity. At later times the torus of fluid collapses towards the axis, and shortly thereafter the calculation of the primitive variables produces unphysical results, and the simulation must be stopped.

Despite our concerns about inadequate resolution, and the memory limitations we encounter at the current time when trying to compute at higher resolutions, we wish to stress that, ultimately, additional memory alone is very unlikely to solve the problems we face. For example, one specific long-term goal of this research is to study the critical gravitational collapse of perfect fluids in axisymmetry, including the case of rotating fluids. As explained in Sec. 1.2, In the corresponding spherically symmetric problem it was found that for certain choices of initial data families, the critical solutions are self-similar (see Evans and Coleman [29] and Neilsen and Choptuik for the study of the collapse of ultrarelativistic fluids, Hawke [46] for the collapse of the same type of

fluids in cosmological settings, and Noble [79] for the critical study of the collapse of perfect fluids and, in particular, critical behavior associated with TOV solutions). This strongly suggests that, in the axisymmetric case, evolution of similar types of initial data will also generate structures on all scales, accompanied by the development of large gradients in the dynamical variables. The only plausible way of attacking this problem in a computationally efficient manner is through the development of some sort of mesh refinement strategy to enable resolution to (locally) increase or decrease as necessary.

To that end, we have begun the development of a spherical symmetric code that refines the mesh adaptively as required. We are considering different possibilities for the mesh refinement criterion. One possibility is to use a Richardson-type estimate (i.e. calculating differences of solutions computed at resolutions h_k and $h_{k+1} = h_k/2$ as in the convergence tests discussed previously) for the truncation (solution) error; when this estimate exceeds a specified threshold we refine the mesh. This procedure has been used successfully by Hawke [46], in his study of relativistic fluids, and by LeVeque in [59]. On the other hand, due to the non-analyticity of the solutions (and the general non-smoothness of solutions computed using the HRSC methods employed in this thesis) these estimates are not very accurate and tend to be numerically irregular. This has motivated us to consider the correction to the numerical flux given by equation (4.56) as a measure of the need for refinement. Specifically when the following function:

$$\frac{1}{2} \sum |\lambda_\alpha| \omega_\alpha \boldsymbol{\eta}_\alpha \quad (5.96)$$

(the different quantities in the above expression are defined in Chap. 4) goes above threshold, we refine. Our current implementation uses a global time step, Δt , on all levels, fixed by the finest level of spatial refinement: $\Delta t = \lambda \Delta r_{\text{finest}}$. The global time-stepping procedure simplifies the treatment of internal boundaries between grids with different mesh spacings, relative to methods such as that proposed by Berger and Collela [6]. We also point out that we have found the use of ENO (Essentially Non Oscillatory) [15] interpolation crucial in our initialization of (new) fine grid values from coarse grid values.

We also plan to implement one or more approximations to the numerical flux, other than the Roe approximation described above. We are especially interested in seeing whether the use of an alternate solver helps with some of the strong-field problems that we have encountered in our collapse calculations. In particular, we are considering the use of the Marquina approximation [22] which has been compared with the Roe solver by Hawke [45]; Hawke found that the Marquina method almost always performed better than the Roe one. Another place for improvement is the reconstruction of the conservative variables at the cell interfaces, where we plan to implement interpolations other than minmod.

Finally, we have also tried to implement a finite-difference based algorithm to solve the equilibrium equations for rotating configurations, Sec. 5.3. Our first approach involved the use of multigrid methods of the type described in Sec. 5.4. However, because of our inability to set proper regularity conditions on the axis, this approach has not been successful. The fact that most of the codes developed to date to find rotating equilibrium configurations are based on some kind of pseudo-spectral method (see [97] and references within) has inspired us to adopt such a approach. With a spectral technique, regularity conditions can be satisfied by choosing a set of basis (expansion) functions with the appropriate regularity behavior. We plan on developing such an algorithm in the near future.

Chapter 6

Conclusions and Directions for Future Research

In this thesis we have considered three different problems in numerical relativity. In these projects we have studied self-gravitating dynamics of three distinct types of matter and/or energy: scalar fields; vacuum gravitational energy; and perfect fluids. In two of the chapters, namely Chap. 2 and 4, we studied systems of equations that, due to our restriction to spherical symmetry, were effectively 2-dimensional, i.e. where the dynamic variables depended on 1 spatial dimension as well as time. In Chap. 3 and 5, on the other hand, the problems were effectively 3-dimensional, with variables dependent on 2 spatial dimensions and time.

We also made use of 2 different formalisms that cast Einstein field equations in a form suitable for treatment as a Cauchy problem: the so called 3+1 approach and the 2+1+1 formalism.

In terms of the numerical analysis, we employed a variety of discretization techniques and solution algorithms in our studies. These included standard centred finite-difference approaches for PDEs of evolution type (scalar and gravitational fields), Godunov/finite-volume/HRSC techniques for the hydrodynamical evolution equations, and multigrid algorithms for the solution of discretized elliptic equations arising from the Einstein constraints.

In the remainder of this chapter we summarize our main conclusions. Firstly, in Sec. 6.1, we summarize the results of the collapse of scalar field with a particular potential, as described in Chap. 2. A summary of results from the evolution of a 5-D black string, which we discussed in Chap. 3 follows. Finally we conclude with some of our findings in relativistic hydro.

As a continuation of this thesis we plan to continue our numerical studies of the strong field regime in the coupled Einstein equations/hydrodynamical equations. Specifically we plan to incorporate adaptive mesh refinement into our axisymmetric code.

6.1 Scalar Field Collapse with Angular Momentum

In Chap. 2 we studied the critical collapse of a scalar field in spherical symmetry. In this collaborative effort [23], the equations of motion for a massless scalar field included a term that was characterized by an angular momentum parameter, l , and that could be viewed as providing an angular momentum barrier. The additional term is analogous to the angular momentum barrier in the 1-dimensional reduced mechanics problem of a particle moving in a central potential.

Following [17], we studied the threshold of black hole formation in our model through parameterization of the initial data with a single parameter, p . We found evidence for an entire family of critical solutions—one for each value of l —and, as was the case for the original study [17] (equivalent to the case $l = 0$), the threshold solutions were found to be discretely self-similar. The critical solutions were thus characterized by two different exponents: (1) Δ_l , which is the so-called echoing exponent, and which is actually a period when the solution is expressed in coordinates adapted to the scale-symmetry (self-similarity); and (2) a scaling exponent, γ_l , that describes how dimensionful quantities, such as the black hole mass, scale with parameter-space distance from criticality, $(p - p^*)$, as $p \rightarrow p^*$. We found that both exponents decreased with l in an almost exponential manner.

Moreover, we found that as l was increased, the time that a solution remained close to criticality (for fixed $(p - p^*)/p^*$) grew, and that the critical solutions appeared to approach periodic configurations. We believe that this fact can be understood as the angular momentum barrier having, at least partially, a stabilizing effect against gravitational collapse.

6.2 Instability of a Black String

Chap. 3 described a study of the dynamical instability of a particular 5-dimensional relative of the usual 4-dimensional Schwarzschild solution, namely the black string originally due to Myers and Perry [73]. This was another collaborative effort [18], and in order to study the instability we developed an effective 2+1 dimensional numerical relativity code to evolve the vacuum Einstein equations.

The exposition in Chap. 3 focused on our numerical procedure to solve the constraint equations at the initial time, and on our implementation of an algorithm to approximately locate event horizons via “backwards evolution” of null rays, using the full results from the numerical simulations of the spacetimes.

The results of our calculations were shown to agree with the predictions from perturbation theory due to Gregory and Laflamme [37]. In addition, we used our code to evolve perturbed

black-string spacetimes well beyond the linear regime where perturbation theory is valid. In the non-linear regime, we found evidence that the perturbed spacetime evolves to a configuration that resembles a series of black holes connected by a black string with radius smaller than the progenitor string. Due to the development of a coordinate pathology, our code failed at late times, and we were thus unable to make any statement about the ultimate fate of unstable black strings, particularly since at the time the code crashes, the spacetimes were still highly dynamical. We also observed that, at least for the spacetimes considered, our approximations for the location of the event horizon at any instant of time agreed well with the locations of apparent horizons.

6.3 Relativistic Hydrodynamics

In the final two chapters of this thesis, Chaps. 4 and 5, we described the development of codes to simulate, respectively, spherically symmetric, and axially symmetric, general relativistic hydrodynamics.

The spherically symmetric code was based on a 3+1 decomposition of the Einstein equations and used coordinates which are the natural restriction to spherical symmetry of the coordinates used in the axisymmetric simulations. This allowed us to experiment with formalisms and numerical methods in a simpler setting than that provided by the axisymmetric case. In order to evolve the hydrodynamic quantities, a numerical technique tailored to treat discontinuities stably and cleanly—namely a so-called high resolution shock capturing method—was implemented. Development of the code also led to the identification of a new set of conservative variables, whose use was crucial in making the solution of the Hamiltonian constraint in the model a well-posed problem. In addition, we observed that—at least at the resolutions used in our simulations—our algorithm was too dissipative to obtain long term evolution of stationary (TOV) solutions.

Chap. 5 considered the case of axisymmetric hydrodynamics. The equations of motion for the fluid and the geometry were written using the 2+1+1 formalism [34]. In addition, the fluid equations were expressed in conservation law form, which again permitted the use of high resolution shock capturing methods. We showed that our code converged (at least for the weak evolution shown in Fig. 5.6) as a function of mesh resolution as expected, and that it could stably evolve various configurations of discontinuous initial data. On the other hand, we found that the code was too unstable to permit study of the very strong-field regime, typified, for example, by configurations close to black hole formation. Additionally, as in the spherical case, we found that the algorithm used for the hydrodynamics was too dissipative to permit stable evolution of stars for long times.

In order to solve some of these problems we have started implementing a code which adaptively refines the numerical grid of points on the locations where it is required. Some early experiments

in spherical symmetry indicate that this is a promising approach.

Bibliography

- [1] Abrahams A. M. and C. R. Evans, “Critical Behavior and Scaling in Vacuum Axisymmetric Gravitational Collapse”, *Phys. Rev. Lett.* **70**, 2980 (1993).
- [2] Anderson E. *et al*, “LAPACK Users’ Guide”, Society for Industrial and Applied Mathematics, Philadelphia, (1992) http://www.netlib.org/lapack/lug/lapack_lug.html.
- [3] Arnowitt R., S. Deser and C. W. Misner, “The dynamics of general relativity”, in *Gravitation: An Introduction to Current Research*, Ed. L. Witten, J. Wiley & Sons, Inc., New York (1962).
- [4] Baiotti L. *et al*, “Three-dimensional relativistic simulations of rotating neutron star collapse to a Kerr black hole”, arXiv:gr-qc/0403029.
- [5] Baumgarte T. W., S. L. Shapiro, M. Shibata, “On the maximum mass of differentially rotating neutron stars”, *Astrophys. J.*, **528** L29, (2000).
- [6] Berger M. J., P. Collela, “Local adaptive mesh refinement for shock hydrodynamics”, *J. Comp. Phys.* **82**, 64-84, (1989).
- [7] Bogojevic A. R. and L. Perivolaropoulos, “Black Holes In A Periodic Universe”, *Mod. Phys. Lett. A* **6**, 369, (1991).
- [8] Bonazzola S., E. Gourgulhon, M. Salgado, and J. A. Marck, “Axisymmetric rotating relativistic bodies: a new numerical approach for “exact” solution”, *Astron. Astrophys.* **278**, 421-443, (1993).
- [9] Brandt A., “Multi-level Adaptive Solutions to Boundary-value Problems”, *Math. Comput.* **31**, 330, (1977).
- [10] Bruhat Y., “The Cauchy Problem”, in *Gravitation: An introduction to current Research*, Ed. L. Witten, J. Wiley & Sons, Inc., New York (1962).
- [11] CACTUS Computational Toolkit, The. <http://www.cactuscode.org>.
- [12] Caveny S. A., M. Anderson and R. A. Matzner, “Tracking Black Holes in Numerical Relativity”, *Phys. Rev. D* **68**, 104009, (2003) [arXiv:gr-qc/0303099].

-
- [13] Chandrasekhar S., *An introduction to the study of stellar structure*, University of Chicago Press, Chicago, (1939).
- [14] Chandrasekhar S., *The mathematical theory of black holes*, Oxford University Press, Oxford (1983).
- [15] Chi-Wang Shu, “Essentially non-oscillatory and weighted essentially non-oscillatory schemes for hyperbolic conservation laws”, Technical Report NASA CR-97-206253 ICASE Report No. 97-65, Institute for Computer Applications in Science and Engineering, November (1997).
- [16] Choptuik M. W., “Consistency of finite-difference solutions of Einstein’s equations”, *Phys. Rev. D* **44**, 3124-3135, (1991).
- [17] Choptuik M. W., “Universality And Scaling In Gravitational Collapse of a Massless Scalar Field”, *Phys. Rev. Lett.* **70**, 9, (1993).
- [18] Choptuik M. W., L. Lehner, I. Olabarrieta, R. Petryk, F. Pretorius and H. Villegas, “Towards the final fate of an unstable black string”, *Phys. Rev. D* **68**, 044001, (2003) [arXiv:gr-qc/0304085].
- [19] Choptuik M. W., E. W. Hirschmann, S. L. Liebling, and F. Pretorius, “An Axisymmetric Gravitational Collapse Code”, *Class. Quant. Grav.* **20**, 1857, (2003).
- [20] Choptuik M. W., E. W. Hirschmann, S. L. Liebling and F. Pretorius, “Critical collapse of the massless scalar field in axisymmetry”, *Phys. Rev. D* **68**, 044007, (2003) [arXiv:gr-qc/0305003].
- [21] Choptuik M. W., E. W. Hirschmann, S. L. Liebling and F. Pretorius, “Critical collapse of a complex scalar field with angular momentum”, arXiv:gr-qc/0405101.
- [22] Donat R., and A. Marquina, “Capturing Shock Reflections: An Improved Flux Formula”, *J. Comput. Phys.* **125**, 42-58, (1996).
- [23] Choptuik M. W., I. Olabarrieta, W. Unruh, J. Ventrella (in preparation).
- [24] Christodoulou D., “The problem of a self-gravitating scalar field”, *Commun. Math. Phys.* **105**, 337-361, (1986).
- [25] Christodoulou D., “A mathematical theory of gravitational collapse”, *Commun. Math. Phys.* **109**, 613-647, (1987).
- [26] Eckart A. and R. Genzel, “Stellar Proper Motions In The Central 0.1 Pc Of The Galaxy”, *Mon. Not. Roy. Astron. Soc.* **284**, 576, (1997).

-
- [28] Evans C. R. “A method for numerical relativity: Simulation of axisymmetric gravitational collapse and gravitational radiation generation”, Ph.D. Thesis, The University of Texas at Austin, (unpublished), (1984).
- [28] Evans C. R., “An Approach For Calculating Axisymmetric Gravitational Collapse”, Gravitational Radiation. in J. Centrella ed. *Dynamical Spacetimes and Numerical Relativity*, 3-39, Cambridge, England, Cambridge University Press, (1986).
- [29] Evans C. R., and J. S. Coleman, “Observation of critical phenomena and selfsimilarity in the gravitational collapse of radiation fluid,” *Phys. Rev. Lett.* **72**, 1782 (1994) [arXiv:gr-qc/9402041].
- [30] Font J. A., “Numerical hydrodynamics in general relativity”, *Living Rev. Rel.* **3**, 2, (2000) [*Living Rev. Rel.* **6**, 4, (2003)] [arXiv:gr-qc/0003101].
- [31] Font J. A., M. Miller, W.-M. Suen and M. Tobias, “Three Dimensional Numerical General Relativistic Hydrodynamics: Formulations, Methods and Code Tests”, *Phys. Rev. D* **61**, 044011, (2000).
- [32] Garfinkle D. and G. C. Duncan, “Scaling of curvature in sub-critical gravitational collapse”, *Phys. Rev. D* **58**, 064024, (1998) [arXiv:gr-qc/9802061].
- [33] Garfinkle D., C. Gundlach and J. M. Martin-Garcia, “Angular momentum near the black hole threshold in scalar field collapse”, *Phys. Rev. D* **59**, 104012, (1999) [arXiv:gr-qc/9811004].
- [34] Geroch R., “A Method for Generating Solutions of Einstein’s Equations”, *J. Math. Phys.* **12**, 918-924, (1971).
- [35] Ghez A. M., B. L. Klein, M. Morris and E. E. Becklin, “High Proper Motion Stars in the Vicinity of Sgr A*: Evidence for a Supermassive Black Hole at the Center of Our Galaxy”, *Astrophys. J.* **509**, 678, (1998) [arXiv:astro-ph/9807210].
- [36] Godunov S. K., *Mat. Sb.* **47**, 271, (1959).
- [37] Gregory R. and R. Laflamme, “Black Strings And P-Branes Are Unstable”, *Phys. Rev. Lett.* **70**, 2837, (1993) [arXiv:hep-th/9301052].
- [38] Gregory R. and R. Laflamme, “The Instability of charged black strings and p-branes”, *Nucl. Phys. B* **428**, 399, (1994) [arXiv:hep-th/9404071].
- [39] Gubser S. S., “On non-uniform black branes”, *Class. Quant. Grav.* **19**, 4825, (2002) [arXiv:hep-th/0110193].

-
- [40] Gundlach C., “Understanding Critical Collapse of a scalar field”, *Phys. Rev. D* **55**, 695-713, (1997) [arXiv:gr-qc/9604019].
- [41] Gundlach C., “Angular momentum at the black hole threshold”, *Phys. Rev. D* **57**, 7080, (1998) [arXiv:gr-qc/9711079].
- [42] Gundlach C., “Critical gravitational collapse of a perfect fluid with $p = k\rho$: Nonspherical perturbations”, *Phys. Rev. D* **65**, 084021, (2002) [arXiv:gr-qc/9906124].
- [43] Gundlach C., “Critical phenomena in gravitational collapse”, *Phys. Rept.* **376**, 339, (2003) [arXiv:gr-qc/0210101].
- [44] Harrison B. K., K. S. Thorne, M. Wakano, and J. A. Wheeler, “Gravitation Theory and Gravitational Collapse”, University of Chicago Press, Chicago Illinois (1965).
- [45] Hawke I., “Computational Ultrarelativistic Hydrodynamics”, Ph.D. Thesis, Queen’s College, Cambridge, (unpublished), (2001).
- [46] Hawke I. and J. M. Stewart, “The Dynamics Of Primordial Black Hole Formation”, *Class. Quant. Grav.* **19**, 3687, (2002).
- [47] Hawking S. W., and G. F. R. Ellis, “The large scale structure of space-time”, Cambridge University Press, Cambridge, (1973).
- [48] Horowitz G. T. and K. Maeda, “Fate of the black string instability”, *Phys. Rev. Lett.* **87**, 131301, (2001) [arXiv:hep-th/0105111].
- [49] Hughes S. A, C. R. Keeton, P. Walker, K. T. Walsh, S. L. Shapiro and S. A. Teukolsky, “Finding black holes in numerical space-times”, *Phys. Rev. D* **49**, 4004, (1994).
- [50] Husa S., C. Lechner, M. Purrer, J. Thornburg and P. C. Aichelburg, “Type II critical collapse of a self-gravitating nonlinear sigma-model”, *Phys. Rev. D* **62**, 104007, (2000) [arXiv:gr-qc/0002067].
- [51] Kelly B., P. Laguna, K. Lockitch, J. Pullin, E. Schnetter, D. Shoemaker and M. Tiglio, “A cure for unstable numerical evolutions of single black holes: adjusting the standard ADM equations”, *Phys. Rev. D* **64**, 084013, (2001) [arXiv:gr-qc/0103099].
- [52] Kreiss H. and J. Olinger, “Methods for the Approximate Solution of Time Dependent Problems”, *Global Atmospheric Research Programme, Publications Series No. 10.* (1973).

-
- [53] Koike T., T. Hara and S. Adachi, “Critical behavior in gravitational collapse of radiation fluid: A Renormalization group (linear perturbation) analysis”, *Phys. Rev. Lett.* **74**, 5170 (1995) [arXiv:gr-qc/9503007].
- [54] Landau L. D. and E. M. Lifshitz, *Fluid Mechanics*, Pergamon Press, London, (1959).
- [55] Lehner L., M. Huq and D. Garrison, “Causal Differencing In ADM and Conformal ADM Formulations: A Comparison In Spherical Symmetry”, *Phys. Rev. D* **62**, 084016, (2000).
- [56] Lehner L., “Numerical relativity: A review”, *Class. Quant. Grav.* **18**, R25, (2001) [arXiv:gr-qc/0106072].
- [57] LeVeque R. J., *Numerical Methods for Conservation Laws*, Basel, Birkhauser-Verlag (1990).
- [58] LeVeque R. J., *Finite Volume Methods for Hyperbolic Problems*, New York, Cambridge University Press (2002).
- [59] LeVeque, R. J., “CLAWPACK Version 4.2 User’s Guide”, (2003).
- [60] Libson J., J. Masso, E. Seidel, W. M. Suen and P. Walker, “Event horizons in numerical relativity. 1: Methods and tests”, *Phys. Rev. D* **53**, 4335, (1996) [arXiv:gr-qc/9412068].
- [61] Liebling S. L., “Critical phenomena inside global monopoles”, *Phys. Rev. D* **60**, 061502, (1999) [arXiv:gr-qc/9904077].
- [62] Liebling S. L., “The singularity threshold of the nonlinear sigma model using 3D adaptive mesh refinement”, *Phys. Rev. D* **66**, 041703, (2002) [arXiv:gr-qc/0202093].
- [63] Maeda K., M. Sasaki, T. Nakamura, S. Miyama, “A new formalism of the Einstein Equations for Relativistic Rotating Systems”, *Prog. Theor. Phys.* **63**, 719-721, (1979).
- [64] Maple 8, Waterloo Maple Inc.
- [65] Marsa R. L. and M. W. Choptuik, “The RNPL User’s Guide”, http://laplace.physics.ubc.ca/Members/marsa/rnpl/users_guide/users_guide.html (1995).
- [66] Martí J. M., J. M. Ibáñez, and E. Muller, “Numerical Relativistic Hydrodynamics: Local Characteristic Approach”, *Phys. Rev. D* **43**, 3794-3801, (1991).
- [67] Martí J. M., and E. Mueller, “Numerical hydrodynamics in special relativity”, *Living Rev. Rel.* **2**, 3, (1999) [arXiv:astro-ph/9906333].
- [68] May M. M, and R. H. White, “Hydrodynamic calculations of general relativistic collapse”, *Phys. Rev. D* **141**, 1232-1241, (1966).

-
- [69] May M. M, and R. H. White, “Stellar dynamics and gravitational collapse”, *Methods Comput. Phys.* **7**, 219-258, (1967).
- [70] Miralles J. A., J. M. Ibáñez, J. M. Martí, and A. Pérez, “Incompressibility of hot nuclear matter, general relativistic stellar collapse and shock propagation”, *Astron. Astrophys. Suppl.* **90**, 283-299, (1991).
- [71] Misner C. W., K. S. Thorne and J. A. Wheeler, *Gravitation*, New York, W.H. Freeman and Company (1973).
- [72] Müller I. “Speeds of Propagation in Classical and Relativistic Extended Thermodynamics”, *Living Rev. Rel.* **2**, 1, (1999).
- [73] Myers R. C. and M. J. Perry, “Black Holes In Higher Dimensional Space-Times”, *Annals Phys.* **172**, 304, (1986).
- [74] Nakamura T, “General Relativistic Collapse of Axially Symmetric Stars Leading to the Formation of Rotating Black Holes”, *Prog. Theo. Phys.* **65**, (1981).
- [75] Nakamura T., and H. Sato, “General Relativistic Collapse of Non-Rotating, Axisymmetric Stars”, *Prog. Theor. Phys.* **67**, 1396-1405, (1982).
- [76] Nakamura T., K. Oohara and Y. Kojima, “General Relativistic Collapse of Axially Symmetric Stars and 3D Evolution of Pure Gravitational Waves”, *Prog. Theor. Phys. Suppl.* **90**, 13-101, (1987).
- [77] Neilsen D. W., “Extremely Relativistic Fluids in Strong-Field Gravity”, Ph.D. Thesis, The University of Texas at Austin, (unpublished), (1999).
- [78] Neilsen D. W. and M. W. Choptuik, “Ultrarelativistic Fluid Dynamics”, *Class. Quantum Grav.* **17**, 733-759, (2000) [arXiv:gr-qc/9904052].
- [79] Noble S. C., “A Numerical Study of Relativistic Fluid Collapse”, arXiv:gr-qc/0310116. Ph.D. Thesis, The University of Texas at Austin, (unpublished), (2003).
- [80] Oppenheimer J. R., and G. M. Volkoff, “On Massive Neutron Cores”, *Phys. Rev.* **55**, 374-381, (1939).
- [81] Olabarrieta I., and M. W. Choptuik, “Critical phenomena at the threshold of black hole formation for collisionless matter in spherical symmetry”, *Phys. Rev. D* **65**, 024007, (2002) [arXiv:gr-qc/0107076].

-
- [82] Orosz J. A., “Inventory of Black Hole Binaries”, [arXiv:astro-ph/0209041].
- [83] Overduin J. M. and P. S. Wesson, “Kaluza-Klein gravity”, *Phys. Rept.* **283**, 303, (1997) [arXiv:gr-qc/9805018].
- [84] Petzold L. R. and A. C. Hindmarsh, “LSODA”, Computing and Mathematics Research Division, I-316 Lawrence Livermore National Laboratory, Livermore, CA 94550.
- [85] Piran T. and R. F. Stark, “Numerical Relativity, Rotating Gravitational Collapse and Gravitational Radiation”, in J. Centrella ed. *Dynamical Spacetimes and Numerical Relativity*, 40-73, Cambridge, England, Cambridge University Press, (1986).
- [86] Press W. H., S. A. Teukolsky, W. T. Vetterling, and B. P. Flannery, “Numerical Recipes in Fortran 77”, (2nd edition), Cambridge University Press, New York (1992).
- [87] Pretorius F., “Numerical Simulations of Gravitational Collapse”, Ph.D. Thesis, The University of British Columbia, (unpublished), (2002).
- [88] Rein G., A. D. Rendall and J. Schaeffer, “Critical collapse of collisionless matter: A numerical investigation”, *Phys. Rev. D* **58**, 044007, (1998) [arXiv:gr-qc/9804040].
- [89] Rhoades C. E. and R. Ruffini, “Maximum Mass of a Neutron Star”, *Phys. Rev. Lett.* **32**, 324-327, (1974).
- [90] Roe P. L., “Approximate Riemann solvers, parameter vectors and difference schemes”, *J. Comput. Phys.* **42**, 357-372, (1981).
- [91] Romero, J. V. J. M. Ibáñez, J. M. Martí, J. A. Miralles, “A New Spherically Symmetric General Relativistic Hydrodynamical Code”, *Astrophys. J.* **462**, 839-854, (1996) [arXiv:astro-ph/9509121].
- [92] Sasaki M., K. Maeda, S. Miyama, T. Nakamura, “A Method of Determining Apparent Horizons in $[(2+1)+1]$ -Formalism of the Einstein Equations”, *Prog. Theor. Phys.* **63**, 1051-1053, (1980).
- [93] Seidel E., and W. M. Suen, “Towards a singularity-proof scheme in numerical relativity”, *Phys. Rev. Lett.* **69**, 1845-1848, (1992).
- [94] Shapiro S. L. and S. A. Teukolsky, “*Black Holes, White Dwarfs, and Neutron Stars*”, J. Wiley & Sons, Inc., New York (1983).
- [95] Shibata M., “Axisymmetric Simulations of Rotating Stellar Collapse in Full General Relativity”, *Prog. Theor. Phys.* **104**, 325-358, (2000).

-
- [96] Shinkai H. A. and G. Yoneda, “Adjusted ADM systems and their expected stability properties”, *Class. Quant. Grav.* **19**, 1027, (2002) [arXiv:gr-qc/0110008].
- [97] Stergioulas N., “Rotating stars in relativity”, *Living Rev. Rel.* **6**, 3, (2003) [arXiv:gr-qc/0302034].
- [98] Swesty D., J. M. Lattimer, and E. S. Myra, “The role of the equation of state in the ‘prompt’ phase of type II supernovae”, *Astrophys. J.* **425**, 195-204, (1994).
- [99] Synge, J. L., *The relativistic gas*, Noth-Holland, Amsterdam, (1957).
- [100] Teukolsky S. A., “On the Stability of the Iterated Crank-Nicholson Method in Numerical Relativity”, *Phys. Rev. D* **61**, 087501, (2000) [arXiv:gr-qc/9909026].
- [101] Thornburg J., “Coordinates and boundary conditions for the general relativistic initial data problem”, *Class. Quant. Grav.* **4**, 1119-1131, (1987).
- [102] Tolman R. C., *Relativity, Thermodynamics and Cosmology*, Oxford University Press, (1939).
- [103] Tolman R. C., “Static Solutions of Einstein’s Field Equations for Spheres of Fluid”, *Phys. Rev.* **55**, 364-373, (1939).
- [104] Unruh W., and R. Wald, (in preparation).
- [105] Van der Marel R. P., “Intermediate-Mass Black Holes in the Universe? - A Review of Formation Theories and Observational Constraints”, arXiv:astro-ph/0302101.
- [106] Van Leer B. J., “Towards the conservative difference scheme. V. A second order sequel to Godunov’s method”, *J. Comput. Phys.* **32**, 101-136, (1979).
- [107] Ventrella J. F. and M. W. Choptuik, “Critical phenomena in the Einstein-massless-Dirac system”, *Phys. Rev. D* **68**, 044020 (2003) [arXiv:gr-qc/0304007].
- [108] VonNeumann J., and R. D. Richtmyer, “A method for the numerical calculation of hydrodynamic shocks”, *J. Appl. Phys.* **21**, 232-247, (1950).
- [109] <http://laplace.physics.ubc.ca/People/inaki/fluids.html>
- [110] Weinberg S., *Gravitation and cosmology*, J. Wiley & Sons, Inc., New York (1972).
- [111] Wilson J. R. “Numerical Study of Fluid Flow in Kerr Space”, *Astrophys. J.* **173**, 209-219, (1971).

-
- [112] Wilson J. R. “A numerical Method for Relativistic Hydrodynamics”, in L. Smarr ed. *Sources of Gravitational Radiation*. 423-445, Cambridge, England, Cambridge University Press, (1979).
- [113] Wilson J. R., G. J. Mathews, and P. Marronetti, “Relativistic Numerical Model for Close Neutron Star Binaries”, *Phys. Rev. D* **54**, 1317-1331, (1996).
- [114] Wiseman T., “From black strings to black holes”, *Class. Quant. Grav.* **20**, 1177, (2003) [arXiv:hep-th/0211028].
- [115] York J. W. Jr., “Kinematics and Dynamics of General Relativity”, in *Sources of Gravitational Radiation*, Ed. L. Smarr, Seattle, Cambridge University Press (1979).
- [116] York J. W., T. Piran, “The Initial Value Problem and Beyond”, in *Spacetime and Geometry*, ed. by R. Matzner and L. C. Shepley, UT Press, Austin, (1982).

Appendix A

Hydrodynamic equations in conservation form

The general relativistic hydrodynamic equations can be cast in conservation law form. This fact was first fully exploited in the work of Martíand Muller [66] (also see [30] for a review), who developed what is now known as the Valencia formulation. Here we explicitly show the details of the calculation that puts the fluid equations into such a form. Specifically, our goal is to show that (1.36) and (1.37) can be written as

$$\frac{\partial Q_i}{\partial t} + \frac{\partial F^j_i}{\partial x^j} = S_i, \quad (\text{A.1})$$

where the S_i do not contain any derivatives of the fluid variables.

We begin with (1.36)

$$(T^\mu_\nu)_{;\mu} = 0, \quad (\text{A.2})$$

and then perform the following manipulations:

$$\begin{aligned} (g_{\delta\nu} T^{\mu\delta})_{;\mu} &= T^{\mu\delta} g_{\delta\nu;\mu} + g_{\delta\nu} T^{\mu\delta}_{;\mu} \\ &= g_{\delta\nu} \left[\frac{1}{\sqrt{-g}} (\sqrt{-g} T^{\mu\delta})_{,\mu} + \Gamma^\delta_{\mu\lambda} T^{\mu\lambda} \right] \\ &= g_{\delta\nu} \left[\frac{1}{\sqrt{-g}} (\sqrt{-g} g^{\xi\delta} T^\mu_\xi)_{,\mu} + \Gamma^\delta_{\mu\lambda} T^{\mu\lambda} \right] \\ &= g_{\delta\nu} \left[g^{\xi\delta}_{,\mu} T^\mu_\xi + g^{\xi\delta} \frac{1}{\sqrt{-g}} (\sqrt{-g} T^\mu_\xi)_{,\mu} + \Gamma^\delta_{\mu\lambda} T^{\mu\lambda} \right] = 0. \end{aligned} \quad (\text{A.3})$$

In the above, we have used equation (4.7.9) of [110] to go from the first to the second line and the Leibniz rule elsewhere. Also note that g is the determinant of the metric $g_{\mu\nu}$. Expression (A.3) can be written as:

$$\frac{1}{\sqrt{-g}} (\sqrt{-g} T^\mu_\nu)_{,\mu} = g_{\lambda\nu,\mu} T^{\mu\nu} - \Gamma^\delta_{\mu\lambda} T^{\mu\lambda} g_{\delta\nu}. \quad (\text{A.4})$$

This set of equations is thus in the form (A.1) since the stress tensor for a perfect fluid does not contain any derivatives of the fluid variables. The equation of particle number conservation (1.37)

is even simpler to massage into conservation form. Indeed

$$(J^\mu)_{;\mu} = 0, \tag{A.5}$$

can be written as

$$\frac{1}{\sqrt{-g}} (\sqrt{-g} J^\mu)_{,\mu} = 0, \tag{A.6}$$

using equation (4.7.7) of [110], and this is also of the desired form.

Appendix B

Scalar fields considered in the $l=1$ case

For illustrative purposes, in this Appendix we explicitly display the scalar fields $\Psi_l^m(t, r, \theta, \phi)$ that are considered in the calculations described in Chap. 2, for the specific case $l = 1$. Note that we want to consider *real* eigenfunctions of the L^2 operator. Moreover, all of the fields Ψ_l^m are required to have the same functional dependence on t and r , which we denote $\psi(t, r)$. We then have the following 3 fields:

$$\Psi_1^1 = \psi(t, r) Y_1^0(\theta, \phi) = \psi(t, r) \sqrt{\frac{3}{4\pi}} \cos(\theta), \quad (\text{B.1})$$

$$\Psi_1^2 = \frac{i}{\sqrt{2}} \psi(t, r) [Y_1^1(\theta, \phi) + Y_1^{-1}(\theta, \phi)] = \psi(t, r) \sqrt{\frac{3}{4\pi}} \sin(\theta) \sin(\phi), \quad (\text{B.2})$$

$$\Psi_1^3 = \frac{1}{\sqrt{2}} \psi(t, r) [Y_1^1(\theta, \phi) - Y_1^{-1}(\theta, \phi)] = \psi(t, r) \sqrt{\frac{3}{4\pi}} \sin(\theta) \cos(\phi), \quad (\text{B.3})$$

where $Y_l^s(\theta, \phi)$ denotes the usual spherical harmonic of degree l and order s . The equations of motion for $\psi(t, r)$ can then be derived by taking the divergence of the stress-energy tensor $\mathcal{T}_{ab}^{(l=1)}$ which in this case is:

$$\mathcal{T}_{ab}^{(l=1)} = T_{ab}^{(11)} + T_{ab}^{(12)} + T_{ab}^{(13)}. \quad (\text{B.4})$$

where each of the $T_{ab}^{(1m)}$ is computed using equation (2.3). Specifically, we have

$$T_{tt}^{(11)} = \frac{3}{8\pi} \alpha^2 \left[\frac{(\Pi^2 + \Phi^2) \cos(\theta)^2}{a^2} + \frac{\psi^2 \sin(\theta)^2}{r^2} \right], \quad (\text{B.5})$$

$$T_{tr}^{(11)} = \frac{3}{4\pi} \frac{\alpha \Pi \Phi \cos(\theta)^2}{a}, \quad (\text{B.6})$$

$$T_{t\theta}^{(11)} = -\frac{3}{4\pi} \frac{\alpha \Pi \psi \cos(\theta) \sin(\theta)}{a}, \quad (\text{B.7})$$

$$T_{t\phi}^{(11)} = 0, \quad (\text{B.8})$$

$$T_{rr}^{(11)} = \frac{3}{8\pi} \left[(\Pi^2 + \Phi^2) \cos(\theta)^2 - \frac{\psi^2 a^2 \sin(\theta)^2}{r^2} \right], \quad (\text{B.9})$$

$$T_{r\theta}^{(11)} = -\frac{3}{4\pi} \Phi \psi \cos(\theta) \sin(\theta), \quad (\text{B.10})$$

$$T_{r\phi}^{(11)} = 0, \quad (\text{B.11})$$

$$T_{\theta\theta}^{(11)} = \frac{3}{8\pi} \left[\frac{(\Pi^2 - \Phi^2) r^2 \cos(\theta)^2}{a^2} - \psi^2 \sin(\theta)^2 \right], \quad (\text{B.12})$$

$$T_{\theta\phi}^{(11)} = 0, \quad (\text{B.13})$$

$$T_{\phi\phi}^{(11)} = \frac{3}{8\pi} \sin(\theta)^2 \left[\frac{(\Pi^2 - \Phi^2) r^2 \cos(\theta)^2}{a^2} - \psi^2 \sin(\theta)^2 \right]. \quad (\text{B.14})$$

$$T_{tt}^{(12)} = \frac{3}{8\pi} \frac{\alpha^2 (-r^2\Pi^2 + r^2\Pi^2 \cos(\phi)^2 - r^2\Phi^2 + r^2\Phi^2 \cos(\phi)^2 + \psi^2 a^2 - \psi^2 \cos(\phi)^2 a^2) \cos(\theta)^2}{a^2 r^2} + \frac{3}{8\pi} \frac{\alpha^2 (r^2\Pi^2 - r^2\Pi^2 \cos(\phi)^2 + r^2\Phi^2 - r^2\Phi^2 \cos(\phi)^2 + \psi^2 \cos(\phi)^2 a^2)}{a^2 r^2}, \quad (\text{B.15})$$

$$T_{tr}^{(12)} = \frac{3}{4\pi} \frac{\alpha\Pi (-1 + \cos(\phi)^2) \Phi \cos(\theta)^2}{a} - \frac{3}{4\pi} \frac{\alpha\Pi (-1 + \cos(\phi)^2) \Phi}{a}, \quad (\text{B.16})$$

$$T_{t\theta}^{(12)} = -\frac{3}{4\pi} \frac{\alpha\Pi (-1 + \cos(\phi)^2) \sin(\theta) \psi \cos(\theta)}{a}, \quad (\text{B.17})$$

$$T_{t\phi}^{(12)} = -\frac{3}{4\pi} \frac{\alpha\Pi \sin(\phi) \psi \cos(\phi) \cos(\theta)^2}{a} + \frac{3}{4\pi} \frac{\alpha\Pi \sin(\phi) \psi \cos(\phi)}{a}, \quad (\text{B.18})$$

$$T_{rr}^{(12)} = \frac{3}{8\pi} \frac{(-r^2\Phi^2 + r^2\Phi^2 \cos(\phi)^2 - r^2\Pi^2 + r^2\Pi^2 \cos(\phi)^2 - \psi^2 a^2 + \psi^2 \cos(\phi)^2 a^2) \cos(\theta)^2}{r^2} + \frac{3}{8\pi} \frac{r^2\Phi^2 - r^2\Phi^2 \cos(\phi)^2 + r^2\Pi^2 - r^2\Pi^2 \cos(\phi)^2 - \psi^2 \cos(\phi)^2 a^2}{r^2}, \quad (\text{B.19})$$

$$T_{r\theta}^{(12)} = \frac{3}{4\pi} \Phi \psi \sin(\phi)^2 \sin(\theta) \cos(\theta), \quad (\text{B.20})$$

$$T_{r\phi}^{(12)} = \frac{3}{4\pi} \Phi \sin(\phi) \sin(\theta)^2 \psi \cos(\phi), \quad (\text{B.21})$$

$$T_{\theta\theta}^{(12)} = -\frac{3}{8\pi} (-\psi^2 \cos(\theta)^2 + \psi^2 \cos(\theta)^2 \cos(\phi)^2 + \psi^2 \cos(\phi)^2) - \frac{3}{8\pi} \frac{r^2 \Pi^2 \cos(\phi)^2 \sin(\theta)^2 - \Pi^2 \sin(\theta)^2 - \Phi^2 \cos(\phi)^2 \sin(\theta)^2 + \sin(\theta)^2 \Phi^2}{a^2}, \quad (\text{B.22})$$

$$T_{\theta\phi}^{(12)} = \frac{3}{4\pi} \psi^2 \sin(\phi) \cos(\theta) \cos(\phi) \sin(\theta), \quad (\text{B.23})$$

$$T_{\phi\phi}^{(12)} = -\frac{3}{8\pi} \frac{(-r^2\Pi^2 + r^2\Pi^2 \cos(\phi)^2 + r^2\Phi^2 - r^2\Phi^2 \cos(\phi)^2 - \psi^2 a^2 + \psi^2 \cos(\phi)^2 a^2) \cos(\theta)^4}{a^2} - \frac{3}{8\pi} \frac{(2r^2\Pi^2 - 2r^2\Pi^2 \cos(\phi)^2 - 2r^2\Phi^2 + 2r^2\Phi^2 \cos(\phi)^2 + \psi^2 a^2) \cos(\theta)^2}{a^2} - \frac{3}{8\pi} \frac{-\psi^2 \cos(\phi)^2 (a)^2 - r^2\Pi^2 + r^2\Pi^2 \cos(\phi)^2 + r^2\Phi^2 - r^2\Phi^2 \cos(\phi)^2}{a^2}. \quad (\text{B.24})$$

$$T_{tt}^{(13)} = -\frac{3}{8\pi} \frac{\alpha^2 (-r^2 \Pi^2 \cos(\phi)^2 - \psi^2 a^2 - r^2 \Phi^2 \cos(\phi)^2 + \psi^2 \cos(\phi)^2 a^2)}{a^2 r^2} \sin(\theta)^2 + \frac{3}{8\pi} \frac{\alpha^2 \psi^2 \cos(\theta)^2}{r^2}, \quad (\text{B.25})$$

$$T_{tr}^{(13)} = \frac{3}{4\pi} \frac{\alpha \Pi \Phi \cos(\phi)^2 \sin(\theta)^2}{a}, \quad (\text{B.26})$$

$$T_{t\theta}^{(13)} = \frac{3}{4\pi} \frac{\alpha \Pi \cos(\phi)^2 \sin(\theta) \psi \cos(\theta)}{a}, \quad (\text{B.27})$$

$$T_{t\phi}^{(13)} = -\frac{3}{4\pi} \frac{\alpha \Pi \sin(\phi) \psi \cos(\phi)}{a} \sin(\theta)^2, \quad (\text{B.28})$$

$$T_{rr}^{(13)} = -\frac{3}{8\pi} \frac{-r^2 \Phi^2 \cos(\phi)^2 + \psi^2 a^2 - r^2 \Pi^2 \cos(\phi)^2 - \psi^2 \cos(\phi)^2 a^2}{r^2} \sin(\theta)^2 - \frac{3}{8\pi} \frac{\psi^2 a^2 \cos(\theta)^2}{r^2}, \quad (\text{B.29})$$

$$T_{r\theta}^{(13)} = \frac{3}{4\pi} \Phi \cos(\phi)^2 \sin(\theta) \psi \cos(\theta), \quad (\text{B.30})$$

$$T_{r\phi}^{(13)} = \frac{3}{4\pi} \Phi \sin(\phi) \psi \cos(\phi) \cos(\theta) - \frac{3}{4\pi} \Phi \sin(\phi) \psi \cos(\phi), \quad (\text{B.31})$$

$$T_{\theta\theta}^{(13)} = \frac{3}{8\pi} \frac{r^2 \Pi^2 \cos(\phi)^2 + \psi^2 \cos(\phi)^2 a^2 - r^2 \Phi^2 \cos(\phi)^2 - \psi^2 a^2}{a^2} \sin(\theta)^2 + \frac{3}{8\pi} \psi^2 \cos(\theta)^2 (2 \cos(\phi)^2 - 1), \quad (\text{B.32})$$

$$T_{\phi\phi}^{(13)} = -\frac{3}{4\pi} \psi^2 \sin(\phi) \cos(\theta) \cos(\phi) \sin(\theta). \quad (\text{B.33})$$

Appendix C

Hydrodynamic equations in the 2+1+1 formalism

In this Appendix we rederive the hydrodynamic equations in the 2+1+1 formalism as originally performed by Maeda *et al* [63]. In particular the following derivation includes some steps not detailed in [63].

We begin by writing the stress-energy tensor in the following way:

$$T^{\mu\nu} = \frac{1}{s^4} \tau \xi^\mu \xi^\nu + \frac{1}{s^2} \tau^i \xi^\mu \gamma^\nu{}_i + \frac{1}{s^2} \tau^i \xi^\nu \gamma^\mu{}_i + \tau^{ij} \gamma^\mu{}_i \gamma^\nu{}_j, \quad (\text{C.1})$$

where we have used the following projections:

$$\tau = T_{\mu\nu} \xi^\mu \xi^\nu, \quad (\text{C.2})$$

$$\tau^i = \gamma^{i\mu} \xi^\nu T_{\mu\nu}, \quad (\text{C.3})$$

$$\tau_{ij} = \gamma_i^\mu g_j^\nu T_{\mu\nu}. \quad (\text{C.4})$$

(We note that we adopt a different notation here for the various projections of the stress energy tensor than that used in Chap. 5. We make a connection between the two notations at the end of the appendix.) By construction, the projection operator satisfies

$$\xi^\mu \gamma^\nu{}_\mu = 0. \quad (\text{C.5})$$

The fluid equations are derived from equations (1.36) and (1.37). We begin with (1.36):

$$T^\mu{}_{\nu;\mu} = 0, \quad (\text{C.6})$$

which can be decomposed in the following way:

$$\xi^\nu (T^\mu{}_\nu)_{;\mu} = 0, \quad (\text{C.7})$$

$$\gamma_{i\nu} (T^{\mu\nu})_{;\mu} = 0. \quad (\text{C.8})$$

We then focus on equation (C.7),

$$\xi^\nu (T^\mu{}_\nu)_{;\mu} = (\xi^\nu T^\mu{}_\nu)_{;\mu} - T^\mu{}_\nu (\xi^\nu)_{;\mu} = 0, \quad (\text{C.9})$$

where the second term on the right hand side is zero since ξ^ν satisfies the Killing equations ($\xi_{\mu;\nu} + \xi_{\nu;\mu} = 0$), and $T^\mu{}_\nu$ is symmetric. Substituting (C.1) in (C.9) and performing some manipulations, we obtain the following expression:

$$\left(\frac{1}{s^2}\tau\xi^\mu\right)_{;\mu} + (\tau^i\gamma^\mu{}_i)_{;\mu} = \left(\frac{\tau}{s^2}\right)_{;\mu}\xi^\mu + \frac{\tau}{s^2}(\xi^\mu)_{;\mu} + (\tau^i)_{|i} + \tau^i(\gamma^\mu{}_i)_{;\mu} = 0. \quad (\text{C.10})$$

Here a vertical bar $()_{|i}$ denotes the covariant derivative D_i in the 3 dimensional quotient spacetime, which is defined by projection of the spacetime covariant derivative, ∇_μ , via $D_i = \gamma^\mu{}_i\nabla_\mu$. The first term of (C.10), which is $\mathcal{L}_\xi(\tau/s^2)$, vanishes since ξ is Killing. The second term is zero because it is proportional to the trace of the Killing equations. Thus we have

$$(\tau^i)_{|i} + \tau^i\left(g^\mu{}_i - \frac{1}{s^2}\xi^\mu\xi_i\right)_{;\mu} = (\tau^i)_{|i} - \frac{\tau^i}{s^2}\xi^\mu(\xi_i)_{;\mu} = 0. \quad (\text{C.11})$$

Using the Killing equation once more, we can express the second term as the derivative of s^2 :

$$(\tau^i)_{|i} + \frac{\tau^i}{2s^2}(s^2)_{|i} = \frac{1}{s}(s\tau^i)_{|i} = 0. \quad (\text{C.12})$$

We now turn attention to equation (C.8):

$$\gamma_{i\nu}(T^{\mu\nu})_{;\mu} = (\gamma_{i\nu}T^{\mu\nu})_{;\mu} - T^{\mu\nu}(\gamma_{i\nu})_{;\mu} = 0. \quad (\text{C.13})$$

Using (C.1) and the definition of the projection operator (5.2), we get the following expression:

$$\left(\frac{1}{s^2}\tau^j\gamma^\nu{}_j\gamma_{i\nu}\xi^\mu\right)_{;\mu} + (\gamma_{i\nu}\gamma^\mu{}_j\gamma^\nu{}_k\tau^{jk})_{;\mu} + T^{\mu\nu}\xi_\nu\left(\frac{\xi_i}{s^2}\right)_{;\mu} = 0. \quad (\text{C.14})$$

Further manipulation gives

$$\frac{1}{s^2}(\tau_i)_{;\mu}\xi^\mu + (\tau^j{}_i)_{|j} + \tau^j{}_i(\gamma^\mu{}_j)_{;\mu} + T^{\mu\nu}\xi_\nu\left(\frac{\xi_i}{s^2}\right)_{;\mu} = 0, \quad (\text{C.15})$$

and combining the second and third terms of the right hand side we find

$$\frac{1}{s^2}(\tau_i)_{;\mu}\xi^\mu + \frac{1}{s}(s\tau^j{}_i)_{|j} + T^{\mu\nu}\xi_\nu\left(\frac{\xi_i}{s^2}\right)_{;\mu} = 0. \quad (\text{C.16})$$

We now consider the first term of this last equation, which, using the definition of τ_i , can be written as

$$\frac{1}{s^2}(\tau_i)_{;\mu}\xi^\mu = \frac{1}{s^2}(\gamma^\lambda{}_i\xi^\sigma T_{\lambda\sigma})_{;\mu}\xi^\mu. \quad (\text{C.17})$$

Expanding the derivative of the product we have

$$\frac{1}{s^2}\left[(\gamma^\lambda{}_i)_{;\mu}\xi^\sigma T_{\lambda\sigma}\xi^\mu + \gamma^\lambda{}_i\xi^\sigma{}_{;\mu}T_{\lambda\sigma}\xi^\mu + \gamma^\lambda{}_i(T_{\lambda\sigma})_{;\mu}\xi^\mu\xi^\sigma\right]. \quad (\text{C.18})$$

We now use the fact that the Lie derivative along the Killing vector field of the stress energy tensor vanishes, i.e.

$$\mathcal{L}_\xi T_{\mu\nu} = \xi^\lambda(T_{\mu\nu})_{;\lambda} + T_{\lambda\mu}(\xi^\lambda)_{;\nu} + T_{\nu\lambda}(\xi^\lambda)_{;\mu} = 0, \quad (\text{C.19})$$

to further manipulate (C.76):

$$\frac{1}{s^2} \left[(\gamma^\lambda)_i{}_{;\mu} \xi^\sigma T_{\lambda\sigma} \xi^\mu + \gamma^\lambda_i (\xi^\sigma)_{;\mu} T_{\lambda\sigma} \xi^\mu - \gamma^\lambda_i \xi^\sigma T_{\mu\lambda} (\xi^\mu)_{;\sigma} - \gamma^\lambda_i \xi^\sigma T_{\mu\sigma} (\xi^\mu)_{;\lambda} \right]. \quad (\text{C.20})$$

The second and the third terms in the above sum to 0 (as can be seen by relabelling dummy indexes), and therefore (C.17) can be written as

$$\frac{1}{s^2} (\tau_i)_{;\mu} \xi^\mu = \frac{1}{s^2} \left[(\gamma^\lambda)_i{}_{;\mu} \xi^\sigma T_{\lambda\sigma} \xi^\mu - \gamma^\lambda_i \xi^\sigma T_{\mu\sigma} (\xi^\mu)_{;\lambda} \right] = \frac{1}{s^2} \left\{ \xi^\sigma T_{\mu\sigma} \left[(\gamma^\mu)_i{}_{;\lambda} \xi^\lambda - \gamma^\lambda_i (\xi^\mu)_{;\lambda} \right] \right\}. \quad (\text{C.21})$$

We can now introduce this last result into equation (C.16):

$$\frac{1}{s} (s\tau^j_i)_{|j} + T^{\mu\nu} \xi_\nu \left[\frac{1}{s^2} (\gamma_{\mu i})_{;\lambda} \xi^\lambda - \frac{1}{s^2} \gamma^\lambda_i (\xi_\mu)_{;\lambda} + \left(\frac{\xi_i}{s^2} \right)_{;\mu} \right] = 0. \quad (\text{C.22})$$

The expression in brackets can be further simplified using the definition of the projection operator (5.2)

$$\frac{1}{s} (s\tau^j_i)_{|j} + T^{\mu\nu} \xi_\nu \left[-\frac{1}{s^4} (\xi_\mu \xi_i)_{;\lambda} \xi^\lambda - \frac{1}{s^2} \gamma^\lambda_i (\xi_\mu)_{;\lambda} + \frac{1}{s^4} \xi^\lambda \xi_i (\xi_\mu)_{;\lambda} + \left(\frac{\xi_i}{s^2} \right)_{;\lambda} \right] = 0. \quad (\text{C.23})$$

Some algebra gives

$$\frac{1}{s} (s\tau^j_i)_{|j} + T^{\mu\nu} \xi_\nu \left[-\frac{1}{s^4} \xi_\mu (\xi_i)_{;\lambda} \xi^\lambda - \frac{1}{s^2} (\xi_\mu)_{;i} + \left(\frac{\xi_i}{s^2} \right)_{;\mu} \right] = 0, \quad (\text{C.24})$$

and then using the Killing equations repeatedly, we find

$$\frac{1}{s} (s\tau^j_i)_{|j} + T^{\mu\nu} \xi_\nu \left[-\left(\frac{\xi_\mu}{s^2} \right)_{;i} - \frac{1}{s^3} \xi_\mu (s)_{;i} + \left(\frac{\xi_i}{s^2} \right)_{;\mu} \right] = 0. \quad (\text{C.25})$$

Using the definition of τ (C.2) we have

$$\frac{1}{s} (s\tau^j_i)_{|j} + T^{\mu\nu} \xi_\nu \left[-\left(\frac{\xi_\mu}{s^2} \right)_{;i} + \left(\frac{\xi_i}{s^2} \right)_{;\mu} \right] - \tau \frac{\partial_i s}{s^3} = 0. \quad (\text{C.26})$$

We now use expression A12 from [34]:

$$\nabla_\mu \xi_\nu = \frac{1}{2s^2} \epsilon_{\mu\nu\alpha\beta} \xi^\alpha \omega^\beta + \frac{1}{2s^2} \xi_{[\nu} \nabla_{\mu]} s^2, \quad (\text{C.27})$$

to simplify the second term of the equation (C.26):

$$T^{\mu\nu} \xi_\nu \left[-\left(\frac{\xi_\mu}{s^2} \right)_{;i} + \left(\frac{\xi_i}{s^2} \right)_{;\mu} \right] = -\frac{1}{s^4} \tau^b \gamma^\nu_j \epsilon_{i\nu\gamma\sigma} \xi^\gamma \omega^\sigma = \frac{1}{s^3} \tau^j \epsilon_{ijk} \omega^k. \quad (\text{C.28})$$

With this result equation (C.26) becomes

$$\frac{1}{s} (s\tau^j_i)_{|j} - \tau \frac{s|i}{s^3} + \frac{1}{s^3} \tau^j \epsilon_{ijk} \omega^k = 0. \quad (\text{C.29})$$

This concludes the initial decomposition of equations (C.6) in directions parallel and orthogonal to ξ^μ , and using quantities adapted to the projection with respect to the Killing field.

We now proceed to a space-plus-time (2+1) split of equations (C.12) and (C.29). To that end we introduce another projection operator, H^i_j ,

$$H^i_j = \gamma^i_j + n^i n_j, \quad (\text{C.30})$$

where n^i is the unit-norm, future-directed, orthogonal vector field to the constant time surfaces (which, in an abuse of terminology we will refer to as hypersurfaces). The following relations will be useful in the subsequent derivations:

$$n^i n_i = -1, \quad (\text{C.31})$$

$$a_j = n^k (n_j)_{|k} = \partial_j (\alpha) / \alpha, \quad (\text{C.32})$$

$$n_i = (-\alpha, 0, 0), \quad (\text{C.33})$$

$$n^i = \left(\frac{1}{\alpha}, -\frac{\beta^I}{\alpha} \right), \quad (\text{C.34})$$

$$(n^i)_{|i} = \frac{1}{\alpha\sqrt{H}} \mathcal{L}_t (\sqrt{H}) - \frac{1}{\alpha} (\beta^I)_{||I}. \quad (\text{C.35})$$

Note that α is the lapse function, while β^I is the shift vector. In addition, the double vertical bar $()_{||I}$ denotes covariant differentiation in the 2-dimensional spacelike surfaces of our dimensionally reduced spacetime (i.e. differentiation compatible with the 2-metric H_{IJ}).

We proceed to a decomposition of (C.12) by first splitting τ^i into hypersurface-orthogonal and hypersurface-tangential pieces:

$$\tau^i = J_\phi n^i + S^I H^i_I, \quad (\text{C.36})$$

$$J_\phi = -n_i \tau^i, \quad (\text{C.37})$$

$$S^I = H^I_j \tau^j. \quad (\text{C.38})$$

Inserting this decomposition into equation (C.12) we obtain

$$\frac{1}{s} (sJ_\phi n^i)_{|i} + \frac{1}{s} (sS^I H^i_I)_{|i} = 0, \quad (\text{C.39})$$

and expanding the derivatives of the products, we find

$$\frac{1}{s} (sJ_\phi)_{|i} n^i + J_\phi (n^i)_{|i} + \frac{1}{s} (sS^I)_{||I} + S^I (H^i_I)_{|i} = 0. \quad (\text{C.40})$$

It is now convenient to define a new vector field, $N^i = \alpha n^i$. Making use of this definition as well as (C.35) we can write (C.40) as

$$\frac{1}{\alpha s} (sJ_\phi)_{|i} N^i + J_\phi \left[\frac{1}{\alpha\sqrt{H}} \mathcal{L}_t (\sqrt{H}) - \frac{1}{\alpha} (\beta^I)_{||I} \right] + \frac{1}{s} (sS^I)_{||I} + S^I (n^i n_I)_{|i} = 0. \quad (\text{C.41})$$

Now, using the fact that $t^i = N^i + \beta^i$ and $n_I = (0, 0)$ and regrouping terms, we get the first of our final equations:

$$\frac{1}{\alpha s \sqrt{H}} \mathcal{L}_t \left(s \sqrt{H} J_\phi \right) + \frac{1}{\alpha s} \left[\alpha s \left(S^I - J_\phi \frac{\beta^I}{\alpha} \right) \right]_{\parallel I} = 0. \quad (\text{C.42})$$

We now similarly decompose (C.29):

$$\frac{1}{s} \left(s \tau_i^j \right)_{|j} - \tau \frac{s|i}{s^3} + \frac{1}{s^3} \tau^j \epsilon_{ijk} \omega^k = 0. \quad (\text{C.43})$$

The hypersurface-orthogonal and hypersurface tangential components of the above are

$$n^i \frac{1}{s} \left(s \tau_i^j \right)_{|j} - \tau n^i \frac{s|i}{s^3} + n^i \frac{1}{s^3} \tau^j \epsilon_{ijk} \omega^k = 0, \quad (\text{C.44})$$

$$h^i_I \frac{1}{s} \left(s \tau_i^j \right)_{|j} - \tau h^i_I \frac{s|i}{s^3} + h^i_I \frac{1}{s^3} \tau^j \epsilon_{ijk} \omega^k = 0. \quad (\text{C.45})$$

We begin by manipulating the first term of equation (C.44),

$$\frac{n^i}{s} \left(s \tau_i^j \right)_{|j} = \frac{1}{s} \left(s n^i \tau_i^j \right)_{|j} - \tau^j_i \left(n^i \right)_{|j}. \quad (\text{C.46})$$

Using the decomposition

$$\tau^j_i = n_i n^j \rho_H + n_i H^j J J^J + n^j H_{iI} J^I + H^{jJ} H_i^I S_{IJ}, \quad (\text{C.47})$$

where we have made use of the following definitions

$$\rho_H = n_i n_j \tau^{ij}, \quad (\text{C.48})$$

$$J^J = -n_i H^J J \tau^{ij}, \quad (\text{C.49})$$

$$S_{IJ} = H_{iI} H_{jJ} \tau^{ij}, \quad (\text{C.50})$$

we obtain

$$\frac{1}{s} \left[s \left(-n^j \rho_H - H^j J J^J \right) \right]_{|j} - \tau^j_i \left(n^i \right)_{|j}. \quad (\text{C.51})$$

After some algebra and the use of (C.35) we obtain

$$-\frac{1}{\alpha s \sqrt{H}} \mathcal{L}_t \left(s \sqrt{H} \rho_H \right) - \frac{1}{\alpha s} \left[\alpha s \left(J^I - \rho_H \frac{\beta^I}{\alpha} \right) \right]_{\parallel I} - \tau^j_i \left(n^i \right)_{|j}. \quad (\text{C.52})$$

Using the following property

$$\left(n_i \right)_{|j} = -K_{ij} - n_j \left(a \right)_{|i}, \quad (\text{C.53})$$

and the fact that $n^i K_{ij} = 0$ and $n^j a_{|j} = 0$ we find that the first term of equation (C.52) can be written

$$-\frac{1}{\alpha s \sqrt{H}} \mathcal{L}_t \left(s \sqrt{H} \rho_H \right) - \frac{1}{\alpha s} \left[\alpha s \left(J^I - \rho_H \frac{\beta^I}{\alpha} \right) \right]_{\parallel I} + (P + \rho_H) \left[v^I v^J K_{IJ} - v^I \frac{\alpha_{\parallel I}}{\alpha} \right] + P K^I_I. \quad (\text{C.54})$$

Here, we have made use of the fact that the stress energy tensor under consideration is that for a perfect fluid. Therefore we have:

$$S_{IJ} = (P + \rho_{\text{H}}) v^I v^J + H^{IJ} P, \quad (\text{C.55})$$

$$J^I = (P + \rho_{\text{H}}) v^I. \quad (\text{C.56})$$

We now shift attention to the remaining terms of (C.44). The second term can be written as

$$-\tau \frac{s_{|i} n^i}{s^3} = \frac{\tau}{s^3} \kappa, \quad (\text{C.57})$$

where we have defined κ via $\kappa = -s_{|i} n^i$. In order to simplify the third term of (C.44), namely

$$\frac{1}{s^3} \tau^j \epsilon_{ijk} \omega^k n^i, \quad (\text{C.58})$$

we use the following definitions:

$$w^i = -n^i \Omega_{\text{H}} + H^{iJ} \Omega_J, \quad (\text{C.59})$$

$$\Omega_{\text{H}} = n_i \omega^i, \quad (\text{C.60})$$

$$\Omega_I = H^J{}_I \omega^J. \quad (\text{C.61})$$

Introducing these into (C.58) we obtain

$$\frac{1}{s^3} (J_\phi n^j + S^I H^j{}_I) \epsilon_{ijk} (-n^k \Omega_{\text{H}} + h^{kJ}) n^i. \quad (\text{C.62})$$

Now, by the antisymmetry of ϵ_{ijk} , the only term that survives in the above is

$$\frac{1}{s^3} S^I H^j{}_I H^{kJ} \Omega_J \epsilon_{ijk} n^i. \quad (\text{C.63})$$

which has only a single factor of n^i . We thus have

$$\frac{1}{s^3} \tau^j \epsilon_{ijk} \omega^k n^i = \frac{1}{s^3} S_I \Omega_J \epsilon^{IJ} = \frac{2}{s^2} E^I S_I = J_\phi \frac{2}{s^2} E_I v^I, \quad (\text{C.64})$$

where we have made the following definitions:

$$\epsilon_{ij} = n^k \epsilon_{kij}, \quad (\text{C.65})$$

$$E^I = \frac{1}{2s} \epsilon^{IJ} \Omega_J. \quad (\text{C.66})$$

Collecting all of the terms, equations (C.54), (C.57), (C.64), together we find

$$\begin{aligned} & -\frac{1}{\alpha s \sqrt{H}} \mathcal{L}_t (s \sqrt{H} \rho_{\text{H}}) - \frac{1}{\alpha s} \left[\alpha s \left(J^I - \rho_{\text{H}} \frac{\beta^I}{\alpha} \right) \right]_{||I} \\ & + (P + \rho_{\text{H}}) \left[v^I v^J K_{IJ} - v^I \frac{\alpha_{||I}}{\alpha} \right] + P K^I{}_I + \tau \frac{\kappa}{s^3} + J_\phi \frac{2}{s^2} E_I v^I = 0 \end{aligned} \quad (\text{C.67})$$

where $J^I = (\rho_H + P)v^I$, $\tau = J_\phi v^\phi s^2 + Ps^2$, $E_\phi = \kappa s$.

Thus our final equation is:

$$\begin{aligned} & \frac{1}{\alpha s \sqrt{H}} \mathcal{L}_t \left(s \sqrt{H} \rho_H \right) + \frac{1}{\alpha s} \left[\alpha s \left(J^I - \rho_H \frac{\beta^I}{\alpha} \right) \right]_{||I} \\ & - (P + \rho_H) \left[v^I v^J K_{IJ} - v^I \frac{\alpha_{||I}}{\alpha} \right] \\ & - P \left(K^I{}_I - \frac{1}{s} \kappa \right) + \frac{1}{s^2} J_\phi \left(\frac{1}{s^2} E_\phi v_\phi + 2E_I v^I \right) = 0. \end{aligned} \quad (C.68)$$

We now turn to (C.45). Manipulation of its first term yields

$$h^i{}_I \frac{1}{s} (s \tau^j{}_i)_{|j} = \frac{1}{s} (s H^i{}_I \tau^j{}_i)_{|j} - \tau^j{}_i (H^i{}_I)_{|j}. \quad (C.69)$$

Using the decomposition

$$\tau^j{}_i = n_i n^j \rho_H + n_i H^j{}_J J^J + n^j H_{iI} J^I + H^{jJ} H_i{}^K S_{JK}, \quad (C.70)$$

yields

$$\frac{1}{s} [s H^i{}_I n^j H_{iK} J^K + H^{jJ} H^i{}_I S_{JK} H^K{}_i]_{|j} - \tau^j{}_i (H^i{}_I)_{|j}. \quad (C.71)$$

Now, using the definition of the projection operator H_{ij} , property (C.35), and the fact that $t^i = N^i + \beta^i$, we find, after some algebra, that

$$\begin{aligned} & \frac{J_I}{\alpha \sqrt{H}} \mathcal{L}_t \left(\sqrt{h} \right) - \frac{J_I}{\alpha} (\beta^J)_{||J} + \frac{1}{\alpha s} \mathcal{L}_t (s J_I) - \frac{1}{\alpha s} (s J_U)_{||J} \beta^J - \\ & \frac{J_J}{\alpha} (\beta^J)_{||I} + \frac{1}{\alpha s} (\alpha s S^J{}_I)_{||J} + \rho_H n^j (n_I)_{|j} + J^J (n_I)_{||J} \end{aligned} \quad (C.72)$$

Regrouping terms we have

$$\begin{aligned} & \frac{1}{\alpha s \sqrt{H}} \mathcal{L}_t \left(s \sqrt{H} J_I \right) + \frac{1}{\alpha s} \left[\alpha s \left(S^J{}_I - \frac{\beta^J}{\alpha} J_I \right) \right]_{||J} - \\ & \frac{J_J}{\alpha} (\beta^J)_{||I} + \rho_H n^j (n_I)_{|j} + J^J (n_I)_{||J}. \end{aligned} \quad (C.73)$$

Now using identity (4.7.6) from [110]:

$$(Y^J{}_I)_{||J} = \frac{1}{\sqrt{H}} \left(\sqrt{H} Y^J{}_I \right)_{,J} - Y^{JK} (H_{KI})_{,J} + H_{KI} \Gamma^K{}_{JL} Y^{JL}. \quad (C.74)$$

expression (C.73) becomes

$$\begin{aligned} & \frac{1}{\alpha s \sqrt{H}} \mathcal{L}_t \left(s \sqrt{H} J_I \right) + \frac{1}{\alpha s \sqrt{H}} \left[\alpha s \sqrt{H} \left(S^J{}_I - \frac{\beta^J}{\alpha} J_I \right) \right]_{,J} - \\ & \left(S^{JK} - \frac{\beta^J}{\alpha} J^K \right) \left[(H_{KI})_{,J} - {}^{(2)}\Gamma_{IJK} \right] - \\ & \frac{J_J}{\alpha} (\beta^J)_{||I} + \rho_H n^j (n_I)_{|j} + J^J (n_I)_{||J}. \end{aligned} \quad (C.75)$$

Expanding the Christoffel symbols, we have

$$\begin{aligned}
 & \frac{1}{\alpha s \sqrt{H}} \mathcal{L}_t (s \sqrt{H} J_I) + \frac{1}{\alpha s \sqrt{H}} \left[\alpha s \sqrt{H} \left(S^J{}_I - \frac{\beta^J}{\alpha} J_I \right) \right]_{,J} - \\
 & \left(S^{JK} - \frac{\beta^J}{\alpha} J^K \right) \left[\frac{1}{2} (H_{IK})_{,J} - \frac{1}{2} (H_{IJ})_{,K} + \frac{1}{2} (H_{JK})_{,I} \right] - \\
 & \frac{J_J}{\alpha} \left\{ (\beta^J)_{,I} + \frac{1}{2} H^{JL} \beta^K \left[(H_{LK})_{,I} + (H_{LI})_{,K} - (H_{IJ})_{,L} \right] \right\} + \\
 & \rho_H n^j (n_I)_{|j} + J^J (n_I)_{||J}.
 \end{aligned} \tag{C.76}$$

Regrouping terms, we have rewritten the first term of equation (C.45) as

$$\begin{aligned}
 & \frac{1}{\alpha s \sqrt{H}} \mathcal{L}_t (s \sqrt{H} J_I) + \frac{1}{\alpha s \sqrt{H}} \left[\alpha s \sqrt{H} \left(S^J{}_I - \frac{\beta^J}{\alpha} J_I \right) \right]_{,J} - S^{JK} \frac{1}{2} (H_{JK})_{,I} + \\
 & \rho_H \frac{\alpha_{||I}}{\alpha} + J^J (n_I)_{||J} - J_J \frac{\beta^J{}_I}{\alpha}.
 \end{aligned} \tag{C.77}$$

We now proceed to the last term of (C.45):

$$\frac{1}{s^3} \tau^b \epsilon_{ijk} \omega^k H^i{}_I. \tag{C.78}$$

Using the decomposition

$$\tau^j = n^j J_\phi + H^j{}_K S^K, \tag{C.79}$$

and

$$w^k = -\Omega_H n^k + \Omega_J H^{Jk}, \tag{C.80}$$

we get

$$-\frac{1}{s^3} J_\phi \epsilon_{IJ} \Omega^J - \frac{1}{s^3} \epsilon_{IK} \Omega_H S^K. \tag{C.81}$$

Here we have used the fact that $H^j{}_K H^i{}_I H^{kJ} \epsilon_{ijk} = 0$ as well as the definition of ϵ_{IJ} . Now, using $B_\phi = 1/2\Omega_H$ and $E_I = 1/(2s)\epsilon_{IJ}\Omega^J$ we obtain

$$-2\frac{1}{s^2} J_\phi E_I - \frac{2}{s^3} B_\phi S^K \epsilon_{IK}. \tag{C.82}$$

Again using the fact that we have restricted attention to the case where the stress energy is that of a perfect fluid, we can use $S^I = J_\phi v^I$ which gives

$$-\frac{1}{s^2} J_\phi \left(2E_I + \frac{2}{s} B_\phi v^K \epsilon_{IK} \right). \tag{C.83}$$

Collecting all the terms together, i.e. collecting expressions (C.76) and (C.83),

$$\begin{aligned}
 & \frac{1}{\alpha s \sqrt{H}} \mathcal{L}_t (s \sqrt{H} J_I) + \frac{1}{\alpha s \sqrt{H}} \left[\alpha s \sqrt{H} \left(S^J{}_I - \frac{\beta^J}{\alpha} J_I \right) \right]_{,J} - S^{JK} \frac{1}{2} (H_{JK})_{,I} + \\
 & \rho_H \frac{\alpha_{||I}}{\alpha} + J^J (n_I)_{||J} - J_J \frac{\beta^J{}_I}{\alpha} - \frac{1}{s^2} J_\phi \left(2E_I + \frac{2}{s} B_\phi v^K \epsilon_{IK} \right) - \tau \frac{s_{||I}}{s^3},
 \end{aligned} \tag{C.84}$$

and using the fact that $\tau = J_\phi v_\phi + Ps^2$ we have

$$\begin{aligned} & \frac{1}{\alpha s \sqrt{H}} \mathcal{L}_t \left(s \sqrt{H} J_I \right) + \frac{1}{\alpha s \sqrt{H}} \left[\alpha s \sqrt{H} \left(S^J{}_I - \frac{\beta^J}{\alpha} J_I \right) \right]_{,J} - S^{JK} \frac{1}{2} (H_{JK})_{,I} - J_J \frac{\beta^J{}_{,I}}{\alpha} \\ & + \rho_H \frac{\alpha_{||I}}{\alpha} + J^J (n_I)_{||J} - \frac{1}{s^2} J_\phi \left(2E_I + \frac{2}{s} B_\phi v^K \epsilon_{IK} \right) - J_\phi v_\phi \frac{s_{||I}}{s^3} - P \frac{s_{||I}}{s} \end{aligned} \quad (C.85)$$

Now, since $\epsilon_{IK} \epsilon^{KJ} = -\delta^J{}_I$, $B^K = \epsilon^{IJ} \partial_{BS}$ and $J^J (n_I)_{||J} = 0$, we find our final expression for equation (C.45):

$$\begin{aligned} & \frac{1}{\alpha s \sqrt{H}} \mathcal{L}_t \left(s \sqrt{H} J_I \right) + \frac{1}{\alpha s \sqrt{H}} \left[\alpha s \sqrt{H} \left(S^J{}_I - \frac{\beta^J}{\alpha} J_I \right) \right]_{,J} \\ & - (\rho_H + P) \left[v^J v^K \frac{1}{2} (H_{JK})_{,I} + v_J \frac{\beta^J{}_{,I}}{\alpha} \right] \\ & + \rho_H \frac{\alpha_{||I}}{\alpha} - \frac{1}{s^2} J_\phi \left[2E_I + \epsilon_{IK} \left(\frac{2}{s} B_\phi v^K - \frac{1}{s} B^K v_\phi \right) \right] - P \frac{s_{||I}}{s} = 0. \end{aligned} \quad (C.86)$$

Equations (C.42), (C.68) and (C.86) represent the local conservation of energy, angular momentum and linear momentum, respectively. To make connection with the notation used in chapter 5 we make the identifications

$$\rho_H = \tau + D, \quad (C.87)$$

$$J_I = S_I, \quad (C.88)$$

$$J_\phi = S_\phi, \quad (C.89)$$

$$S_I = S_\phi v_I, \quad (C.90)$$

$$S_{IJ} = S_I v_J + H_{IJ} P, \quad (C.91)$$

where the quantities on the left are the variables defined and used in this appendix, while those on the right are used in Chap. 5.

Finally, we must rewrite the equation of (local) baryon number conservation,

$$J^\mu{}_{;\mu} = (\rho_0 u^\mu)_{;\mu} = 0. \quad (C.92)$$

The above implies

$$\frac{1}{s \alpha \sqrt{H}} \left(s \alpha \sqrt{H} \rho_0 u^\mu \right)_{;\mu} = 0, \quad (C.93)$$

and then using the variables defined in Chap. 5, we have:

$$\frac{1}{s \alpha \sqrt{H}} \mathcal{L}_t \left(s \sqrt{H} D \right) + \frac{1}{s \alpha \sqrt{H}} \left[s \alpha \sqrt{H} D \left(v^I - \frac{\beta^I}{\alpha} \right) \right]_{,I} = 0. \quad (C.94)$$

This completes our derivation of the hydrodynamical equations within the 2+1+1 formalism.

Appendix D

Characteristic Structure

The characteristic structure for the Jacobian or velocity matrix $\tilde{\mathbf{V}}_{ij}^\rho = \partial \tilde{\mathbf{F}}_j^\rho / \partial \tilde{\mathbf{q}}^i$ is given by the following set of eigenvalues:

$$\lambda_0 = \alpha v^\rho - \beta^\rho \quad \text{triply degenerate,} \quad (\text{D.1})$$

$$\lambda_\pm = \frac{\alpha}{1 - v^2 c_s^2} \left\{ v^\rho (1 - c_s^2) \pm c_s \sqrt{(1 - v^2) [H^{\rho\rho} (1 - v^2 c_s^2) - v^\rho v^\rho (1 - c_s^2)]} \right\} - \beta^\rho, \quad (\text{D.2})$$

and the corresponding right eigenvectors:

$$\mathbf{r}_{0,1} = \left(\frac{\mathcal{K}}{hW}, v_\rho, v_z, v_\phi, 1 - \frac{\mathcal{K}}{hW} \right)^T, \quad (\text{D.3})$$

$$\mathbf{r}_{0,2} = (Wv_z, 2hW^2 v_\rho v_z, h(\psi^4 + 2W^2 v_z v_z), 2hW^2 v_z v_\phi, Wv_z(2hW - 1)), \quad (\text{D.4})$$

$$\mathbf{r}_{0,3} = (Wv_\phi, 2hW^2 v_\rho v_\phi, 2hW^2 v_z v_\phi, h(s^2 + 2W^2 v_\phi v_\phi), Wv_\phi(2hW - 1)), \quad (\text{D.5})$$

$$\mathbf{r}_\pm = (1, hW\mathcal{C}_\pm^\rho, hWv_z, hWv_\phi, hW\tilde{\mathcal{A}}_\pm^\rho - 1). \quad (\text{D.6})$$

In the above expressions we have made use of the following definitions

$$\mathcal{K} = \frac{\tilde{\kappa}}{\tilde{\kappa} - c_s^2}, \quad (\text{D.7})$$

$$\tilde{\kappa} = \kappa / \rho_0, \quad (\text{D.8})$$

$$\mathcal{C}_\pm^\rho = v_\rho - \mathcal{V}_\pm^\rho, \quad (\text{D.9})$$

$$\mathcal{V}_\pm^\rho = (v^\rho - \Lambda_\pm^\rho) / (1/\psi^4 - v^\rho \Lambda_\pm^\rho), \quad (\text{D.10})$$

$$\tilde{\mathcal{A}}_\pm^\rho = (1/\psi^4 - v^\rho v^\rho) / (1/\psi^4 - v^\rho \Lambda_\pm^\rho), \quad (\text{D.11})$$

$$\Lambda_\pm^\rho = \lambda_\pm / \alpha + \beta^\rho / \alpha, \quad (\text{D.12})$$

where $c_s^2 = 1/h(\chi + P/\rho_0^2 \kappa)$, $\chi = \partial P / \partial \rho_0$ and $\kappa = \partial P / \partial \epsilon$. The characteristic structure of the Jacobian matrix in the z direction, $\tilde{\mathbf{V}}_{ij}^z = \partial \tilde{\mathbf{F}}_j^z / \partial \tilde{\mathbf{q}}^i$ can be easily calculated from the above results using symmetry arguments, and is explained in [30].